Design and Construction of a Sulfur Dioxide Gas Permeation Device and Further Screening of Metal-Organic Frameworks for the Removal of Harmful Gases from the Air

by ©

Victoria Downing

A Thesis submitted

to the School of Graduate Studies
in partial fulfillment of the
requirements for the degree of
Master of Science

Department of Chemistry

Memorial University of Newfoundland

September 2021

St. John's, Newfoundland and Labrador

Abstract

Metal-organic frameworks (MOFs) are a class of porous materials comprised of metal nodes and organic linkers. These tunable materials possess high accessible surface area, making them attractive for a variety of applications (e.g., gas separations, gas storage, and catalysis). The primary focus in this thesis has been to examine the experimental design and the application of MOFs for the sorption and separation of harmful gases. This thesis will focus on two different topics.

Firstly, the application of MOFs for the sorption of sulfur dioxide (SO_2) gas was explored. SO_2 is a criteria air pollutant, being one of the most common air pollutants monitored by the government. SO_2 gas is harmful to both human health (e.g., respiratory ailments) and the environment (e.g., acid rain). The primary anthropogenic source of SO_2 in the environment is the combustion of fossil fuels. Existing pre- and post- combustion methods for the removal of SO_2 are costly and are unable to meet stringent environmental regulations. These drawbacks in pre-existing methods/materials increase the demand for more effective and lower cost alternatives. The challenge with studying SO_2 adsorption/separation is in the toxicity and corrosive nature of the gas. This makes it difficult to study SO_2 at environmental concentrations. With that in mind, we aimed to create a tunable SO_2 source to test MOFs for their sorption potential of gaseous SO_2. Chapter 2 will thoroughly discuss the experiments that were implemented in creating an SO_2 gas source.

Secondly, MOFs were investigated for their potential to separate carbon monoxide (CO) from other gases on the basis of size exclusion. Our primary interest has been to separate

carbon dioxide (CO_2) from CO. This is due to the risks associated with incomplete combustion that leads to formation of CO. CO is a colorless and odorless gas that, even at low concentrations, can be extremely detrimental to human health. Therefore, newly discovered MOF systems were investigated for their ability to sieve CO from other common gases (CO_2 and N_2) via their unique pore apertures. The synthesis, crystal structure, and separation capabilities of both $Zn_3(NH_2BDC)_3DABCO$ and $Zn_2Cd(NH_2BDC)_3DABCO$ will be discussed in-depth in Chapter 3.

Acknowledgements

First and foremost, I would like to give a huge thanks to my supervisor Dr. Michael Katz. Without his help, this thesis would not be what it is today. He offered continued support and never gave up on me throughout the process. He taught me how to be a great chemist in terms of asking the right questions in the project, taking the right approach to further experiments, and how to analyze data meaningfully. Mike always made sure that we were safe in the lab but were able to have fun and lean on other group members for help. I cannot thank you enough for my fun and educational experience throughout my degree. Mike was the first to introduce me to MOFs, and it has given me a lifelong interest in the topic. One day I hope MOFs are able to help solve our environmental issues.

Secondly, I would like to give a thank you to Devon McGrath. You were extremely helpful with all of the SO_2 gas studies. We were able to work extremely well as a team, and the project would not have been as successful as it was without you in it. I would also like to thank Nathan Butt, a former MUCEP student, that was able to also help my project along.

I would like to thank my two committee members, Dr. Travis Fridgen and Dr. Peter Pickup. In terms of experiments, I would like to thank Dr. Celine Schneider for teaching me all I know about NMR and Dr. Wanda Aylward for running all of my PXRD experiments.

Finally, I would like to thank all of the members of the MOFia group (i.e., the MOFstars). You provided a safe and friendly atmosphere. I could always lean on one of you to help me if need be. Some of the times spent in our student office, I will never forget.

Table of Contents

List of Tables

List of Figures

List of Abbreviations and Symbols

Å	Angstrom
H_2-BDC	1,4-benzenedicarboxylic acid (terephthalic acid)
H_2-BPDC	biphenyl-4,4’-dicarboxylic acid
CH_4	methane
cm	centimeter
CO	carbon monoxide
CO_2	carbon dioxide
DABCO	1,4-diazabicyclo[2.2.2.]octane
DMF	*N,N*-dimethylformamide
DMSO	dimethyl sulfoxide
HCl	hydrochloric acid
IR	infrared
MeOH	methanol
MOFs	metal-organic frameworks
H_2-NH_2BDC	2-aminoterephthalic acid (BDC = 1,4 – benzenedicarboxylic acid)
nm	nanometer

NMR	nuclear magnetic resonance
NO_x	nitrous oxides
PFA	perfluoroalkoxy
PID	proportional integral derivative
PM	particular matter
ppb	parts per billion
ppbv	part per billion per volume
ppm	parts per million
PTFE	polytetrafluoroethylene
PXRD	powder X-ray diffraction
sccm	standard cubic centimeters per minute
SO_x	sulfur oxides
TGA	thermogravimetric analysis

Chapter 1

Introduction

1.1 Porous Materials

Porous materials are defined as materials whose observed surface area exceeds the surface area determined by examining the external dimensions alone. This increase in surface area is due to the presence of empty space inside the material that can be accessed by molecules smaller than the pore aperture and pore volume. These empty spaces within the structure of the material, referred to as pores, are typically filled with fluids (e.g., liquid or gas).[1, 2] The unique structure of these porous materials offers a variety of innovative applications within the fields of science and engineering. These applications include gas storage and separation,[3-9] catalysis,[10-15] and sensing.[16-20] Some common examples of porous materials are different types of carbon, zeolites, and metal-organic frameworks (MOFs). Within our research group,[21-24] and thus in this thesis, the work focuses on the design and applications of MOFs.

1.1.1 Metal-organic Frameworks

MOFs are a class of highly porous materials that are made up of a combination of inorganic metal nodes attached via organic linkers (Figure 1.1).[25, 26] The inorganic metal nodes exist as metal ions, dimers, chains, or metal clusters.[27] Typical metals found in MOFs include zinc, zirconium, and copper (Figure 1.1). The organic linkers feature two or more Lewisbasic groups that promote the bridging of metal nodes rather than chelation.[28] Typical linkers include Lewis-bases such as carboxylates, phosphonates, amines, and N-heterocyclic groups like pyridine and imidazole, to name a few.[29] Due to the wide variety of options available for nodes and linkers, there are thousands of MOFs available to be synthesized.[30]

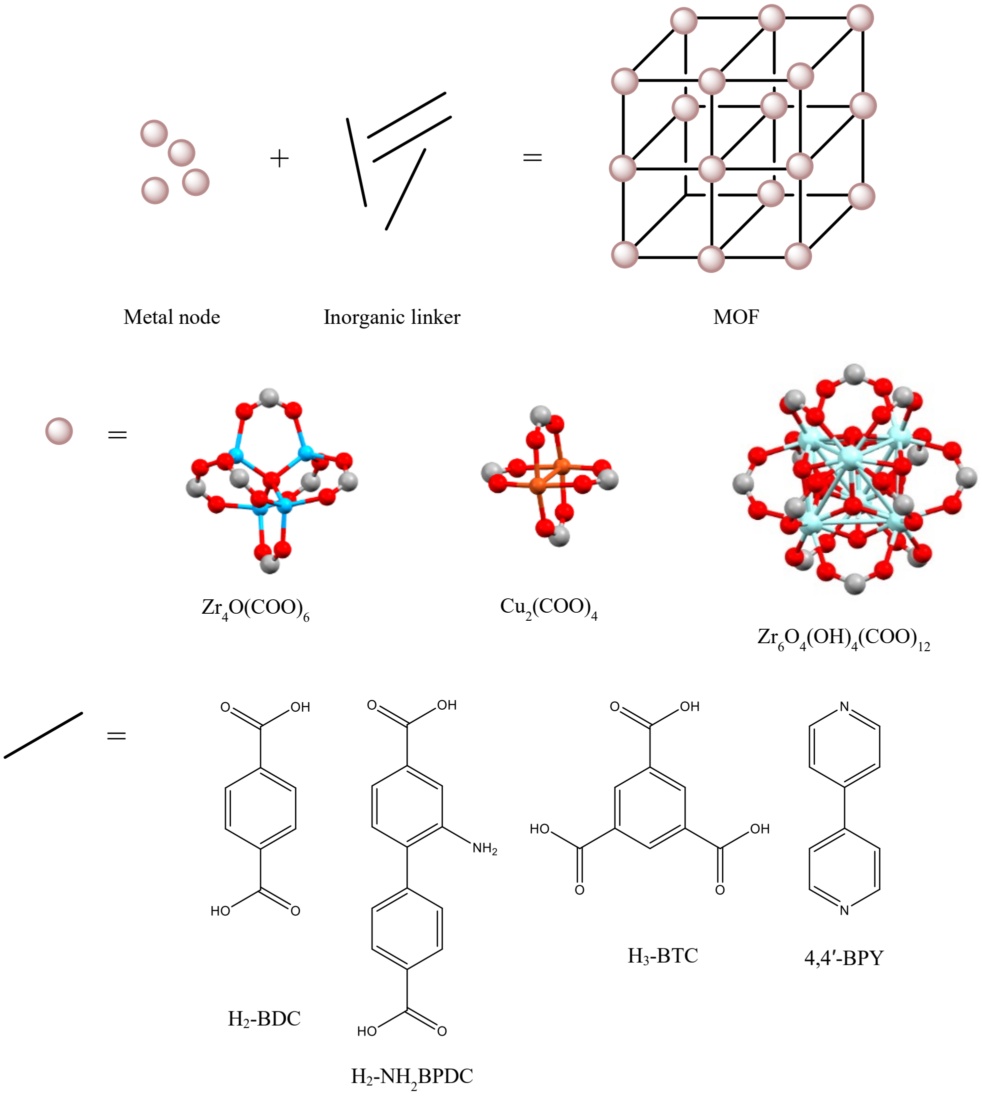

Figure 1.1. Examples of metal nodes (pink circles) and organic linkers (black rods) in MOFs [Cu, orange; Zn, light blue; Zr, dark blue; C, grey; O, red].[31-33]

1.1.2 Applications of Metal-organic Frameworks

With the customizable nature of MOFs, coupled with their applications, there has been an increased drive to synthesize such materials while concomitantly targeting them towards various applications.

For many MOF applications, an adsorbate (molecule being introduced) is adsorbed on the adsorbent (internal and external surface of the MOF). There are two main adsorption routes possible. If weaker intermolecular forces such as dipole-dipole, quadrupole, dispersion, and hydrogen bonding are the dominating forces, then physisorption occurs.[34, 35] Physisorption is favoured in applications where the adsorbent needs to be easily regenerated. If the adsorption process that leads to the formation of new chemical bonds is dominant, then chemisorption occurs.[35] In chemisorption, the types of bonds may include metal-ligand or covalent bonding. Chemisorption is most often considered an irreversible process. Thus, chemisorption favours applications in which we want to ensure the adsorbate does not desorb and re-enter the environment. Chemisorption is a key process utilized in separation of toxic analytes from mixtures.[36-38] As an example, in the shipping industry, chemisorption has the potential to separate toxic gases like carbon monoxide and sulfur dioxide from benign gases like nitrogen and carbon dioxide in flue gas streams.

1.2 Environmental Pollutants and Removal Methodologies

With the increasing demand for industries, there has become a growing global concern over the amount of air pollutants in the environment.[39] Specifically, greenhouse gases (e.g., carbon dioxide, CO_2; and methane, CH_4)[40-43] and harmful air pollutants that remain in the troposphere (e.g., nitrogen oxides, NO_x; sulfur oxides, SO_x; and carbon monoxide, CO).[44-47] have a detrimental effect on Earth. With this in mind, it is important to try to find efficient methodologies that can be implemented in reducing these emissions.

These methods can be grouped into two main categories. Pre-combustion methodologies that rely on purifying an exhaust stream at the fuel source.[48, 49] In other words, through various purification processes, the precursors to NO_x, SO_x, etc. are removed before they can be combusted to form these harmful gases. This can be a challenging process since different fuel sources may have different impurities present. Post-combustion methodologies rely on removing harmful gases after they are formed.[50-52] This allows the technology to work independent of the source of the fuel and thus any industry can take advantage of these methods. The challenge is that we have to ensure that these harmful gases are trapped such that they cannot be re-emitted into the atmosphere. The options for trapping such gases are to store them in materials or to chemically react them with other compounds to form safer chemical chemicals that can be disposed of.

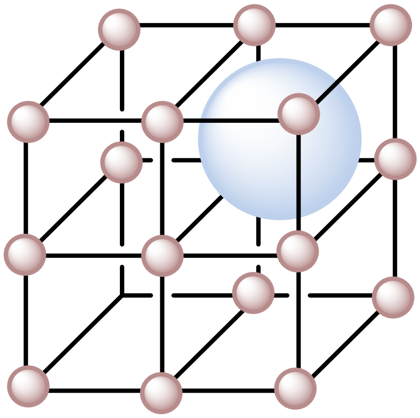

Figure 1.2. Interaction of toxic chemicals (represented by blue sphere) with the pores of MOFs.

For either pre/post-combustion methodologies to work, standards and government regulations must be in place and industries must monitor their pollutant concentrations in order to comply. Of course, this creates a causality dilemma in which the necessary technology must be available in order for the standards and regulations to be met. This forces the need for a mature technology to exist and be implemented. With the goal of reducing emissions, this thesis explores post-combustion adsorption of SO_2 and the molecular sieving potential of CO_2 from CO.

1.3 Sulfur Dioxide and the Environment

Sulfur dioxide is the primary component of a group of gases referred to as SO_x. SO_x refer to any group of compounds containing both sulfur and oxygen (e.g., sulfur oxide, SO; sulfur dioxide, SO_2; and sulfur trioxide, SO_3). These gases are predominantly present in the atmosphere through the burning of fossil fuels, specifically coal and sulfur-containing low-grade oils.[53, 54] As SO_2 gas has the highest concentration of sulfur oxide gases in the troposphere, it is predominantly used as the indicator for the amount present in the environment.

SO_2 gas that is found in the atmosphere poses a risk to both human and environmental health. Regarding human health, short-term exposure of SO_2 can lead to respiratory issues, such as asthma or chronic bronchitis.[55-58] Higher concentrations in the environment may additionally lead to other health issues such as pulmonary oedema.[59, 60] At high enough concentrations, SO_2 may react with other compounds in the atmosphere to form particulate matter (PM).[61] PM can enter deeper into the lungs, causing serious health issues (e.g., lung cancer or death related to respiratory disease).[39, 62-65]

Regarding the environment, SO_2 is a precursor responsible, in part, for the formation of acid rain.[66-69] Acid rain occurs by wet deposition in which sulfuric acid is deposited on the ground by mixing with snow, rain, or fog.[70] Acidic sulfuric acid particles may also be deposited on surfaces, such as the ground or trees, which is known as dry deposition.[70] By altering the pH of these surfaces to be more acidic, there is a direct impact on the ecosystems present in the environment.[67, 71, 72] When acid rain seeps into soil, it dissolves certain nutrients necessary for plant growth (i.e., calcium) and releases aluminum.[73] The presence of aluminum in the soil not only kills tree roots but may also lead to the depletion of wildlife such as fish.[74]

1.4 Sulfur Dioxide Capture Methods

As the government has implemented national quality standards for SO_2, industries have developed pre-combustion and post-combustion methods of capturing gases.[75] According to the Clean Air Act provided by the Environmental Pollution Agency, the primary standards for SO_2, which affect public health, is to not exceed a concentration of 75 ppb (ppb is parts per billion and has a value of 1 x 10^{-9} mol/mol) over a period of one hour.[76] The second primary standards, which affect the public welfare, are to not exceed 0.5 ppm, averaged over 3 hours, more than once a year.[76] All companies and industries must adhere to these standards to remain operable.

One area where these quality standards have a strong affect is in the transportation and shipping industry. The transport and shipping of goods is vital for an economy to function, but the transport of such materials is largely accomplished by the marine industry. The marine industry is a large contributor to atmospheric pollutants.[77-79] In fact, on a global scale, the marine industry accounts for 13% of SO_x emissions per year.[79] These ships are propelled by burning sulfur based low-grade oils. As SO_x standards are in place, these shipping companies can regulate their gas output by purchasing fuel with a low sulfur content. However, this option is a large cost for companies; thus, either the companies stop shipping or turn these costs onto the consumer. In Newfoundland, these costs can be seen in the price of a car which has a $1000 surcharge for getting the car to the island.[80] Given these challenges, it is evident that pre- and/or post-combustion methods of reducing SO_x without considerable cost is critical. As mentioned previously, post-combustion methods are more favourable than pre-combustion methods. A very common example in the marine industry is the process of flue gas desulfurization (FSD) via wet or dry scrubbing.[81, 82]

In wet scrubbing systems, limestone or lime is mixed with water to form a slurry that is subsequently released into the flue gas.[83, 84] The SO_2 present in the flue gas reacts with the slurry to form an aqueous solution, which requires safe disposal. In dry systems, the sorbent material is introduced into the flue gas stream as a solid material (e.g., limestone pellets). Most post-combustion methods use scrubbers which suffer due to low gravimetric activity (e.g., limestone that is only 10-20% active by weight). As such, 80-90% of the weight of the absorber is inactive. For companies like Oceanex, which use 200 tons of fuel per trip between St. John's and Montreal, 6 tons of SO_2 is formed requiring 60 tons of limestone.[80] Not only is limestone not a great sorbent, but the mass of material acquired to neutralize 6 tons of SO_2 gas adds an extra cost for the company for storage of the limestone and disposal of the exhausted material.[80] Comparing the existing limestone technology, it illustrates the opportunity for MOFs in the field. As shown in Figure 1.3, while limestone has a nitrogen gas accessible surface area of 10 m^2/g, typical MOFs have nitrogen accessible surface areas of 1500-2000 m^2/g (measurements are done at 77K).[85] The data in Figure 1.3, clearly illustrates the potential for MOFs in replacing existing solid scrubbers. If the 100 times fold increase in surface area has a surface with similar reactivity to SO_2, then there would be a 100 times fold decrease in the necessary amount of scrubbing weight needed for a trip and a concomitant decrease in produced waste. Despite this, there is little existing research that uses MOFs in SO_2 uptake.[86-92]

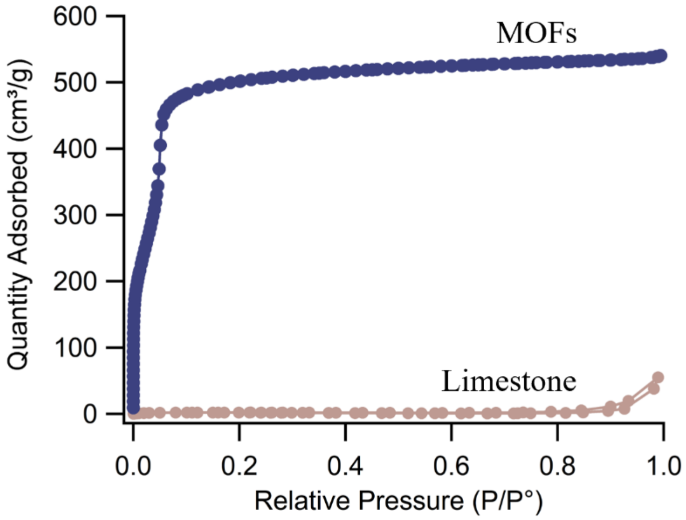

Figure 1.3. Comparison of the nitrogen isotherms in limestone vs. a typical MOF.

MOF research has focused on storing gases such as CO_2 and CH_4, but considerably less research has focused on SO_2 sequestration in MOFs. Carter et al. reported a record high SO_2 adsorption capacity of 12.3 mmol/g in a zirconium-based MOF known as MFM-601.[89] Along with the incredibly high adsorption capacity, the gas-uptake process is reversible and selective. Another example in the field is reported by Hungerford et al.[91] The group found substitution of the metal ion and organic linker in the parent MOF, $Zn_2(BDC)_2DABCO$, DMOF-1, showed favourable SO_2 uptake and improved structural stability in both dry and humid environments. The group tailored the parent MOF by substituting the BDC linker for 2,3,5,6-tetramethylterephthalic acid (H_2-Me_4BDC), and swapped the metal centres for zinc, nickel, copper, and cobalt. They also used other organic linkers including 1,4-naphthalenedicarboxylic acid (H_2-NDC), 2,5-dimethyl terephthalic acid (H_2-Me_2BDC), and 9,10-anthracenedicarboxylic acid (H_2-ADC) in the Zn-based MOF. The substitution of the linkers H_2-Me_2BDC to H_2-ADC lead to an improved structural stability in dry SO_2

environments. In humid SO_2 conditions, the ADC functionalized version of the zinc-based parent MOF, DMOF-1, showed the most favorable results in terms of structural stability.

1.5 Carbon Dioxide and the Environment

Solar energy that is emitted from the sun is absorbed at the surface of our planet and radiated back in the form of heat.[93] The heat is absorbed by greenhouse gases before it is radiated back through the atmosphere.[94] This is the necessary process by which our planet stays warm, with an average temperature around 15 °C.[95] In comparison, the atmospheric pressure on Mars is roughly 0.006 times lower than that of Earth, and Mars has an average temperature of -50 °C.[96] The more greenhouse gases present in our atmosphere, the more they are able to absorb larger amounts of heat and the higher the average planetary temperature. On earth, CO_2 is the main greenhouse gas released by anthropogenic sources in the environment.[97] Specifically, CO_2 accounts for 80% of the amount of greenhouses gases released via human activities in the United States.[98] The primary sources of CO_2 are from the transportation, electricity, and energy field.[99-102] These gases are mostly present in the atmosphere through the combustion of fossil fuels, specifically coal, natural gas, and oil.[94]

The presence of high amounts of CO_2 in our atmosphere are causing a wide variety of environmental and health concerns.[39, 103-107] For example, the greenhouse effect of such gases is resulting in warmer temperatures, rising sea levels, and having a drastic impact on weather changes.[99, 103, 108] In regard to human health, research has shown that indoor levels of CO_2 may cause dizziness, headaches, and reduced cognitive abilities.[105, 109-111] As such, it is vital for research to be implemented in eliminating or reducing such gases from indoor and outdoor environments.

1.6 Carbon Dioxide Capture Methods

Similar to that of SO_x gases, the levels of CO_2 that are released into the environment must be monitored. The main source of CO_2 is via the transportation, electricity, and energy sectors; therefore, the most effective way to reduce CO_2 emissions is to reduce the amount of fossil fuel consumed by these fields. With this in mind, the Environmental Pollution Agency has a guideline of strategies that can be implemented by such industries to eliminate the production of CO_2 gas. In terms of methodologies, CO_2 is the direct product of the combustion of fossil fuels, and as such, pre-combustion methods are not possible. Therefore, industries have focused their attention on using post-combustion methods.[51, 112]

In a direct comparison with how SO_2 is captured via post-combustion methods; CO_2 gas is captured by using liquid amines.[112-114] This process is commonly referred to as amine treating. A solution of alkylamines is mixed with a flue gas stream, where it is able to react with CO_2 to form the carbonate salt.[115, 116] The mixture is then heated in a still, where the amine is able to be separated from the CO_2 gas.[116] The amine solution is able to be cooled down and reused, whereas the CO_2 gas is released in the form of steam and condensed down, where it can be disposed of or further utilized. Thus, in this post-combustion method, CO_2 is able to be scrubbed/removed from the flue gas prior to being released into the environment.

Although this method is quite reliable, one notable drawback to this method is corrosion problems inside of the operating units.[117, 118] Also, this method is only utilized on CO_2 gas and hydrogen sulfide gas, whereas flue gases contain many other pollutants, including SO_2 and CO gas. A method in which all of the gases can be separated and disposed of using only one material, such as a MOF, would be the ultimate method in industries. If only one method was required for every gas present in flue streams, this would significantly reduce the financial costs associated with gas capture and disposal.

An abundance of research has focused on using porous materials to uptake CO_2 gas in the atmosphere.[119-123] In this work, we report a novel material that is able to selectivity sieve CO_2 from toxic gas mixtures by utilizing its unique pore features. Other work in the field has shown examples using chemisorption. For example, Siegelmen et al. have shown that Mg_2(dobpdc) (dobpdc^{4-} = 4,4′- dioxidobiphenyl-3,3′-dicarboxylate) was able to tether or cap the ends with diamine to form Mg_2(dobpdc)(diamine).[124] In doing so, the group was able to show that CO_2 was able to insert itself into metal-amine bonds to form ammonium carbamate chains. This group was able to synthesize a variety of these materials, each with a different number of tethered diamines present, and these resulting materials showed high CO_2 gas capacities.

1.7 Motivation of This Thesis

In this thesis, I have worked towards the application of MOFs for SO_2 and CO_2 adsorption. SO_2 adsorption often fits into two categories. Given the toxic nature of SO_2, it is often used as a toxic industrial chemical in chemical warfare. Under these conditions, SO_2 adsorption at large mixing ratios needs to be explored and the post-adsorption stability of the MOF does not need to be considered (i.e., the cost and reusability of the MOF is far less important than the cost of lives the MOF may save). However, for environmental applications, it is important to study SO_2 adsorption at low concentrations and the post-adsorption stability of the MOF is important from a regeneration and reusability point of view. With that in mind, Chapter 2 of this thesis explores the generation of SO_2 at low concentrations, with some preliminary work on the adsorption of SO_2 into MOFs. With regard to CO_2, there is a considerable amount of CO_2 adsorption literature in MOFs. One of the challenges with CO_2 adsorption is the issue of competitive binding. Gases such as water vapour, nitrogen, oxygen, etc. are able to also adsorb onto the surface of the MOF. This decreases the efficacy of a chemisorption system considerably. In flue gas application, this may be less of an issue due to the high concentration of CO_2, but in direct capture of CO_2 in the environment, where the concentration is quite low, this may be very challenging. However, if a MOF can be designed such that CO_2 can pass through and the majority of other gases cannot (i.e., molecular sieving), then existing MOF technology (or other materials) can be used in tandem with existing MOF adsorbers to improve their real-world behaviour. To that end, Chapter 3 explores microporous MOFs for CO_2 molecular sieving applications.

Chapter 2

Development of a Sulfur Dioxide Gas Permeation Device

2.1 Introduction

As outlined in the introduction, one of the goals of this thesis is to study the adsorption properties of SO_2 in MOFs. Before these experiments can be carried out, a source of SO_2 gas must be constructed. The pros and cons for attaining SO_2 gas are detailed for two main methods: sourcing the gas directly from a company or synthesizing it in the lab.

SO_2 can be purchased in gas cylinders appropriate for use in the laboratory. These gas cylinders may contain high purity SO_2 gas, but typically come in the form of mixtures balanced with other gases such as air, nitrogen, or helium.[125] These balance gases are typically unreactive with SO_2. Of course, for the success of a project, it is important to know what mixing ratios (i.e., concentration of SO_2 in an inert gas matrix) is needed. However, as research progresses, new experiments are designed to test different hypotheses and different mixing ratios are required. Assuming a sufficiently high enough mixing ratio of SO_2 is purchased to accommodate any experiment, an additional gas mixer must be purchased. This creates the problem of needing a gas mixer that can safely work with SO_2 and the added problem of dealing with the corrosive and toxic nature of SO_2. Due to toxicity, if gas mixers are used, it requires the necessary sensors to indicate a gas leak. In fact, companies like Praxair often state that SO_2 cylinders should not be used with gas mixing systems. While this may be the easiest option, from a safety and cost-effective approach, gas cylinders filled with SO_2 gas may not be the best option.

A more ideal approach to forming SO_2 in the lab would be to utilize a chemical reaction that produces the gas. There are a variety of reactions that produce SO_2, but an ideal reaction is one that can be easily controlled. A controlled reaction would enable the reaction to be easily started, stopped, and adjusted for different applications by changing the mixing ratio. The ideal reaction would be able to tune the output SO_2 concentration by adjusting the amount (concentration/mixing ratio) of at least one of the reagents – this can be done by changing the initial concentration of the reagent(s) or possibly the temperature under which the reagents are kept. If such a reaction can be found, then a tunable SO_2 gas stream can be produced. This reaction would produce the safest working environment possible during the research project. There are two common methods by which SO_2 can be produced. As shown in Equation 2.1, the reaction between copper metal and sulfuric acid, in the presence of heat, can produce SO_2.[126]

$$\mathrm{Cu(s)} + \mathrm{2H_2SO_4(l)} \xrightarrow{\Delta} \mathrm{CuSO_4(aq)} + \mathrm{SO_2(g)} + \mathrm{2H_2O(l)} \qquad \text{(Eq. 2.1)}$$

Alternatively, as shown in Equation 2.2, the reaction between any acid (i.e., a proton source) and a source of sulfite can also produce SO_2 gas.[127]

$$\mathrm{2HX(aq)} + \mathrm{SO_3^{2-}(aq)} \longrightarrow \mathrm{SO_2(g)} + \mathrm{2X^{-}(aq)} + \mathrm{H_2O(l)} \qquad \text{(Eq. 2.2)}$$

These reactions can occur at room temperature and are relatively cheap. Given that Equation 2.2 can be done with any acid source (e.g., HCl, HNO_3, H_2SO_4, or CH_3COOH) and there are several sources of sulfite or even bisulfite (Na_2SO_3 and $NaHSO_3$, respectively), we have opted to investigate this reaction.

The reaction between Na_2SO_3 and HCl is an acid-base reaction that produces sulfurous acid and a salt (Equation 2.3). The sulfurous acid intermediate that is produced does not exist in solution.[128] The thermodynamic instability of the sulfurous acid intermediate ultimately leads to the immediate dissociation of sulfurous acid to SO_2 and water (Equation 2.3).[128] Thus, the reaction between Na_2SO_3 and HCl ultimately forms SO_2 in solution. The amount of SO_2 produced will depend on the molar ratios of the two reagent solutions. In principle, the amount of SO_2 released can thus be controlled. If the proposed chemistry for generating SO_2 can be proven, then the method can be implemented in combination with a gas permeation system (see section 2.2.2).

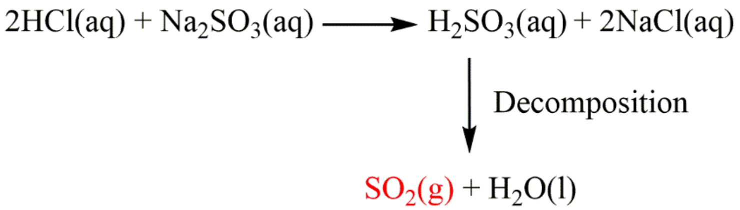

$$\begin{tikzcd} 2HCl(aq) + Na_2SO_3(aq) \arrow[r] & H_2SO_3(aq) + 2NaCl(aq) \arrow[d, "\text{Decomposition}"] \\ & SO_2(g) + H_2O(l) \end{tikzcd}$$

(Eq. 2.3)

Although this reaction works effectively in solution as seen by multiple trial experiments, there are several draw backs to producing a gas in a solution-based reaction. For example, as our final goal is to generate gas-phase SO_2 to investigate adsorption of SO_2 in MOFs, we need to ensure that all, or at least a constant amount, of the produced SO_2 gas is released from the solution. Furthermore, if the concentration of the gas is to be kept constant, then the reaction must always be maintained at a steady state. As the concentration of either reagent changes, the concentration of dissolved SO_2 and thus the mixing ratio of SO_2 gas will also change. To circumvent this, it would be necessary to maintain a large concentration of one of the reagents and a slow addition of the second to maintain some kinetic control of the reaction. While this is possible, it may be more practical to change the phase of the reagents. For example, if HCl gas can be flowed over solid sodium sulfite (Equation. 2.4), then it may be possible to displace SO_2 gas with HCl gas. Analogous reactions are well-established to occur under ambient conditions.[129]

$$2HCl(g) + Na_2SO_3(s) \longrightarrow SO_2(g) + 2NaCl(s) + H_2O(l) \qquad \text{(Eq. 2.4)}$$

The rational behind not using SO_2 gas from a gas cylinder is that the gas is toxic and corrosive. In Equation 2.4, HCl gas is being proposed, which is also toxic and corrosive.[130] In staying with the theme that I would like to produce SO_2 gas in the safest way possible, I turned my attention to finding a method of using HCl solutions as a source for HCl gas. At room temperature and atmospheric pressure, HCl exists as a gas.[130] If HCl is placed in a solution, then it will be energetically favorable to emit gaseous HCl. This property can be manipulated to form a system in which HCl escapes a gas-permeable container and subsequently flows over a sulfite salt using an inert gas carrier (e.g., nitrogen) to produce SO_2 gas. A gas-permeable container is often called a permeation tube and an instrument that utilizes permeation tubes to generate a constant gas mixing ratio is called a permeation system.

2.1.1 Gas Permeation Tubes

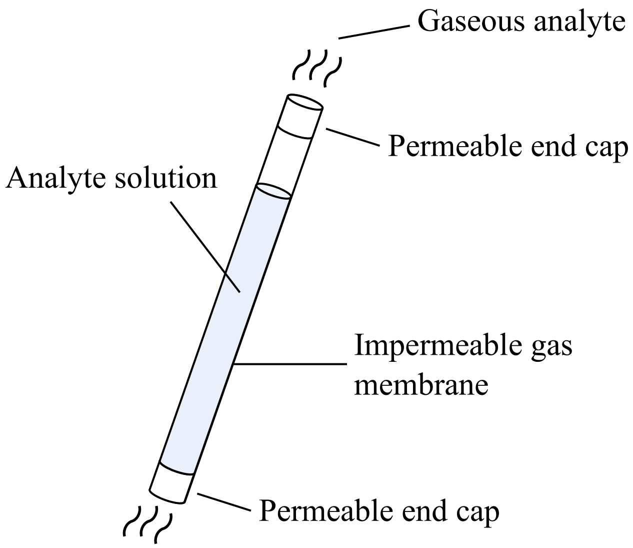

Figure 2.1. Schematic of a permeation tube.[131]

Gas permeation tubes are relatively easy to construct (Figure 2.1). The body of the material is constructed from an impermeable material while the endcaps are constructed from a gas permeable material. The amount of gas that escapes through the permeable end caps depends on the diameter of the end cap, concentration of the dissolved gas, and the temperature of the permeation tube.[22, 132] The gas permeates through the end caps by diffusion according to Fick's second law of diffusion (Eq. 2.1). The length of the tube governs how long a permeation tube will operate before it is exhausted; the longer the tube, the more material can outgas over time. A 5 cm long tube with 5 mm wide end caps can last years at a modest temperature of 30 °C. Increasing the temperature of the permeation tube results in an increase of emitted gas. The outgas from the permeation tube may also be controlled (increased or decreased) by altering the concentration of the acid in the tube. Given that a permeation tube utilizes a solution to generate the desired gas, the advantage of a permeation tube, as compared to a gas cylinder, is that it can be stored at ambient pressure and requires significantly less volume of material; this reduces the hazards associated with HCl gas.

2.1.2 Gas Permeation Systems

In general, a gas permeation system is an instrument designed to heat a permeation tube to a constant temperature while ensuring a constant flow of inert carrier gas (e.g., nitrogen gas). This produces a constant gas mixing ratio determined by the properties of the permeation tube, the gas flow rate, and the temperature of the permeation system. The produced gas can be used directly in a reaction, or it can be flowed over another material to undergo a reaction to produce another gas. In the examples above in section 2.1, the produced acidic gas can react with a solid sulfite source to undergo a solid-gas phase reaction, also known as a displacement reaction. Gas permeation systems are often custom-built insulated assemblies.

VandenBoer and Young have demonstrated the success of gas permeation systems. They have developed a gas phase source for perfluoroalkyl acids to examine atmospheric sampling methods.[129] Their work outlined the success of using acid displacement reactions with an acid (HCl or HBr) and various sodium perfluorocarboxylic acids to produce the corresponding acids.[129]

$$\mathrm{HX(g) + NaPFCA(s) \longrightarrow NaX(s) + PFCAH(aq)} \qquad \text{(Eq. 2.5)}$$

The gas permeation system used above was also customized for other environmentally relevant gases. By substituting the salt in the displacement reaction, other gases can be produced. Recent research by McGrath et al. has successfully used a permeation system to produce nitrous acid gas using a displacement reaction between HCl gas (generated from a permeation tube) and sodium nitrite as shown below in Equation 2.6.[22]

$$HCl(g) + NaNO_3(s) \longrightarrow NaCl(s) + HONO(g) \qquad \text{(Eq. 2.6)}$$

2.1.3 Hypothesis

Given the success demonstrated with other gas permeation tubes and gas systems, we propose to use similar chemistry to produce SO_2 gas.[133] We hypothesize that a permeation tube filled with HCl would be able to undergo a displacement reaction with sodium sulfite and/or sodium bisulfite to produce a constant and tunable mixing ratio of SO_2 gas. Once a constant source of SO_2 is able to be reproduced, we propose that exposure of MOFs to SO_2 gas will result in an uptake of that gas. By testing a number of different MOFs to the gas permeation source, we should be able to find a material that is capable of adsorbing SO_2 gas.

2.2 Results and Discussion

2.2.1 Solution-Based Experiments

The long-term goal of the project is to study SO_2 adsorption in MOFs. The first challenge in this goal is to produce a stable and safe SO_2 gas source via a permeation system. However, given that these instruments are custom built, taking yet another step backwards is important to ensure that a permeation system would be a successful approach. To that end, a set of experiments need to be explored to ensure that the proposed chemistry in Equation 2.4 is possible (i.e., the reaction between HCl gas generated via a permeation tube and sodium sulfite successfully produces SO_2). At this stage, this requires us to be able to detect SO_2 gas but not necessarily quantify the amount of gas produced.

Given that SO_2 is colorless, some methods by which it can be detected include spectroscopic method (e.g., IR), or by reaction with a colorimetric indicator.[134] SO_2 is a reducing agent and as such, it reacts with oxidizing agents. Although this reaction can be quite exothermic and dangerous, at sufficiently low concentrations and mixing ratios, such a reaction is expected to be relatively safe. Potassium permanganate ($KMnO_4$) is a strongly coloured oxidizing agent. The reaction between $KMnO_4$ and SO_2 (Equation 2.7) is expected to produce solid manganese dioxide (MnO_2) which would render an equimolar or sub molar, relative to the sulfite source, purple permanganate solution colourless.[135] Thus, a color change from a purple solution to a colorless solution would be indicative of a positive test for SO_2. While it is possible for the HCl solution to be oxidized via the $KMnO_4$ solution to yield chlorine gas, no evidence of this by-product was observed. These color changing reactions were only utilized as proof-of-concept qualitative tests, prior to purchasing an expensive SO_2 gas analyzer instrument.

$$3SO_2(g) + 2KMnO_4(aq) + 2H_2O(l) \longrightarrow 2MnO_2(s) + K_2SO_4(aq) + 2H_2SO_4(aq) \qquad \text{(Eq. 2.7)}$$

A general experimental setup can be seen in Figure 2.2. 100 mL of a 0.250 mol/L sodium sulfite and 50 mL of a 1 M solution of HCl were added to a round bottom flask heated to 50 °C. The round bottom flask was connected via glassware to a second round bottom flask containing 0.100 M potassium permanganate. A gentle flow of nitrogen gas was introduced to the first round bottom flask by hooking a line of tubing up to a nitrogen cylinder.

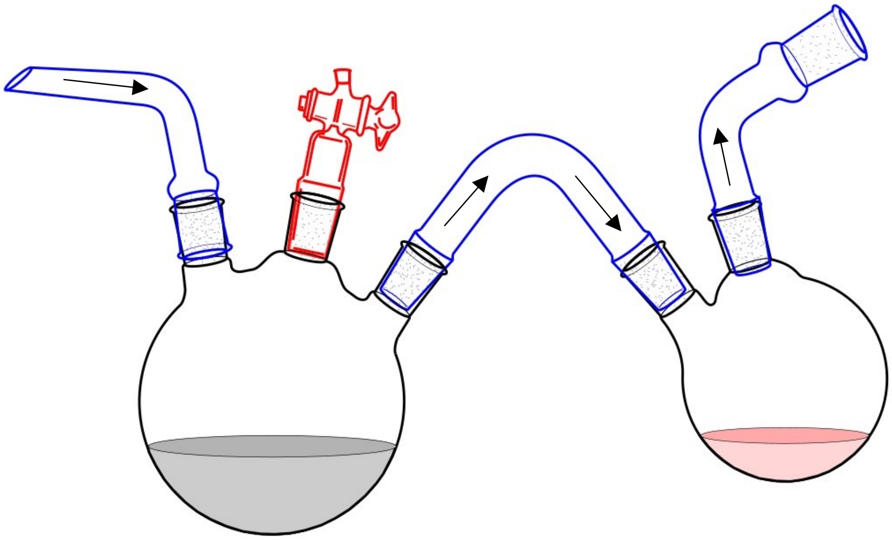

Figure 2.2. General schematic of the solution-based tests used in the production of SO_2; nitrogen flow (blue), acid addition (red), sodium sulfite solution (grey), and potassium permanganate solution (pink). Arrows are marked for the direction flow of the SO_2 gas, as carried by nitrogen gas.

Evidence of gas production was observed by the presence of vapours and condensation on the walls of the first flask overtime. These physical observations illustrate the exothermic nature of the reaction between the acid and the sulfite. After about an hour, the $KMnO_4$ solution exhibited a noticeable change in appearance. The dark purple solution lightened to form a brown solution. After another hour, the brown solution turned into a colorless solution and a dark brown/black precipitate (Figure 2.3) was formed. We hypothesize that the observations indicate that SO_2 was formed, and the dark precipitate is likely MnO_2.

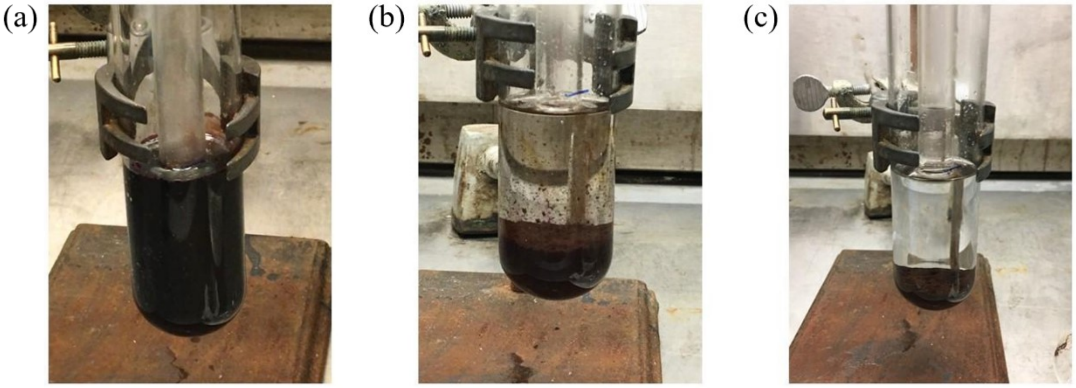

Figure 2.3. Initial $KMnO_4$ solution (a), lightening of the purple $KMnO_4$ solution to a light brown solution (b), and final result showing the brown solution has turned into a colorless solution and the presence of a dark brown precipitate (c).

To confirm our hypothesis, we completed control experiments to confirm whether SO_2 was being produced by the combination of the acid and the salt or by each reagent individually. To test this, each of the starting materials were made in solutions and were placed in individual glassware. We repeated the reaction with a heated HCl solution, and with a heated Na_2SO_3 solution. In either experiment, the permanganate solution remained unchanged. These control experiments confirmed that both the salt and the acid are needed for the reaction to occur. Based on these results, we were confident that we could produce SO_2 gas in the lab, but we wanted to further explore the reaction conditions to examine the effect of certain variables on the evolution of SO_2 gas.

To further explore the solution-based chemistry, we explored more variables associated with the reaction (e.g., reagent concentration and heat). We first tried halving the starting material concentrations to ensure that low concentrations of reagents, which is more reflective of the displacement reaction that I am exploring, were still able to produce SO_2.

Rather than taking an hour to react to form the insoluble material, at half concentration in both SO_2 and $KMnO_4$, the reaction took 25 minutes for the permanganate solution to change into a colorless solution. This suggests that at smaller reagent concentrations, more similar to realistic environmental conditions, we are still able to produce low concentrations of SO_2 gas.

To explore the effect of temperature on the reaction, we repeated the reaction in the absence of a heating element and found the confirmative color changes still occurred. To understand how much SO_2 was produced, we repeated the experiment with different amounts of $KMnO_4$. $KMnO_4$ solutions containing 7013 ppm, 701.3 ppm, 70.13 ppm, 14.03 ppm, 7.013 ppm, and 0.7013 ppm were made. At concentrations above 70.13 ppm, I could not visually observe any color change; therefore, not enough SO_2 gas was being produced to react with all of the $KMnO_4$ in solution. The concentrations that were 14.03 ppm and less all resulted in a color change from dark purple to colorless in less than an hour. Based on these results, we hypothesize that only small amounts of SO_2 gas are being produced that actually react with the $KMnO_4$ solution. To examine if the issue was with the outgassing of SO_2 from solution, the aqueous solution containing the acid and salt was combined with a concentrated $KMnO_4$ solution. Upon adding this, the solution remained colorless until a relatively large amount (>>14.03 ppm) of $KMnO_4$ was added to completely neutralize the solution. This indicates that the low SO_2 gas yield is due to the gas escaping the solution rather than poor reaction kinetics in producing SO_2.

2.2.2 Gas-Based Experiments and Modifications to Form a Permeation System

The experiments in the previous section demonstrate that SO_2 can be produced in solution. However, for a permeation system to be successful, the same chemistry must occur between the gaseous vapours of one reagent (the acid) and the solid (the salt); the displacement reaction in Equation 2.4 (with gaseous HCl being produced from an aqueous HCl solution). The gas-based chemistry was tested by individually switching the phases of the reagents. In the solution-based chemistry reactions, both the salt and the acid were in aqueous phases. For a permeation system to work, the acid must be converted into a gaseous phase and the salt must remain solid.

First, the sodium sulfite solution was changed from an aqueous form to a solid salt that was further housed inside a round bottom flask. A solution of HCl was added directly via a syringe on top of the salt. After minutes, the potassium permanganate solution changed from a dark purple to a colorless solution. This indicates that the solution-based chemistry observed in the previous section works when solid sodium sulfite is used. This does not preclude the hypothesis that the small amount of acid is dissolving the sodium sulfite and the reaction is occurring in solution.

Next, the HCl solution was substituted for gaseous HCl. As shown in Figure 2.4, another round bottom flask was added to the experimental setup. The first flask contained an HCl solution that was heated over a hot plate. This round bottom flask should produce an adequate amount of HCl vapour. The round bottom flask containing the HCl solution was connected to a second round bottom flask that contained only the solid salt. Preliminary experiments showed no observed color change in the $KMnO_4$ solution, but some issues in the setup were observed.

The main issue noted in this experiment was the gas was not being flowed directly over the solid salt. Instead, the SO_2 gas entered the second round bottom flask where it encountered a large volume of free space in which the time it took to come into contact with the salt was far too long. To test this hypothesis, a piece of tubing was placed inside the neck of the flask containing the salt to direct the flow of the gas directly onto the salt. The concentration of the acid solution was also increased to 6 mol/L. After all these modifications to the system (Figure 2.4), a color change in the $KMnO_4$ solution was observed. At 1 mol/L HCl, the $KMnO_4$ did not completely react over a period of 60 minutes. Increasing the HCl concentration to 6 M resulted in the $KMnO_4$ changing colour after only 6 minutes. This suggests that the proposed chemistry works but the HCl concentration needs to be higher to account for the slow outgassing from the solution. This also confirms that the solution-based chemistry that was attempted in section 2.2.1 is operable in a solid-gas phase reaction (i.e., a displacement reaction).

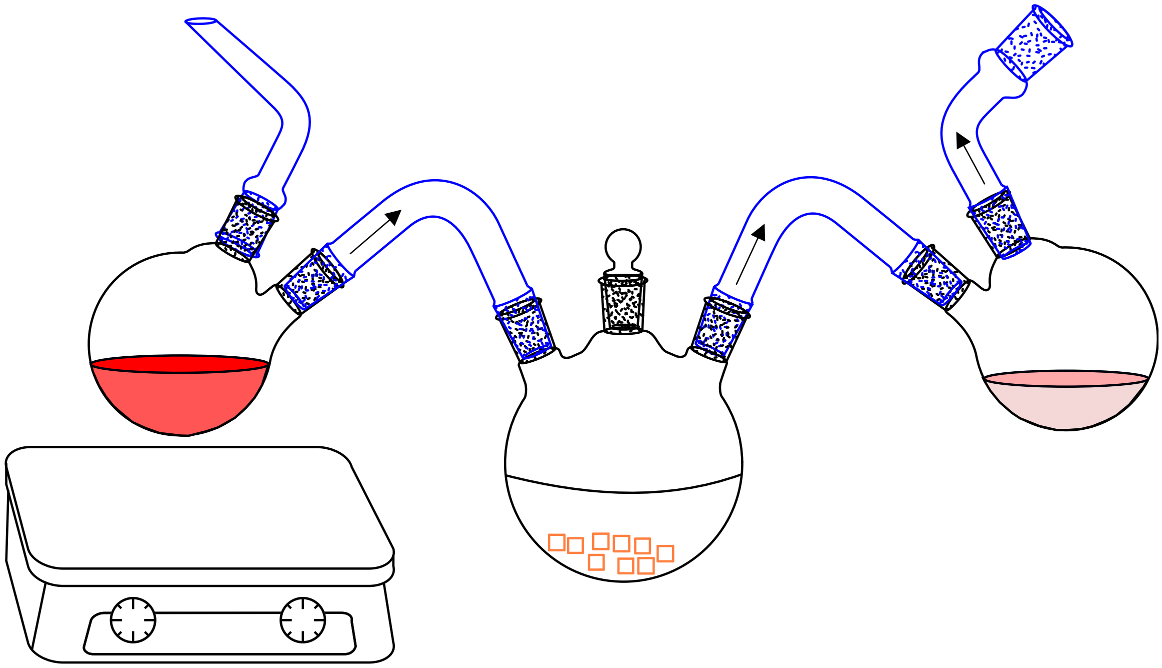

Figure 2.4. General schematic of the gas-based experiments; HCl solution (red), Na_2SO_3 salt (orange squares), nitrogen flow (blue), and $KMnO_4$ solution (pink). Arrows are marked for the direction flow of the SO_2 gas as forced by a steady nitrogen gas flow.

With the solid-gas phase chemistry confirmed, there was only one more test to convince us that a permeation system is worth building and testing. Instead of a solution of HCl, we assembled a 6 mol/L permeation tube and used it as the HCl source. The HCl permeation tube was placed inside of the round bottom flask as shown in Figure 2.5. Although these test conditions did not have a temperature-controlled environment, we wanted to determine whether the same chemistry could happen in a system that closely reflected a gas permeation system as could be achieved. Once again, after an hour, the purple permanganate solution changed to a colorless solution. With all the above successful experiments, the next steps were to build an instrument that could yield a long-term stable environment that would result in a constant mixing ratio of SO_2 gas.

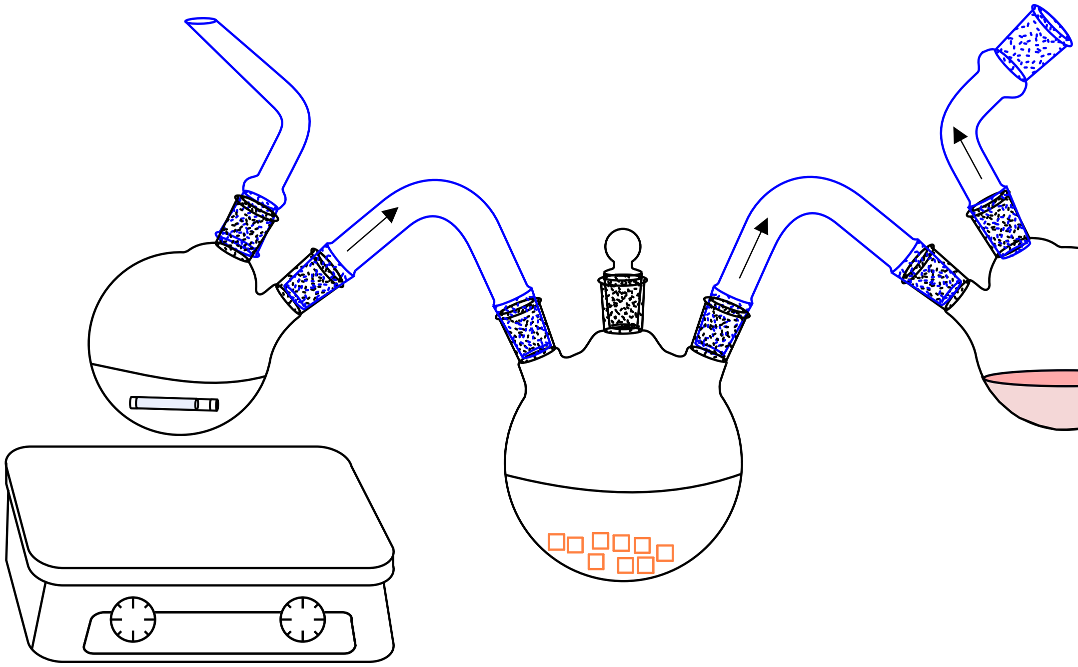

Figure 2.5. Schematic of testing an HCl permeation tube in the setup; sodium sulfite salt (orange squares), nitrogen flow (blue), and $KMnO_4$ solution (pink).

2.2.3 Building of a Gas Permeation System

The aim of a permeation system is to produce a constant mixing ratio of a gas, SO_2 in this case, over prolonged periods of times (days-months depending on the experiment). To that end, the permeation tube and the salt must be maintained at a relatively stable temperature during those periods of time. We accomplished this by building a permeation system as shown in Figure 2.6.

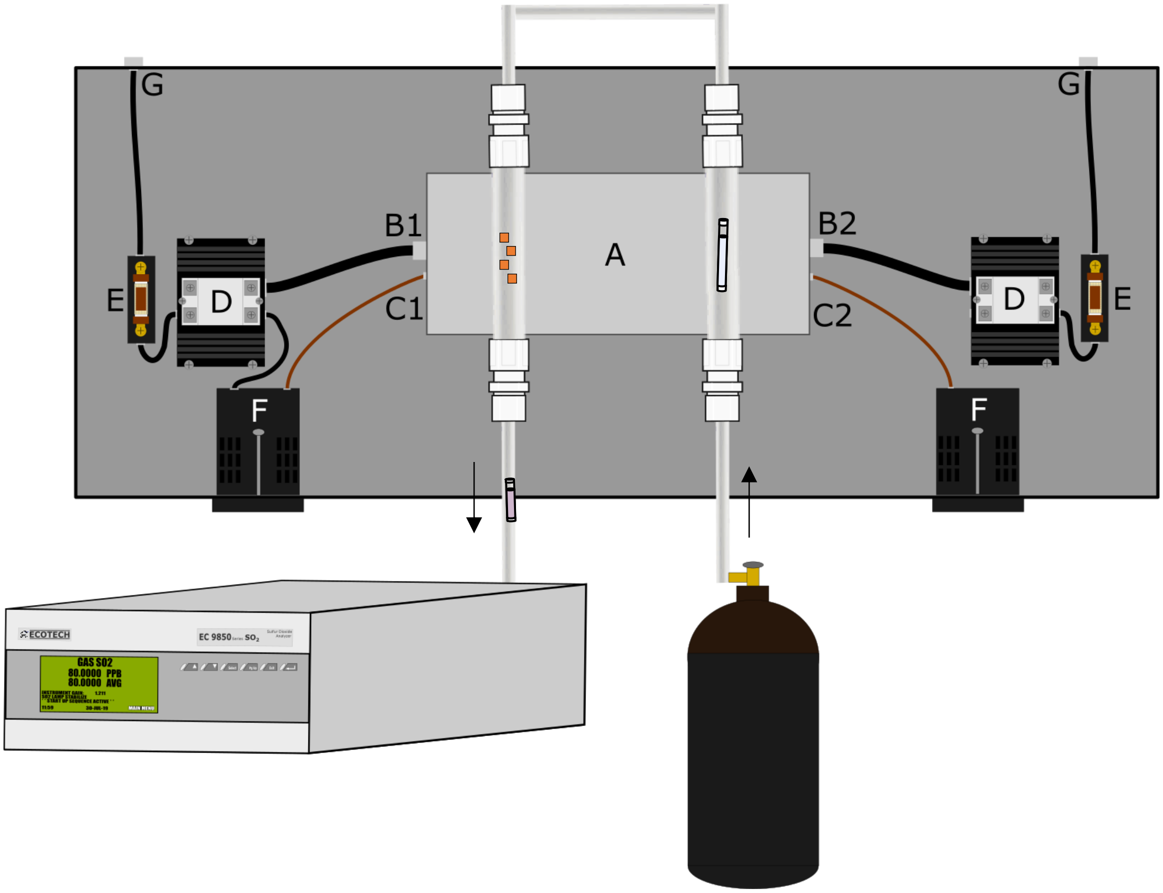

Figure 2.6. Gas permeation device outlining the electronic parts used; aluminum block (A), cartridge heaters (B), thermocouples (C), solid-state relays (D), fuses (E), temperature controllers (F), and (G) power supply. Arrow outlines the gas flow from the nitrogen cylinder, through the tubing housing the permeation tube, flows over the salt bed (orange squares), enters the tubing (where the MOF is eventually placed prior to breakthrough experiments) where it finally enters the EC9850 A detector.

In order to build a permeation system, we start with a large aluminum block (Figure 2.6, A) with two sample chambers, two heater chambers, and two thermocouple chambers. The purpose of the aluminum block is to maintain the temperature of the sample chambers with little temperature drift over long periods of time (i.e., when exposing a MOF to SO_2 gas at environmentally relevant concentrations). The first chamber houses the permeation tube, and the second chamber houses the salt. The heat is generated using a cartridge heater element (Figure 2.6, B) that is controlled by a PID temperature controller (Figure 2.6, D) that monitors the thermocouples (Figure 2.6, C) and adjusts the cartridge heater voltage accordingly. The heaters and thermocouples were placed at opposite corners of the aluminum block, running perpendicular to the sample chambers to try to ensure a constant temperature is maintained over the whole aluminum block. The function of each part required for heating the aluminum block, as well as a detailed description of the electrical parts necessary to install the heating parts can be found in section 2.4.5.

Although the $KMnO_4$ solution was useful in detecting large changes in concentration, a more analytical instrument was required for the purpose of this thesis. The specifications of the EC9850A Sulfur Dioxide Analyzer used in this thesis can be found in the experimental section (see section 2.4.1). For the gas permeation device used for SO_2 generation, the sample flow rate of the device was explored prior to any gas permeation experiments. A bubble flowmeter was used to measure the flow rate being provided by the nitrogen cylinder. Flow rates between 100 – 150 sccm (standard cubic centimeters per minute) were set using the bubble flowmeter and the SO_2 mixing ratio determined on the gas analyzer. The EC9850A Sulfur Dioxide Analyzer itself additionality provides a flow of 500 sccm via an internal pump to operate correctly.

2.2.4 Instrument Stability Experiments

With a working gas permeation instrument and a detector capable of measuring SO_2, we turned our attention to benchmarking the operation of the instrument. Although the ultimate goal is to test the adsorption capacity of SO_2 onto porous materials, in the absence of a stable permeation system, any adsorption experiment is meaningless. For the purpose of this work, stable concentrations are deemed by having a range of data that has a percent error of 5% or less over an extended time period (e.g., 6 hours). With a stable mixing ratio, the data being collected can be related to the adsorption capacity of the MOF. For example, if a stable output of 10 ppbv is reached, any changes in this mixing ratio, when exposed to a porous material, is likely due to interactions with the MOF. Integrating the adsorption and desorption curves from this plot, can result in determining the ratio of physisorption and chemisorption. However, if the source's mixing ratio does not stay constant, then the adsorption/desorption data is meaningless. To test the stability of the instrument, HCl solutions with molarities ranging from 1 mol/L – 6 mol/L were tested at different temperatures ranging from 30 – 60 °C.

Starting with a 1 mol/L HCl permeation tube at 40 °C, Figure 2.7 illustrates the SO_2 mixing ratio as a function of time. Although there is a small period where a relatively constant mixing ratio of 40 ppbv is observed, over the course of 1400 minutes (approximately 24 hours), the source had a 27% deviation with maxima around 70 ppbv and minima at 15 ppbv. This initial data, although promising, indicated that changes were necessary to establish a more stable source.

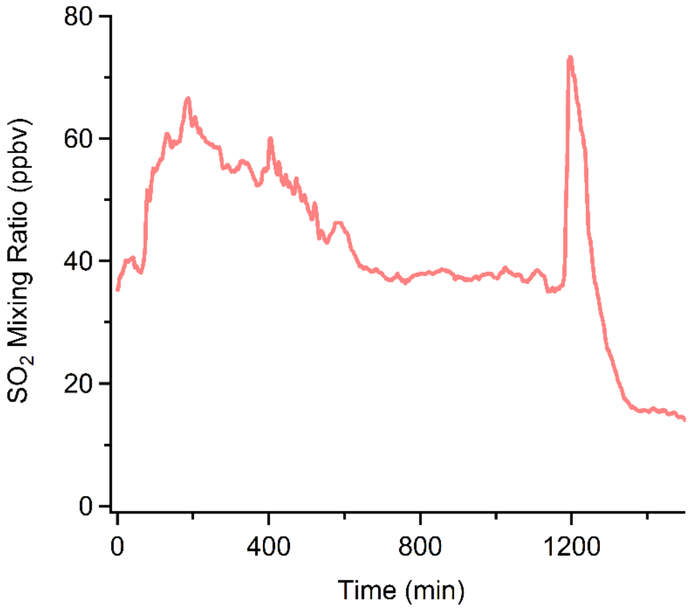

Figure 2.7. Observed SO_2 mixing ratio from using sodium sulfite as the salt source (data was collected using a nitrogen flow rate of 130 sccm, 1 mol/L HCl permeation tube, and a temperature of 40 °C).

Several external factors were explored to produce a more stable source. Given that SO_2 is a toxic gas, the gas generator was always placed inside of a fume hood such that any residual gas can be easily exhausted away. However, changes in the performance of the fume hood, due to changes in temperature, flow rate, or pressure, can lead to changes in the rate of cooling of the aluminum block and thus the temperature of the reagents inside the gas generator. To counteract the affect of the fume hood, the gas generator was first removed from the fume hood and placed in a low traffic area. Under these conditions, the effects of air flow and temperature should be minimized. Furthermore, the aluminum block was insulated with foam to reduce cooling on the surface of the block. Under these conditions, a thick layer of insulation would limit the effect of the external environment. Lastly, to reduce the risk of leaks, the quick connect fittings used in the gas permeation system, which are easy to remove and hence why they were used, were replaced with compression fittings and quartz fibre filters. This change ensured that the gas flow going through the instrument was constant with minimal-to-no leaks since compression fittings allow for a tighter gas seal. A full schematic of the external changes made to the gas permeation device is shown in Figure 2.8. Although these changes made a huge improvement in the experimental stability, there were still fluctuations observed in the data when the instrument was left for longer than 24 hours.

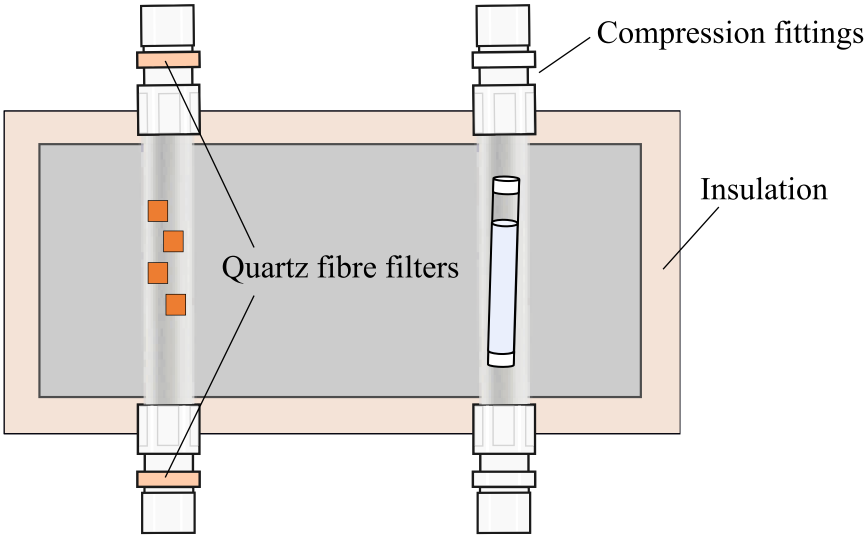

Figure 2.8. External improvements made to the gas permeation device; insulation around the aluminum block, compression fittings, and addition of quartz fibre filters in the compression fittings associated with the salt bed.

With the external variables exhausted, we turned our attention to the chemistry happening within the aluminum block. As mentioned throughout Chapter 2, sodium sulfite was proposed and used as the salt source for the reaction and HCl was used as the acid source to produce SO_2 gas. Given that existing work had shown the success of using HCl as an acid gas source, we hypothesized that there may be an issue with the sodium sulfite salt. With the idea that other salts may exhibit the same chemistry, sodium bisulfite was used for any subsequent reactions. As shown in Equation 2.8, the same chemistry occurs while using sodium bisulfite as with sodium sulfite.

$$\mathrm{HCl(aq) + NaHSO_3(aq) \longrightarrow SO_2(g) + NaCl(aq) + H_2O(l)} \qquad \text{(Eq. 2.8)}$$

To our surprise, after replacing the salt, an immediate improvement in the stability of the data was observed. As shown in Figure 2.9, the mixing ratio output remained stable over the course of 1500 minutes (25 hours). Under these conditions, a 1400 ppbv output with a 1.2% deviation was observed. This indicates that the gas generator can be used for gas adsorption experiments. It should also be noted that in the data collected in Figure 2.9, we increased the concentration of the HCl in the permeation tube from 1 mol/L to 4 mol/L. Although it would be more meaningful to compare the two different salts under the same experimental conditions, we wanted to outline a more meaningful set of data. With lower HCl concentrations (i.e., 1 mol/L HCl), any fluctuations in the observed SO_2 mixing ratio as a function of time would show larger percent deviations, as smaller amounts of HCl gas would be present for the salt to react with. With smaller SO_2 mixing ratios being produced, any change, whether it be minor or major, would have a larger impact on the percent deviation of the data.

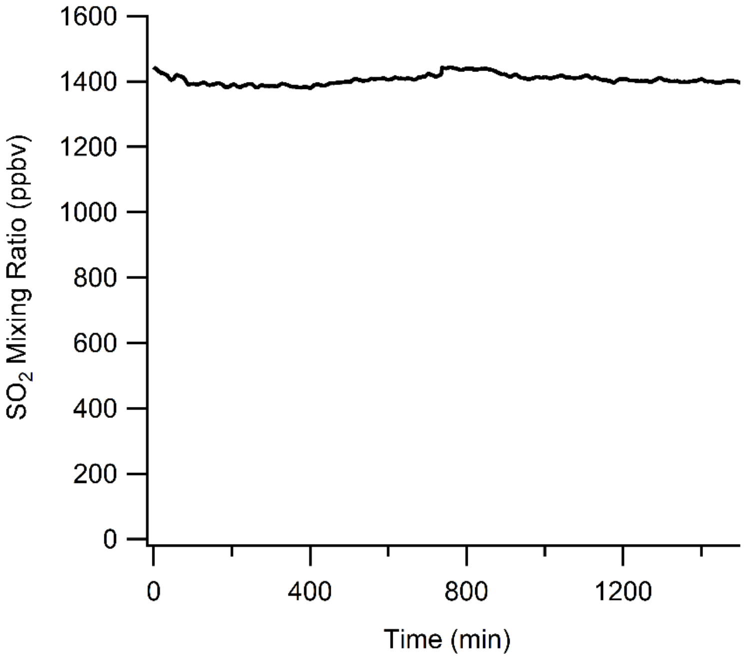

Figure 2.9. Observed SO_2 mixing ratio when using sodium bisulfite as the salt source (data was collected using a nitrogen flow rate of 130 sccm, 4 mol/L HCl permeation tube, and a temperature of 50 °C).

With a stable output of SO_2 achieved, we turned our attention to evaluate the effects of temperature and HCl concentration on the production of SO_2 gas. HCl solutions with molarities ranging from 1 mol/L – 6 mol/L were tested at temperatures ranging from 30 – 60 °C and the results are summarized below in Figure 2.10. The data points are an average of the data collected for each temperature over a period of 24 hours. In all four datasets, we see a proportional relationship between the HCl concentration and SO_2 mixing ratio.

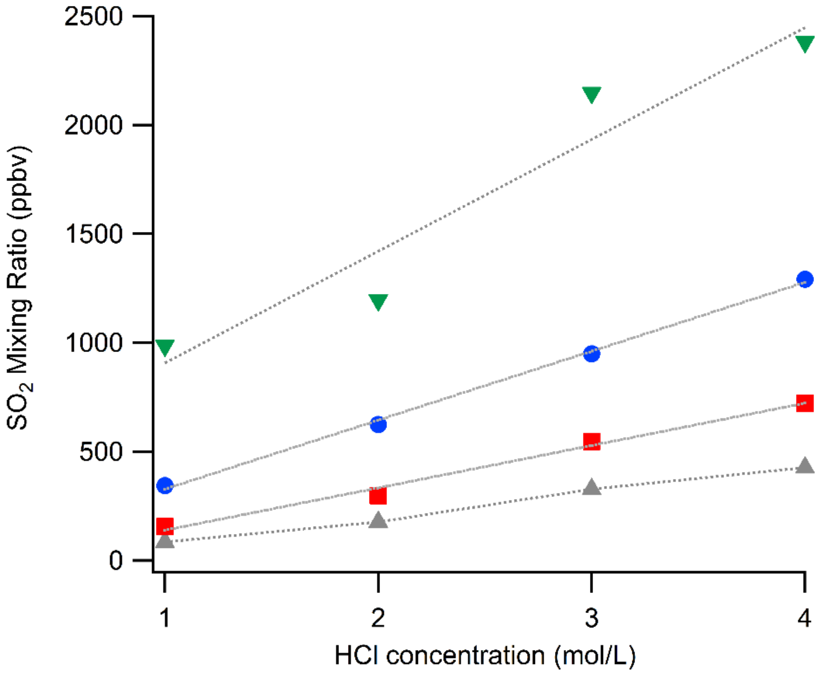

Figure 2.10. Observed SO_2 mixing ratio as a function of HCl concentration over a range of temperatures; 30 °C (black), 40 °C (red), 50 °C (blue), and 60 °C (green).

As evident in Figure 2.10, as we increase the concentration of HCl, we also increase the SO_2 mixing ratio. This result is expected, as we stated earlier that higher acid concentrations produce more gaseous HCl, which in turn reacts with the salt, and yields more SO_2 gas. Another trend can be observed as a function of temperature. As seen below in Figure 2.10, as we increase the temperature of the reaction, the SO_2 mixing ratio also increases. This same trend is observed the same in all four temperatures. In context, these experimental results show higher temperatures yield more SO_2 gas. Since the gas is housed inside of a permeation tube, we have to remember that permeation tubes are temperature dependent. In fact, the mixing ratio produced is directly proportional to temperature. The aqueous HCl solution housed inside of the permeation tube is emitted through the permeable membrane as a vapour based on its Effective Henry's Law constant.[132] Henry's law of solubility states that at a constant temperature, the amount of gas that dissolves in a liquid is directly proportional to the partial pressure of that gas at equilibrium with the given liquid.[136] The higher the temperature, the higher the quantity of HCl gas that is able to escape the permeable ends caps of the tube. According to Henry's law, we should observe a linear relationship between mixing ratio and the molarity of HCl used in the experiment. However, Fick's first law states the movement of particles from high to low concentration is directly proportional to the particles concentration gradient, which will change depending on the flow rate of the carrier gas. As such, the overall behaviour may not be linear.[131, 137, 138] According to Henry's law, we should observe a linear relationship between mixing ratio and the molarity of HCl used in the experiments.

Taking a closer look at the trend in each dataset, a linear trend is observed at temperatures ranging from 30 – 50 °C, as expected by Henry's law. Lower temperatures show a higher correlation factor, but at higher temperatures (i.e., 60 °C), the data seems to deviate from linearity. In fact, the dataset collected for 60 °C shows a poor linear correlation factor. The data also seems to deviate more severely at higher acid concentrations. It must also be noted that at 60 °C, the concentration data is not reproducible. Multiple attempts at trying to reproduce the data were unsuccessful; therefore, the dataset itself may not ultimately be that trustworthy. It is possible at this temperature, the rate of HCl gas escaping the permeation tube was no longer constant or the reaction between the acid and the salt bed was not reaching a steady state.

2.3 Conclusions

In summary, SO_2 gas was produced in both solution-based and gas-phase chemistry. It was shown that under a variety of different test conditions, sodium sulfite readily reacts with aqueous and gaseous HCl to yield SO_2 gas. With this chemistry in mind, we were able to implement the gas-phase chemistry into a permeation system. A custom-built SO_2 generator was designed and built.

The gas permeation device was shown to produce relatively constant SO_2 mixing ratios with the addition of external modifications. The external changes made to the gas permeation device was the addition of insulation to the aluminum block, switching the adaptors to compression fittings to allow for a tighter gas seal, and finally the addition of quartz fibre filters inside of the compression fittings to ensure no salt was able to pass through into the tubing. The biggest of changes made to the design was to swap the salt from sodium sulfite to sodium bisulfite. This result showed the largest improvement in stable SO_2 mixing ratios.

Experiments of varying HCl acid concentrations and temperatures showed a promising start. At 30, 40, and 50 °C, the datasets showed a linear trend between SO_2 mixing ratios and HCl concentration, and repeated experiments showed reproducibility. At 60 °C, the dataset strays from linearity but this result was not reproducible in any means.

The next step in this work would be reproducing the datasets for each temperature in triplicate to ensure the linear trend in SO_2 mixing ratio and HCl is correct. Once a stable source is acquired and quantified, initial MOF screenings for SO_2 adsorption can occur.

2.4 Experimental

2.4.1 General Materials and Instrumentation

All compounds were used as received: hydrochloric acid (ACP, 36.5-38%), nitrogen gas (Praxair, 99.9999%), sodium sulfite (ACP, 98%), and sodium bisulfite (ACP, 58.5%).

Quantitative SO_2 measurements were made using an Ecotech EC9850A Sulfur Dioxide Analyzer. The analyzer is an ultraviolet (UV) fluorescence spectrometer. A zinc discharge lamp provides the UV radiation. Using a bandpass filter, a wavelength of 214 nm is selected for the experiment. SO_2 molecules absorb this radiation and subsequently reemit it at a lower energy (fluorescence) between 300 and 400 nm. The emitted radiation perpendicular to the excitation beam is measured by a photomultiplier tube. The intensity is proportional to the mixing ratio of SO_2 gas. The range of detection of the instrument is from 0 – 20 ppm, with a lower detectible limit of 0.5 ppb or 0.2% of the concentration reading.[139] The data collection was measured in units of ppb.

For the EC9850A Analyzer to function properly, the instrument must pull in sample air at a flow rate of no less than 500 sccm. Most of this flow is being provided by an internal pump, which controls the flow rate by altering the pump speed. After the sample air enters the inlet port, it passes through a particulate filter that removes particles less than 5 micrometers. This filter is necessary to ensure only materials nonreactive to Kynar, Teflon, and Viton can pass into the detector to be analyzed. The filtered sample air is passed through a hydrocarbon kicker that has an internal membrane that eliminates any instrument interference of hydrocarbons. The instrument houses an internal zero air scrubber that provides SO_2-free air. As the sample enters the kicker jacket at 500 sccm, a flow of 2300 sccm is provided by the zero-air scrubber in the opposite direction. The difference in pressures between the two flow channels assists in diffusion of the hydrocarbons across the membrane and elimination of them via the exhaust. After the kicker jacket, the sample continues to flow at 500 sccm to the fluorescence cell.

2.4.2 Preliminary Solution-Based Experiments

To confirm that SO_2 could be produced in the gas-phase, preliminary experiments were done using a glassware setup (Figure 2.2). The first tests were completed using sodium sulfite salt as the SO_2 and HCl as the acid. A 1:2 ratio of Na_2SO_3:HCl was used as an initial starting point for the experiments. 3.15 g of sodium sulfite was dissolved in 100 mL of distilled water. A 1 mol/L HCl solution was prepared, and 50 mL was placed into a syringe. To prepare the color indicator, 1.58 g of $KMnO_4$ was dissolved in 100 mL of distilled water. This amount was calculated with the assumption all the starting material would react. For the setup, a nitrogen cylinder was connected via tubing to a round bottom flask containing a septum for the addition of acid, and this flask was connected to a bubbler by more tubing. Approximately 80 mL of the potassium permanganate solution was used to fill a bubbler and 100 mL of the salt solution was placed inside of the round bottom flask. 50 mL of 1 mol/L HCl was added through the septum directly to the aqueous salt solution. Any production of gas by these reagents was flowed via the carrier nitrogen gas directly into the permanganate solution.

To study the effect of reagent concentration, more experiments were completed using 0.70 g of $KMnO_4$ in 100 mL of distilled water which was less than half of the amount previously used to hopefully observe the color change quicker. 1.57 g of Na_2SO_3 in 100 mL of distilled water was used to make the salt solution and 25 mL of 1 mol/L HCl was also used.

2.4.3 Custom Instrumentation for SO_2 Generation

Approximately, a 5 cm piece of PFA (perfluoroalkoxy) tubing (ID = 1/8 in., OD = 1/4 in.) is capped at one end with a 0.5 cm long 1/8" PTFE (polytetrafluoroethylene) rod. The tube is filled with a HCl solution ranging from 1 mol/L – 6 mol/L and the other end is sealed with another identical piece of a PTFE rod. A heat gun was used to soften the PFA tubing prior to placement of the PTFE rods, ensuring the acid solution is completely sealed within the tubing. PTFE is permeable to HCl gas. The permeation tube was put inside of a 10 cm piece of PFA tubing (ID = 3/8 in., OD = 1/2 in.) and placed inside of the aluminum block.

A 10 cm piece of PFA tubing (ID = 3/8 in., OD = 1/2 in.) was used for placement of the salt. 3.00 g of $NaHSO_3$ or 3.00 g Na_2SO_3 was placed inside of the tubing and subsequently placed inside of an aluminum block. Both ends of the tubing were connected to compression reducing unions that reduced the tubing from 1/2 in. to 3/8 in. It was extremely important to ensure all materials used were compatible with SO_2 and that no fittings were made from metal because if any moisture were to be present in the system, SO_2 may react with water to form sulfuric acid which is highly corrosive. The compression reducing unions were made from polypropylene which has an excellent compatibility with SO_2.

An advantage of the compression reducing unions was that there was available space inside of the fittings that allowed for placement of filters. Filters are extremely important to have in the salt bed because salt can easily be transferred into the tubing via the nitrogen gas flow. The filters were added inside both reducing unions to prevent this from happening. The filters were made from quartz fiber which is a material that is chemically unreactive with acidic gases (e.g., HCl or SO_2).

The 1/2 in. PFA tubing housing the permeation tube was reduced to 3/8 in. PFA tubing via push-to-connect fittings. Push-to-connects are known as instant fittings and the tubing is gripped by an internal system that is easily disconnected by pushing on the gripping ring. They are much easier to use than compression fittings which, in turn, must be tightened using wrenches. A drawback to using push-to-connects instead of compression fittings is that they tend to be less gas-tight, but no loss of gas flow was observed for our system when they were used. The amount of nitrogen gas used as the flow rate for the reaction was tested to be equal pre and prior to the gas permeation device.

2.4.4 Electrical Materials

Copper wires were used to install electrical connections between the thermocouples, cartridge heaters, solid-state relays, fuses, and temperature controllers. Beginning at the aluminum block, the cartridge heaters (B1 and B2) were connected to the solid-state relays (D) and the thermocouples (C1 and C2) were connected to the temperature controllers (F). The temperature controllers (F) were each connected to individual solid-state relays (D) which subsequently were connected to fuses (E). If wire-to-wire connections were required, marrettes were utilized as electrical connectors.

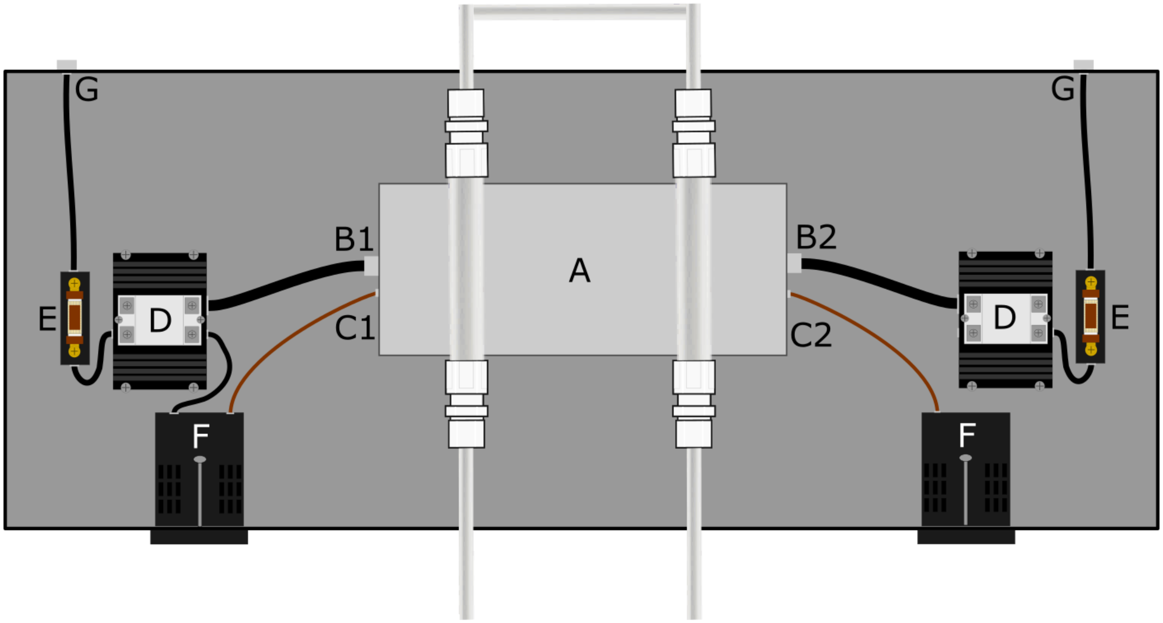

Figure 2.11. Gas permeation device outlining the electronic devices used; aluminum block (A), cartridge heaters (B), thermocouples (C), solid-state relays (D), fuses (E), temperature controllers (F), and (G) power supply.

2.4.5 Electrical Parts and Their Roles

The rate of HCl permeability in permeation tubes is dependent on temperature; thus, it is essential to have a temperature-controlled environment. A cartridge heater is a cylindrical shaped heating element used to provide uniform heating in an aluminum block.[132] Although other metals could be utilized as the metal block material, aluminum was selected due to its high heat capacity. The cartridge heaters were placed lengthwise inside of an aluminum block. Aluminum has a high melting point (660 °C) and is quite inexpensive. Overall, aluminum is a very good conductor of heat. Adjacent to the cartridge heaters are thermocouples (Figure 2.12, b). Thermocouples are sensors that measure heat, so for them to measure an accurate temperature in the aluminum block, it was important to have them as close as possible to the source of heat.[132]

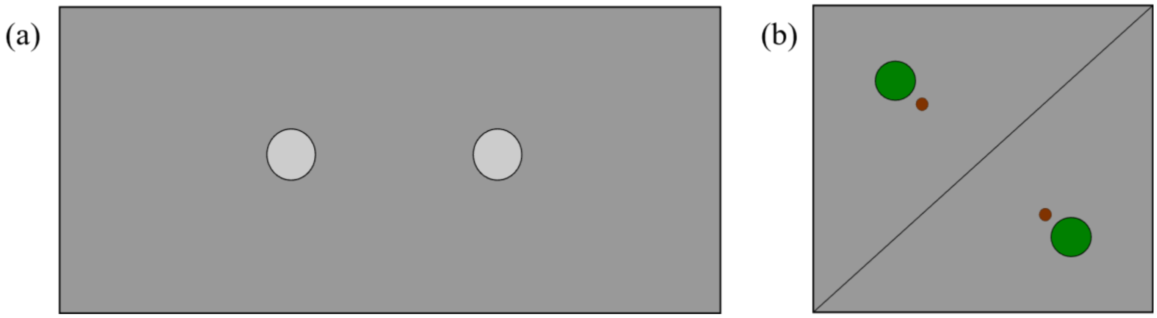

Figure 2.12. Side-view (a) and front-view (b) of the aluminum block showing where the necessary holes are for placement of the sample holders (side-view; a), cartridge heaters (green) and thermocouples (red) (front-view; b).

Solid-state relays are devices that switch on or off when an external voltage is applied across the terminals.[132] They control large resistance heaters when paired with temperature controllers. It is necessary to have both solid-state relays and temperature controllers, as one will not function without the other. The solid-state relays are mounted on finned heat sinks that are riveted on a thin sheet of aluminum metal. Fuses were installed parallel to the solid-state relays. Fuses were placed inside of fuse folders that were mounted with rivets. Fuses operate as electrical safety devices. If too much flow passes through the circuit, the fuse will be blown first instead of the more expensive devices. Once the fuse is blown, the electrical current is terminated and no further damage should occur (e.g., fire).

PID temperature controllers are devices that are used to regulate and control the temperature. They operate by reading the temperature that is sensed by the thermocouple as the output and compare it to the set-point that is selected by the temperature controller.[132] If the readout temperature is not at the desired temperature, it communicates an output through the solid-state relays to the cartridge heaters to either increase or decrease the temperature to whatever temperature is selected as the set-point on the controller.

Chapter 3

Microporous MOFs and their Applications in Molecular Sieving

3.1 Introduction

As outlined in Chapter 1, this thesis set out to explore two main ideas. In Chapter 2, we explored how to make SO_2 gas in order to study the adsorption of SO_2 in MOFs. In this Chapter we explore if MOFs with small pore apertures can be made and applied in separation studies. The primary gases of interest in this work are in the separation of exhaust streams. Gas separation can take many different approaches. On the one hand, we can make porous materials that are able to adsorb the target gas over the others. On the other hand, we can make porous materials that can adsorb all the other gases over the target ones. In either case, we can efficiently separate gases from one another. The challenge in either of these approaches is that the gas of interest has to be the most or least adsorptive of all the gases. With this in mind, it is easier to design a material that targets the adsorption of a target gas over the others. However, if the target gas is present in low abundance in the exhaust stream, then the porous material must be really reactive or highly selective. These approaches are not impossible, but there exists another way.

The kinetic diameter of a gas is a measure of how close atoms or molecules can be to one another before collision occurs. For example, nitrogen gas has a kinetic diameter of 3.60 Å while CO_2 has a kinetic diameter of 3.30 Å.[140] While initially this may seem counter-intuitive since CO_2 is longer than nitrogen gas, these numbers reflect the reality that the kinetic diameter is a measure of atomic width vs. length of the molecule. With this in mind, if a MOF can be designed with a pore aperture between two kinetic diameters, then the kinetic separation selectivity and the adsorption selectivity would be infinite and allow one gas to pass through while the other remains behind.

Excluding computational studies, the pore properties of a MOF can be determined in one of three different ways. The average width of a pore is determined via pore-size distributions. In this method, a gas adsorption isotherm (often N_2 at 77 K) is fit using a kernel.[141, 142] The kernel represents a mathematical model of isotherm shapes as a function of pore sizes. In essence, the computer is answering the question: how many of each type of isotherms, and thus pore sizes, does it take to reconstruct the observed isotherm. For this to work, an appropriate model is necessary to generate the kernel. While for MOFs there is some debate of the validity of the existing models, for smaller MOFs, the existing pore size distributions fit well and return results that are consistent with the crystallographic data. The pore functionality can be studied by looking at the isosteric heats of adsorption.[143] By collecting isotherms at different temperatures, but assuming the adsorption mechanism doesn't change, we can determine how much energy is released when a gas adsorbs onto a surface.[143] Determining kinetic diameter is a bit more challenging. The only way to determine the kinetic diameter of a MOF is to try to adsorb gas molecules of different kinetic diameters until one does not adsorb.[144] Of course, this also relies on the gas molecule having sufficiently high enthalpies of adsorption that a considerable amount of gas can adsorb at the measurement temperature and pressures being explored. For example, helium, which has a kinetic diameter of 2.60 Å, doesn't look like it adsorbs onto most MOFs at 77 K. This does not mean that the pore aperture of a MOF is less than 2.60 Å, it means that helium is not adsorptive enough at these temperatures and pressures. However, for common adsorbents like CO_2, methane, and nitrogen gas, this should not be an issue. Thus, assuming the pore aperture is approximately the size of a vapour/gas that can be studied, the pore aperture can be easily determined. Table 3.1 outlines different probe molecules that can be used for these size-exclusion sorption studies.[140, 145]

Table 3.1. Useful Probe Molecules for Size-exclusion Studies.

Gas Molecule	**Kinetic Diameter (Å)**
Methane	3.80
Carbon monoxide	3.76
Nitrogen	3.64
Sulfur dioxide	3.60
Carbon dioxide	3.30

Figure 3.1 helps illustrate what each measurement represents. If we assume a hexagonal shaped pore, such as those we will discuss in this Chapter and the blue shape in Figure 3.1, pore size distribution would return an average value for the width of the pore (Figure 3.1a). Isosteric heats of adsorption data would reflect the adsorption energy on the surface of the

pore (the blue hexagon). However, if we looked at a packing structure (Figure 3.1b), then the pore aperture is the smallest opening that leads into the pore. In the case of Figure 3.1b, assuming we extend the hexagon pattern indefinitely in 3D, the pore aperture is related to the opening illustrated in the figure.

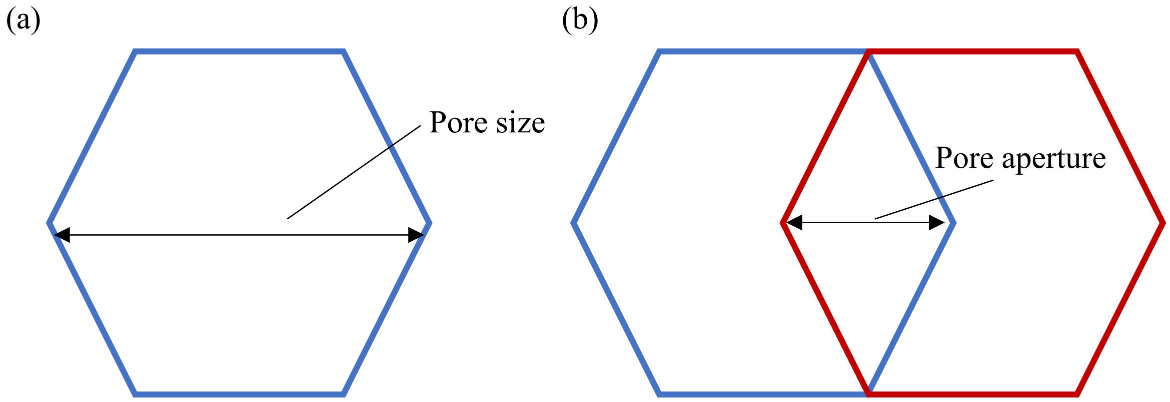

Figure 3.1. Single hexagonal-shaped pore (a) vs. two hexagonal-shaped pores overlapping to form a smaller cavity for gas molecules to enter through (b) illustrating the difference between pore size and pore aperture.

In this Chapter, we explore a new MOF whose structure suggests that it has a pore aperture in a region where molecular sieving of common gases is possible. In particular, we are interested in determining if we can sieve CO (kinetic diameter = 3.3 Å) from CO_2 (kinetic diameter = 3.76 Å). CO is a colorless and odorless gas that can be extremely detrimental to human health. Incomplete combustion processes lead to the formation of CO gas; therefore, in flue gas streams CO gas is present. In this work, we were interested in studying the molecular sieving properties of our materials on CO_2 and CO gas. If we can develop a system that first separates toxic CO gas from CO_2, we can then utilize another MOF material in tandem with our work to further adsorb CO_2 gas from the environment.

3.2 Results and Discussion

3.2.1 Synthesis of $Zn_3(NH_2BDC)_3DABCO$

Previously in the group, the synthesis of the MOF, $Zn_2(NH_2BDC)_2DABCO$ (NH_2BDC, 2-aminoterephthalic acid; DABCO, 1,4-diazabicyclo[2.2.2.]octane) was examined. While the non-functionalized $Zn_2(BDC)_2DABCO$ (BDC = terephthalic acid) MOF is trivial to synthesize, the amine-functionalized version has surprisingly very few reports.[62, 146] Under standard MOF-synthesis conditions (i.e., DMF at elevated temperature) a reproducible surface area could not be achieved.

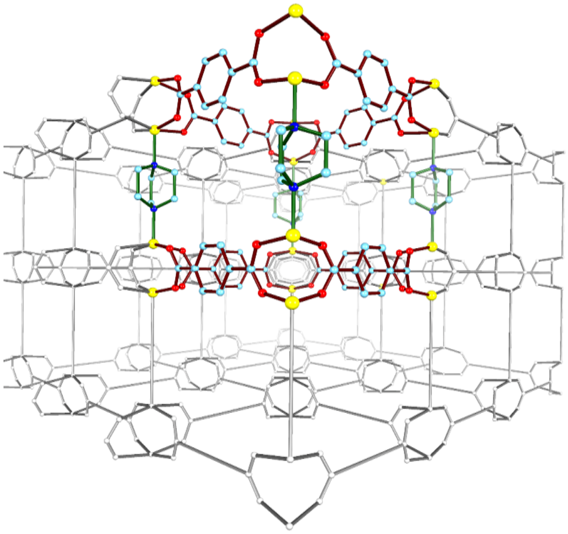

Figure 3.2. Crystal structure of $Zn_2(NH_2BDC)_2DABCO$ showing a 3-D representation of a pillared paddlewheel MOF; zinc (yellow), oxygen (red), carbon (light blue), and nitrogen (dark blue).[146]

$Zn_2(NH_2BDC)_2DABCO$ belongs to a family of MOFs known as pillared-paddlewheel MOFs (Figure 3.2).[146] In these MOFs, a pair of zinc centres are bridged to one another via one of the two carboxylate groups of four different NH_2BDC units; this is considered a paddlewheel geometry. The remaining carboxylate on the NH_2BDC moiety coordinates to another pair of zinc cations making a neutral 2D sheet of $Zn_2(BDC)_2$; this is considered a paddlewheel sheet. At this stage, each zinc is square planar with, at most, a single remaining site available for coordination. The DABCO unit acts as a pillar connecting two sheets to one another via the final coordination site of the zinc centre. Each zinc is a five-coordinate square-based pyramid, hence the pillared paddlewheel nomenclature.

As stated above, the synthesis of $Zn_2(NH_2BDC)_2DABCO$ is challenging, with the synthesis of a perfectly crystalline material difficult to reproduce. During the synthesis of this MOF, an impurity of 1D chains of $Zn(H_2O)_2(NH_2BDC)$ were formed.[146] The formation of this impurity, and potentially others, precluded the formation of a reproducible, high surface area crystalline material. The work attempted to synthesise $Zn_2(NH_2BDC)_2DABCO$ by changing a variety of variables such as temperature, ratio of starting materials, reaction time, and reaction vessel size. No common thread was observed that would result in a reproducible synthesis for the material. At the time, one area of research that we had not explored was the role solvent played on the synthesis of the MOF.

The most common solvent in the synthesis of MOFs is DMF. DMF is selected because most MOF node/linker precursors exhibit a high degree of solubility in DMF.[24, 147] Secondly, DMF has a high boiling point (153 °C). This enables researchers to tune the kinetics of the reactions. Perhaps most importantly, as illustrated in Figure 3.3, DMF can also undergo favourable acid-base chemistry during MOF formation.[147] In the simplest equation, the reaction of an acid linker and a metal salt produces a MOF and acid. With regards to metal-ligand bonds, Brønsted acids can break metal-ligand bonds. As such, the formation of acid can be detrimental to the formation of MOFs. Acids such as HCL, the byproduct of the formation of a MOF between a metal chloride and a dicarboxylic acid, can readily break the newly formed metal-ligand bonds. To avoid this from happening, DMF is utilized as the solvent of choice in MOF synthesis. As DMF is heated in the synthesis, it decomposes to formic acid and dimethylamine; the formic acid continues to decompose to CO and water.[148] The dimethylamine base can react with any acid to form the dimethylammonium cation. Thus, it is critical in choosing the appropriate solvent when making MOFs. In fact, some MOF synthesis utilizes the addition of a small amount of acid to modulate this chemistry to assist in the formation of large crystals vs. polycrystalline, or potentially, amorphous powders.

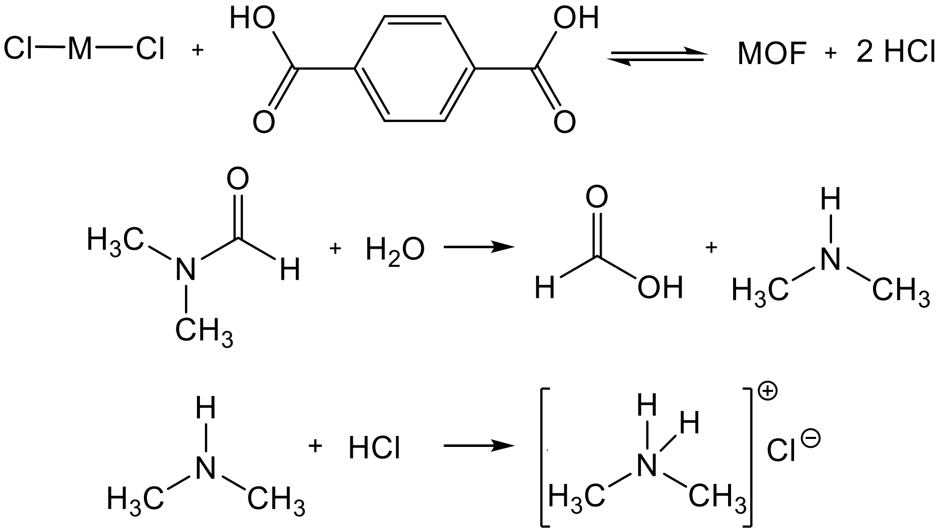

Figure 3.3. Example of DMF acid-base chemistry in the synthesis of MOFs.

Although DMF is attractive in the synthesis of MOFs, DMF is readily absorbed into the skin, causing adverse liver effects and reproductive toxicity.[149, 150] With that in mind, researchers have been focused on synthetic methodologies that reduce or eliminate the use of DMF. Alternative solvents, such as water, and dihydrolevoglucosenone (Cyrene), have been used in the solution-based synthesis of MOFs.[24] Furthermore, solvent free methods such as ball milling, where little-to-no solvent is used in the procedure, have been shown to be successful.[151]

With my interest in $Zn_2(NH_2BDC)_2DABCO$, I turned my attention to using dimethyl sulfoxide (DMSO) as a replacement solvent for DMF. The Hansen solubility parameters relating to dispersion (δ_D), polarity (δ_P) and hydrogen bonding (δ_H) interactions, indicate that DMSO is a close solvent match to DMF, as compared to water or ethanol (Table 3.2).[152] The Hansen solubility parameters help in relating chemicals to one another based on their intermolecular interactions and dissolving power.[152] Although DMF and DMSO have similar Hansen parameters, their toxicity is quite different. DMF is readily absorbed into the skin and can cause quite adverse side effects. On the other hand, if DMSO is absorbed into the skin, such side effects do not occur.[153] In fact, homeopaths utilize DMSO topically to treat joint pains[154]; while this doesn't prove its efficacy for this application, it does demonstrate the relative safety of the two solvents. Although, it may be noted that DMSO does present a risk in terms of having the potential to carry other materials through the skin. While this risk is noted, DMSO on its own, carefully obtained, does not present this inherit risk.

Table 3.2. Physical Properties of DMF and DMSO Compared to Other Common Solvents.[152]

	DMF	DMSO	Water	Ethanol
δ_D/MPa$^{0.5}$	17.4	18.4	15.5	16.6
δ_P/MPa$^{0.5}$	13.7	16.4	13.2	8.8
δ_H/MPa$^{0.5}$	11.3	10.2	42.3	19.4
MP/°C	-60.5	19	0	-114
BP/°C	153	189	100	78
ρ/g cm^{-3}	0.94	1.1	1.0	0.789
V_m/cm^3 mol^{-1}	77.0	71.3	18	168

DMSO has the solvating power necessary for MOF formation but lacks the favorable acid-base chemistry provided by DMF. With that in mind, I explored the use of DMSO in synthesizing $Zn_2(NH_2BDC)_2DABCO$ using a stoichiometric amount of DMF to aid in the favourable acid-base chemistry. Using the temperature and reagent concentrations used to attempt to make $Zn_2(NH_2BDC)_2DABCO$, I explored the role of DMSO in forming this MOF. Unlike the work in DMF, to my surprise, large X-ray quality single crystals were found in the reaction vessel the following day (ca. 24h later). The crystals did not have the morphology expected for $Zn_2(NH_2BDC)_2DABCO$ (cube-shaped crystals). Instead of forming $Zn_2(NH_2BDC)_2DABCO$, another MOF with different connectivity was formed; the chemical formula of this MOF was $Zn_3(NH_2BDC)_3DABCO$ and was observed as large yellow crystals (*vide infra*).

Although the initial synthesis yielded X-ray quality crystals of $Zn_3(NH_2BDC)_3DABCO$, the initial procedure was not reproducible. At times, no crystals would form, and at other times, crystals would form with an additional material that appeared as yellow flakes. There was a clear variable that I was not controlling between different batches.

To gain better insight into the synthesis, a combination of optical microscopy, to examine the presence or absence of the yellow flakes, as well as the solution-phase ^1H NMR spectroscopy of the dissolved solid material was used as a bulk measurement for quantitative results; MOFs are often dissolved in a combination of a few drops of strong acid to break the metal-linker bonds, and DMSO-d_6 as a highly solubilizing lock solvent. To better explore the NMR, we must first examine the protons in the free linkers. The linkers used in the synthesis of $Zn_3(NH_2BDC)_3DABCO$ are shown schematically in Figure 3.4. The ligands containing protons are 2-aminoterephthalic acid (H_2-NH_2BDC) and DABCO.

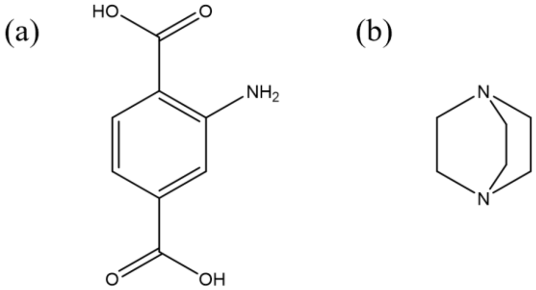

Figure 3.4. Chemical structures of H_2-NH_2BDC (a) and DABCO (b).

Given the MOF has two different linkers at a ratio of 3:1 NH_2BDC:DABCO, solution phase NMR can help compare the linker ratio to identify the bulk ratio of linkers vs. the ratio found in the crystal structure (Figure 3.5). Although the linker ratio is 3:1, we expect a 9:12 integration ratio for the C-H protons on the DABCO and the C-H protons on the NH_2BDC.

When impurities were observed in the synthesis of $Zn_3(NH_2BDC)_3DABCO$, ratios less than 9.00:12.00 of NH_2BDC:DABCO were measured. For example, select NH_2BDC:DABCO ratios of 9.00:3.30, 9.00:6.40, and 9.00:9.00 were all observed throughout the optimization process.

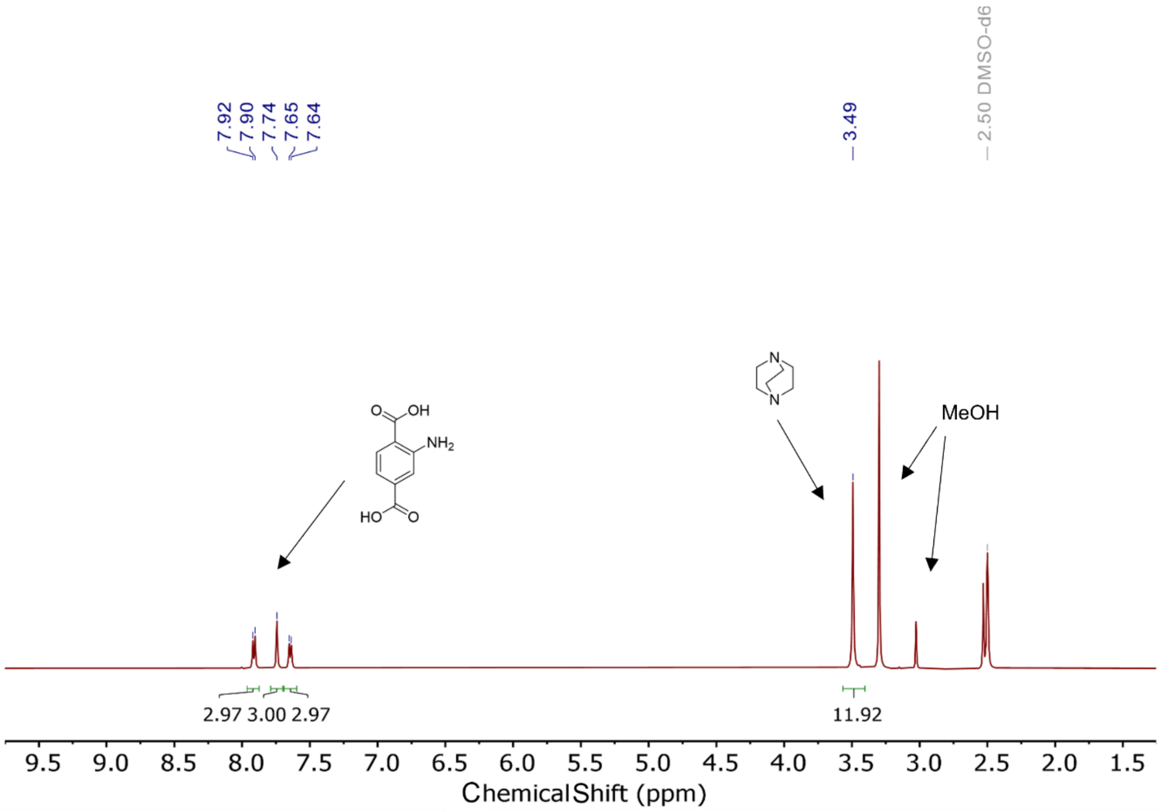

Figure 3.5. ^1H NMR of acid-digested of $Zn_3(NH_2BDC)_3DABCO$ showing integration value with an overall 3:1 ratio of NH_2BDC:DABCO (500 MHz, DMSO-d_6).

Given these less-than-ideal ratios, we can rationalize two different possibilities: too little DABCO or too much NH_2BDC is present. The former would suggest that some DABCO linkers are missing from the structure (defects). If this is the case, then it is important to determine the optimal synthesis that would result in a constant number of linker defects. The secondary possibility in rationalizing poor ligand ratios is the dissolved solid may be rich in NH_2BDC. This option suggests that an impurity (or impurities) is present that contain a higher amount of NH_2BDC in comparison with the structure of $Zn_3(NH_2BDC)_3(DABCO)$. Given the challenges the group has had with the synthesis of $Zn_2(NH_2BDC)_2DABCO$, the observations of 1D chains of $Zn(H_2O)_2(NH_2BDC)$, and the presence of yellow flakes in the synthesis of $Zn_3(NH_2BDC)_3DABCO$, I believe that the latter hypothesis is more likely.

Table 3.3. The Role of Water on the Optimized Synthesis of $Zn_3(NH_2BDC)_3DABCO$.

Amount of water added (μL)	Formation of crystals	Mixture appearance
0	No	N/A
100	No	N/A
200	No	N/A
300	Yes	Cloudy
400	Yes	Cloudy
500	Yes	Clear
700	Yes	Cloudy
900	Yes	Cloudy

At an attempt to improve the reproducibility of $Zn_3(NH_2BDC)_3DABCO$, the first variable investigated in the reaction was the purity of the solvent. For air/moisture stable chemistry, and with MOF chemistry, we often take for granted the purity of solvents, assuming that one reagent bottle is the same as another. However, depending on the solvent and the age of the bottle, the purity of a solvent alters with time. DMSO is a hygroscopic solvent. With that in mind, we hypothesized that either the DMSO solvent bottle used for the procedure that produced the original crystals contained some amount of water and water was needed for the synthesis, or the original solvent bottle was relatively dry, and water was adversely affecting the synthesis in subsequent reactions. To test this hypothesis, a new and unopened bottle of DMSO, and a new bottle of DMF was used to test out the role of water on the product formation. A large solution of the MOF components was made using this bottle of DMSO and split into smaller reaction vials (4 mL). In each vial, a different amount of water was added. With 3 mL of DMSO and 0.2 mL of DMF, the amount of water was varied from 0 – 900 μL (Table 3.2). The vials were placed in the oven at 120 °C. The vials were monitored for the formation of crystals and the clarity of the mixture after two days.

Based on the results in Table 3.3, a minimum of 300 μL of water is needed per 3 mL of DMSO to produce crystals. Interestingly, there seems to be an optimal amount of water around 500 μL where the mixture does not appear cloudy. At greater water content, the mixture became cloudy again. The concern with the cloudy mixture is that the material that is left in suspension may not reflect the connectivity or formula of the crystals and thus could lead to incorrect interpretation of bulk materials properties (e.g., gas adsorption). The procedure containing 500 μL of water was repeated several times. After repeated experiments, the mixture was always transparent at this water content indicating that the optimized water content in the synthesis of $Zn_3(NH_2BDC)_3DABCO$ was 500 μL. These results are indicative that some amount of water is critical in the synthesis of this material and that the original attempt at making $Zn_3(NH_2BDC)_3DABCO$ was carried out using an older DMSO solvent bottle that had adsorbed too much water. To see if the MOF synthesis can be scaled to produce more crystals per batch, the reaction was scaled by a factor of 3

(1500 μL of water per 9 mL of DMSO). The products and reaction observations for this reaction were consistent with what was observed on the smaller scale. Although I was able to optimize the water content, it is worth mentioning that the water content may need to be adjusted due to the water content in the DMSO. As a general guideline, the minimum water concentration was approximately 500 μL in 3 mL of DMSO. These amounts were mostly adjusted in the summer months when the environment was more humid.

To further optimize the synthesis of this MOF, the reaction temperature was explored. Reaction temperature is a critical factor in MOF synthesis. The temperature of the reaction is used to provide energy that goes into breaking and forming new bonds, so that a crystalline and ordered structure can form. At an ideal temperature, we can optimize the crystal growth rates in a manner that leads to the formation of the desired product. The advantage of using high-boiling solvents (e.g., DMF and DMSO) is that the kinetics of crystal growth can be modulated over a wide temperature range. $Zn_3(NH_2BDC)_3DABCO$ was synthesized using the optimal solvent and metal ligand ratios used above (1.68 mM $Zn(NO_3)_2 \cdot 6H_2O$, 1.52 mM H_2-NH_2BDC, and 0.844 mM DABCO) and placed in ovens at 90 °C, 100 °C, 110 °C, and 120 °C. The formation of crystals was observed at five day, four days, three days, and two days for 90 °C, 100 °C, 110 °C, and 120 °C, respectively. All of the temperatures listed yielded crystalline products, but at higher temperatures, the presence of yellow flakes were more prominent. If the reactions were left too long in the oven, the presence of flakes tended to increase as well. Thus, the optimal temperature was determined to be 110 °C due to the lack of yellow flakes present while minimizing the reaction time used. It is noteworthy to mention that no crystals seem to form for an extended amount of time and then suddenly large crystal appear over a very short time period. For example, when crystals were formed at 110 °C, nothing was observed in the vials after 46 hours, but between 46 hours and 48 hours, surprisingly large X-ray quality single crystals were observed.

3.2.2 Crystal Structure of $Zn_3(NH_2BDC)_3DABCO$

The crystal structure of $Zn_3(NH_2BDC)_3DABCO$ contains a node consisting of three inline zinc centres along the c-axis (Figure 3.6). Each zinc centre is bridged to a neighbouring zinc centre via syn-syn bidentate bridging mode of three carboxylate linkers from the NH_2BDC linker ($(Zn_{1.5}RCOO)_3$). The zinc centers are not all chemically equivalent. The outer two zinc centres are tetrahedral and chemically equivalent. The central zinc centre is octahedral with one face of the octahedron coordinating via the syn-syn coordination with a tetrahedral zinc and the opposite face of the octahedron coordinating via the syn-syn coordination with the second tetrahedral centre; hence the $Zn_{1.5}(RCOO)_3$ nomenclature indicating one whole zinc (tetrahedral) and one face of a zinc centre (octahedral). As such, the two tetrahedral zinc centres form a symmetric fac isomer with the central octahedral zinc centre. Overall, the node forms two 3-fold symmetric paddlewheels in the ab-plane that are perfectly staggered (60°) with respect to one another. With three NH_2BDC linkers per tetrahedral zinc, the remaining axial position of the tetrahedron is coordinated by a DABCO unit. The colour coding in Figure 3.6 is intended to aid in visualizing the structure in sheet structures and how they pack in Figures 3.7 and 3.8.

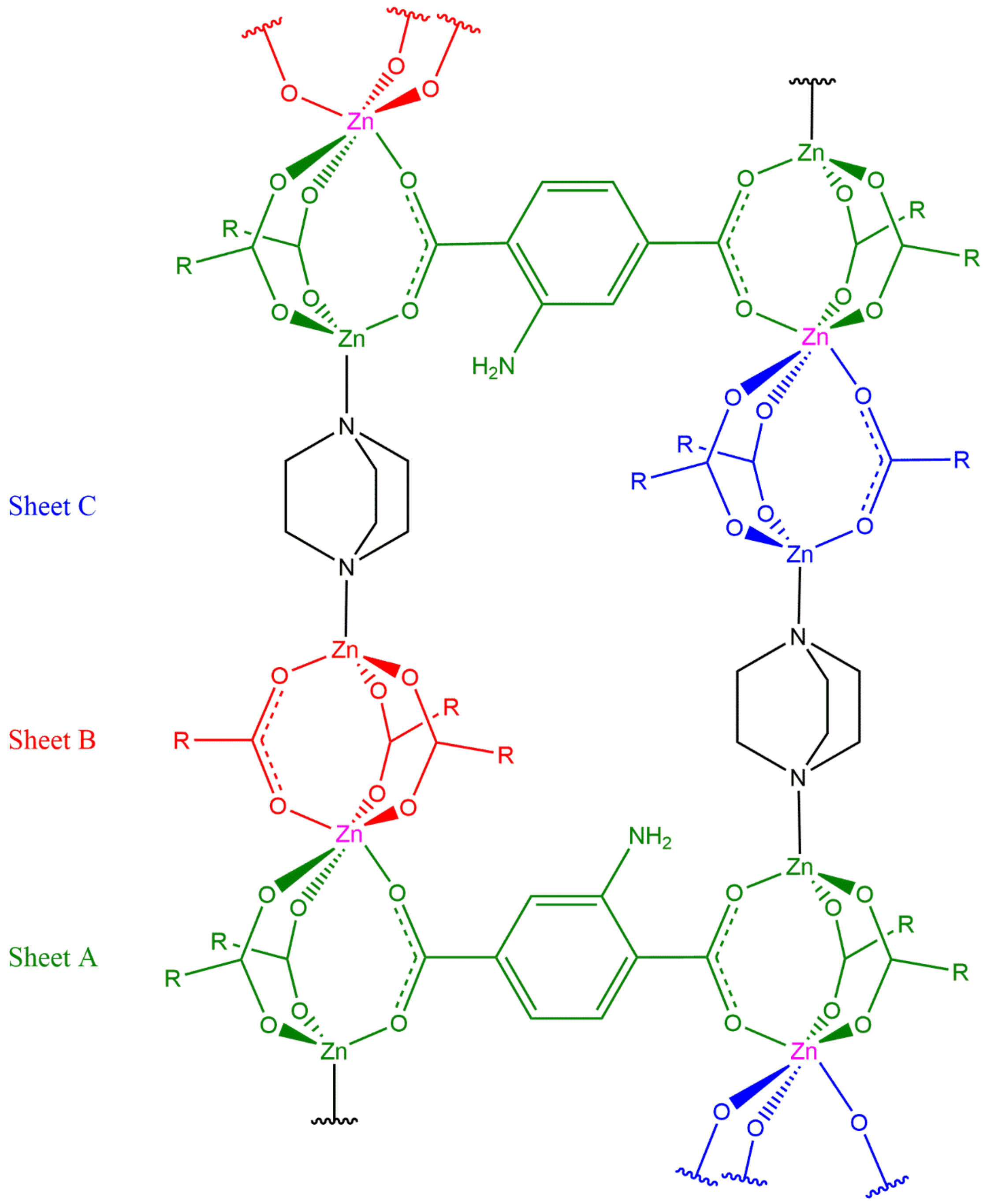

Figure 3.6. Crystal structure of $Zn_3(NH_2BDC)_3DABCO$ illustrating the connectivity between nodes and linkers.

Focusing only on one zinc paddlewheel (Zn_{tet}-Zn_{oct} pair; green-pink in color in Figure 3.6), the paddlewheel dimer connects to three neighbouring paddlewheel dimers via the other end of the bridging NH_2BDC carboxylates. Expanding this connectivity in this direction (ab-plane) results in a hexagonal paddlewheel sheet (Figure 3.7). Of note is the relationship of the nodes to one another within the sheet. As shown in Figure 3.6 and Figure 3.7, if one node is considered to point up (i.e., the DABCO attached to the tetrahedral zinc is above the sheet), then the neighbouring nodes point down (i.e., the DABCO attached to the tetrahedral zinc is below the sheet). For the purpose of the structural description, we will call the described sheet as Sheet A (Figure 3.7).

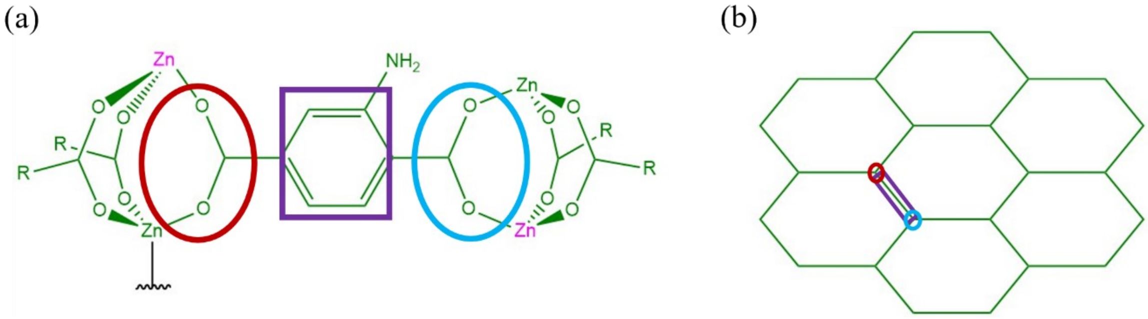

Figure 3.7. Simplified structure illustrating how the vertices in the hexagonal honeycomb layer represent half of a Zn_3 node and how the vertices are connected via NH_2BDC linkers (a) and the overall connectivity between the nodes and linkers in one individual sheet (b).

Each node consists of two fused – with the central octahedral zinc acting as the fuse point – paddlewheel sheets. The second sheet (Sheet B; Figure 3.8) also forms a hexagonal sheet, but due to the staggered relationship of the two paddlewheels on one node (e.g., red circle Figure 3.7), the neighbouring nodes are a different set of nodes (i.e., the neighbouring node from Sheet B is not the blue circle in Figure 3.7).

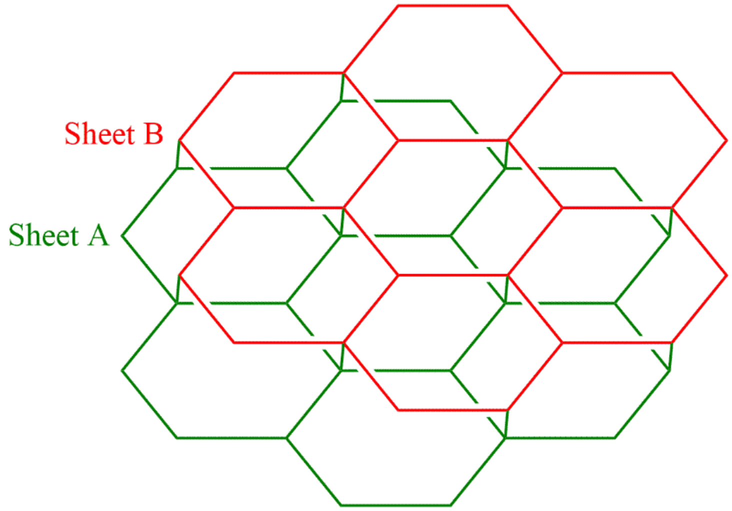

Figure 3.8. Illustration of how Sheets A and B stack with respect to one another.

Focusing on the original Zn_3 node used to build this discussion, Sheet B connects to a new Sheet A via the DABCO unit above (Figure 3.6), while Sheet A connects to a new Sheet B via a DABCO unit below; this DABCO acts like a pillar between nodes; this creates a stacking of AB-DABCO-AB-DABCO-AB along the c-axis.

There is an additional sheet (Sheet C) that exists. As shown in Figures 3.6 and 3.9, an additional sheet (Sheet C) can be viewed growing from the neighbouring node relative to the node used for our discussions above. The neighbouring paddlewheel wraps around the DABCO unit of the AB-DABCO-AB chain (Figure 3.9 and 3.6). Thus, this second node produces a CA-DABCO-CA-DABCO chain along the c-axis; similarly, a BC-DABCO-BC-DABCO chain is also possible.

A simplified version of how sheets A, B, and C stack on top of one another is shown in Figure 3.9. As illustrated, all the sheets are relative to one another. The DABCO linker forms a connection between sheet A and sheet C as shown by the bold black lines. Sheets A, B, and C collectively make up the whole 3-D repeating structure of the MOF. As the MOF continues to grow, all three sheets repeat in the same order, respectively. Interestingly, if the DABCO was not present, then the connectivity of the sheets would not change. Thus, as a pillar, the DABCO is not acting as a structural support group. As the data in the crystal structure suggests, the pore aperture of $Zn_3(NH_2BDC)_3$DABCO seems to be quite small in comparison to other MOFs. By observing the structure of the MOF, we can see that the dimensions for the pore aperture may be around those required for molecular sieving.

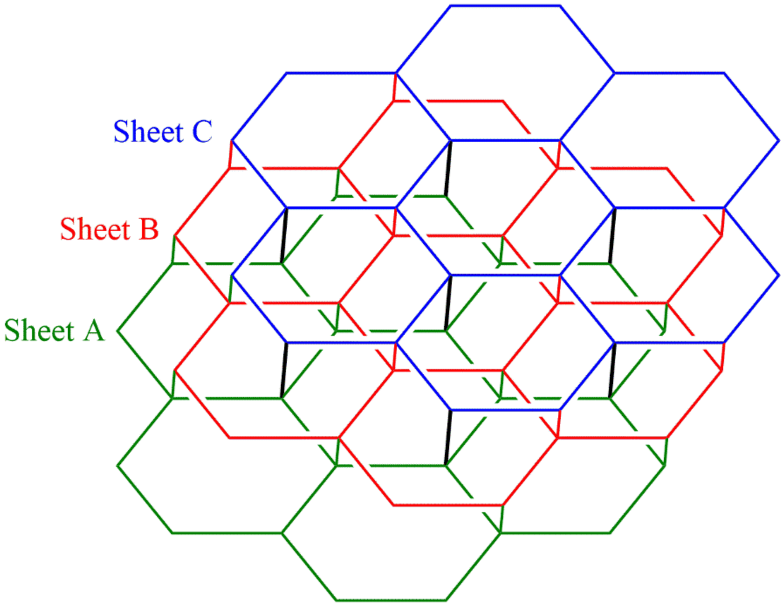

Figure 3.9. 3-D representation of how sheets A, B, and C stack with respect to one another. The grey circle represents the node used to generate a CA-DABCO-CA-DABCO chain along the c-axis.

While we were able to synthesize $Zn_3(NH_2BDC)_3DABCO$ and understand the crystal structure in depth, we turned our attention to attempting to alter the structure by replacing the metal centres or switching the ligands. A variety of transition metals were tested using the same H_2-NH_2BDC ligand, but the only other transition metal that formed a crystalline structure was cadmium. In the X-ray crystal structure of this material, we found the chemical formula was $Zn_2Cd(NH_2BDC)_3DABCO$; to our surprise, the only metal that was replaced was the central zinc that occupied an octahedral site. The two other zinc metals, both occupying tetrahedral geometries, remained unsubstituted (see Appendix A, Table A.1 for the crystallographic data for both $Zn_3(NH_2BDC)_3DABCO$ and $Zn_2Cd(NH_2BDC)_3DABCO$).

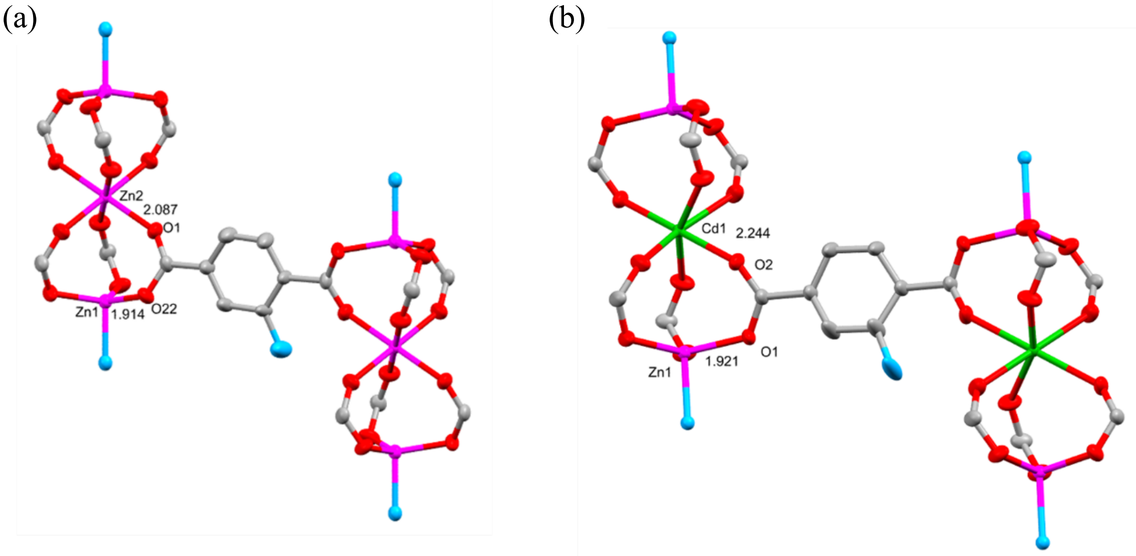

Figure 3.10. Illustration of $Zn_3(NH_2BDC)_3DABCO$ (a) and $Zn_2Cd(NH_2BDC)_3DABCO$ (b) showing the differences in bond lengths in Å [Cd, green; Zn, pink; N, blue; C, grey; O, red].

As observed in Figure 3.10, the bond lengths are different when the central zinc is replaced with a cadmium atom. In $Zn_3(NH_2BDC)_3DABCO$, the Z–O bond length is 2.086(2) Å for the central zinc atom. For $Zn_2Cd(NH_2BDC)_3DABCO$, the Cd–O bond length is 2.244(15) Å. This difference in bond length shows that the orientation of each node is slightly different. The bond lengths on the Cd-O vs. the Zn-O are longer; thus, the ab-plane is slightly wider, which has a direct impact on the pore size and aperture. If the ab-plane is slightly wider in $Zn_2Cd(NH_2BDC)_3DABCO$, the pore size and aperture of this structure are bigger than the pore size and apertures observed in $Zn_3(NH_2BDC)_3DABCO$. This small difference in pore size may become an interesting property when exploring the molecular sieving properties for each structure. The slight increase in bond length for $Zn_2Cd(NH_2BDC)_3DABCO$ may allow the material to let more gases or larger gases into the structure compared to $Zn_3(NH_2BDC)_3DABCO$.

3.2.3 Activation Methods

3.2.3.1 Thermal Activation

With the synthesis of $Zn_3(NH_2BDC)_3DABCO$ determined, and our interest in examining the gas adsorption properties of these microporous MOFs, I turned my attention to activation of the material. Activation of materials prior to gas analysis is extremely important, as it is the process of eliminating solvent molecules from the pores of the MOF structure. The pores of the MOF must be empty to accurately measure the quantity of gas molecules entering or exiting the material. Activation can be achieved though several processes including heating, solvent-exchange, and supercritical CO_2 drying. The initial activation method explored for this material was thermal activation. Thermal activation of the material can be quite challenging because of the high boiling point associated with DMSO. High temperatures (i.e., 189 °C and above) are necessary to eliminate the DMSO molecules from the overall structure. If the activation temperature is too high, it is possible that the metal-ligand bonds of $Zn_3(NH_2BDC)_3DABCO$, or other bonds, may be destroyed. As the DMSO molecules are being heated and removed from the pores of the material, they may lead to decomposition of the overall framework of the material. It is critical to select a temperature in which DMSO is being eliminated while the structure of the MOF remains intact. To experimentally determine the proper activation temperature, thermal gravimetric analysis (TGA) was used.

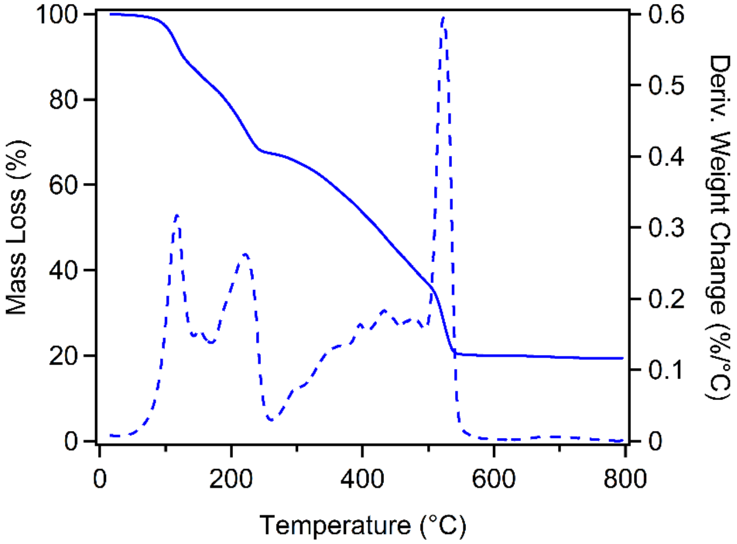

Figure 3.11. TGA of $Zn_3(NH_2BDC)_3DABCO$ soaked in DMSO at a heating ramp rate of 10 °C/min; mass loss (solid line) and derivative weight change (dashed line).

TGA analysis is a process in which the weight of a material is measured as a function of temperature. After soaking the MOF in DMSO for a day to ensure the only solvent molecule present in the MOF is that of DMSO and not of any of the other solvents used in the synthesis. Crystals of $Zn_3(NH_2BDC)_3DABCO$ were filtered from DMSO and allowed to dry on filter paper to remove any excess solvent (i.e., any solvent that is not in the pore). For the purposes of this thesis, a ramp rate of 10 °C/min was used in Figure 3.10 to illustrate a typical TGA curve for this material. The derivative weight change is shown on the right-axis where each peak demonstrates a loss of material.

Analysis of thermograms can yield information about the ratio of materials that can be burned (often organics) to those that leave residual material (often inorganics). This information can be used to approximate a chemical formula. Additionally, for MOFs, thermograms can be used to explore the loss of pore-bound solvent and the strength of any pore-solvent interaction. For example, loss of pore-bound water that is not coordinated should occur around 100 °C, with the % loss reflecting the number of water molecules lost per mass. For other solvents that are coordinated, the mass loss may occur above the boiling point of the solvent, since additional energy needs to be given to break the bonds. While thermograms can often have overlapping mass losses, the derivative of the weight change can be used to more easily ascertain the temperature range associated with the mass loss.

For $Zn_3(NH_2BDC)_3DABCO$ we expect to see solvent losses around the molecular weight of the solvents in the pore around their boiling points (i.e., 100 °C for water and 189 °C for DMSO). Ideally, after all the solvent is removed from the material, the weight of the material should remain constant until the material begins to decompose. In Figure 3.11, the derivative weight change of the material shows several mass losses occurring prior to 190 °C followed by a small region in which no mass loss occurs until decomposition of the material begins (ca. 250 °C). As the material had been soaked in DMSO, we expect a certain amount of DMSO to remain inside the pores of the MOF. It can be observed, via calculations shown in Table 3.4, that the MOF contains six DMSO molecules prior to activation of the material. For six DMSO molecules to be present in the material, a solvent mass loss of 68.4% should be observed prior to decomposition of the MOF. As seen in Figure 3.11, the solvent loss peaks (peaks occurring before 200 °C) correspond to a mass loss around 68%.

Table 3.4. Calculated Mass % of MOF as a Function of DMSO Molecules Present in the Structure.

Formula	Molecules of DMSO lost	% of Mass
$Zn_3(NH_2BDC)_3DABCO(DMSO)$	1	94.1
$Zn_3(NH_2BDC)_3DABCO(DMSO)_2$	2	88.1
$Zn_3(NH_2BDC)_3DABCO(DMSO)_3$	3	82.2
$Zn_3(NH_2BDC)_3DABCO(DMSO)_4$	4	76.2
$Zn_3(NH_2BDC)_3DABCO(DMSO)_5$	5	70.3
$Zn_3(NH_2BDC)_3DABCO(DMSO)_6$	6	68.4
$Zn_3(NH_2BDC)_3$	N/A	59.3
$(ZnO)_3$	N/A	19.7

It can also be observed in Table 3.4, the decomposition of the MOF (when the ligands holding the structure begin to break apart), mass losses around 59.3% should be seen. After the material is completely decomposed, we are left with a total mass around 20% which correlates to a remaining zinc oxide (ZnO) molecule. While a definitive activation temperature was not observed, we wanted to correlate the X-ray diffractograms with the activation temperature to see if an optimal activation temperature could be determined.

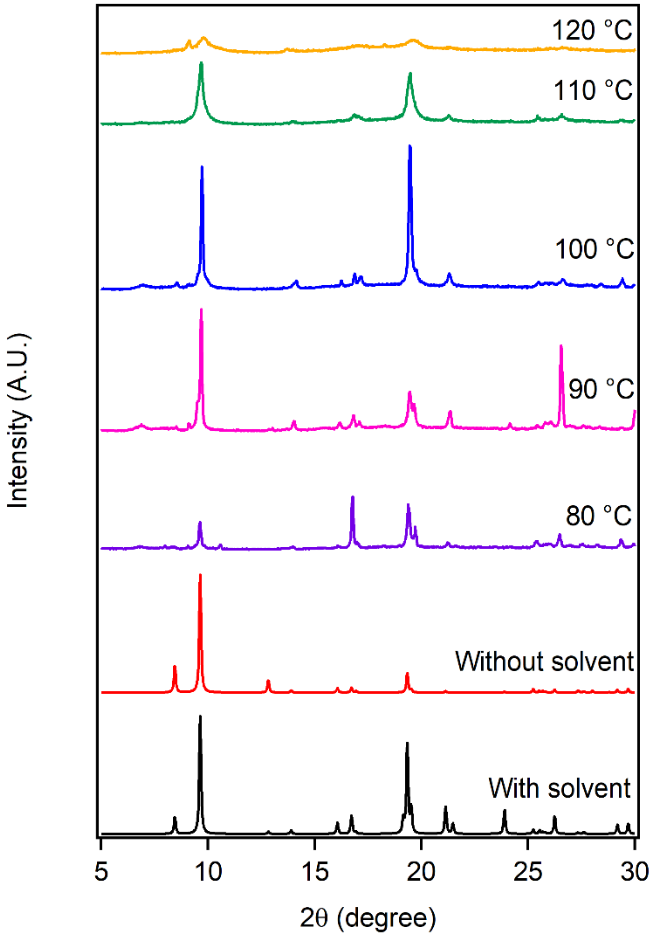

Figure 3.12. PXRD of $Zn_3(NH_2BDC)_3DABCO$ at different activation temperatures compared with the PXRD of the MOF with DMSO in the pores and without it.

Once $Zn_3(NH_2BDC)_3DABCO$ was synthesized, samples were heated under vacuum at different temperatures using a Micromeritics SmartVac prep. Each of the samples were evacuated to 5 mmHg prior to heating and subsequently heated at 80, 90, 100, 100, 110, or 120 °C. We wanted to avoid 190 °C because that is a relatively high temperature where the

MOF is known to start decomposing. As seen in Figure 3.11, the TGA shows the beginning of solvent loss around 100 °C. Therefore, the activation temperatures were selected loosely based upon the TGA results making sure to include a range of temperatures around that result. In an ideal case, there would be a long plateau region between solvent loss and MOF decomposition, but this was not the case when using DMSO as the solvent. After activation under a vacuum, the samples were analyzed by powder X-ray diffraction (PXRD) and compared to the simulated versions with DMSO solvent and without DMSO in the pores (Figure 3.12).

In comparing the simulated spectrum of $Zn_3(NH_2BDC)_3DABCO$ without solvent, to the observed spectra of the heated sample, we see a few key observations. The peak positions for some of the more-prominent reflections between the simulated without solvent and observed PXRDs match. Of particular note, as the temperature is changed, the peak positions do not change suggesting that large structural changes are not occurring. The peak width, which is an indication of small particles and/or amorphous behaviour, does not seem to increase until temperatures greater than 110 °C suggesting that structural damage does not occur until these temperatures. The peak intensities are more challenging to interpret. The changes are indication of a change in atomic positions and electron density either due to a change in position of atoms in the framework or the pore or the removal of solvent from the pore. These changes are not captured in the simulated structures since the simulated structures are simulated with six DMSO molecules per formula unit and no DMSO molecules per formula unit (i.e., the framework alone). This doesn't factor in changes in the flexibility of the framework as the solvent is removed or the affects of only partial solvent removal. Given this data, as an upper limit of thermal stability, the MOF should not be heated above 100 °C. Looking at the TGA data, this presents a problem because solvent loss still occurs at temperatures higher than 100 °C. This suggests that a low and slow heating method may be the best option to remove as many solvent molecules as possible. If heated at a lower temperature than the TGA suggests, a longer heating time is needed to ensure all the solvent molecules are removed from the pores of the MOF without damage to the crystalline structure/framework.

3.2.3.2 Solvent-assisted Activation

If the solvent inside the pores of the MOF can be replaced with an alternative solvent, without damaging the connectivity within the crystals, activation of the material has the potential to be easier than just thermal activation from DMSO-filled pores. In certain cases, when solvent boiling points are high, they can be swapped out with lower boiling point solvents. Low boiling point solvents require significantly less heat to be eliminated from the pores. If activation of the material is at a much lower temperature, solvents can be removed from the pores without damaging the material. $Zn_3(NH_2BDC)_3DABCO$ was rinsed three times with separate solvents to examine the effects of the pore-filled solvent. The solvents used were acetone, isopropanol, and methanol as they all have significantly lower boiling points than DMSO. Each day, the solvent was decanted and replaced with fresh solvent over a period of three days; this ensures that solvents have sufficient time to diffuse through the pores and be replaced with the new solvent. After sufficient soaking time, the samples were filtered and the TGA data was collected (Figure 3.13).

As demonstrated in Figure 3.13, soaking $Zn_3(NH_2BDC)_3DABCO$ in acetone and methanol show the smoothest transition of complete solvent loss before decomposition of the MOF occurs. Between 100 – 350 °C, there is very little mass loss with increasing temperature. Also, there are no peaks observed in the derivative weight changes for acetone and methanol between that same temperature range. For isopropanol, either some isopropanol remains in the pore, or the isopropanol was unable to remove all the synthesis solvents (i.e., DMSO/DMF) as evident by the number of derivative weight changes occurring between 100 – 350 °C. From this data, exchanging the synthesis solvent with either acetone/methanol is one method to activate the material below 100 °C to eliminate the solvent from the pores of the MOF without considerable risk to the framework.

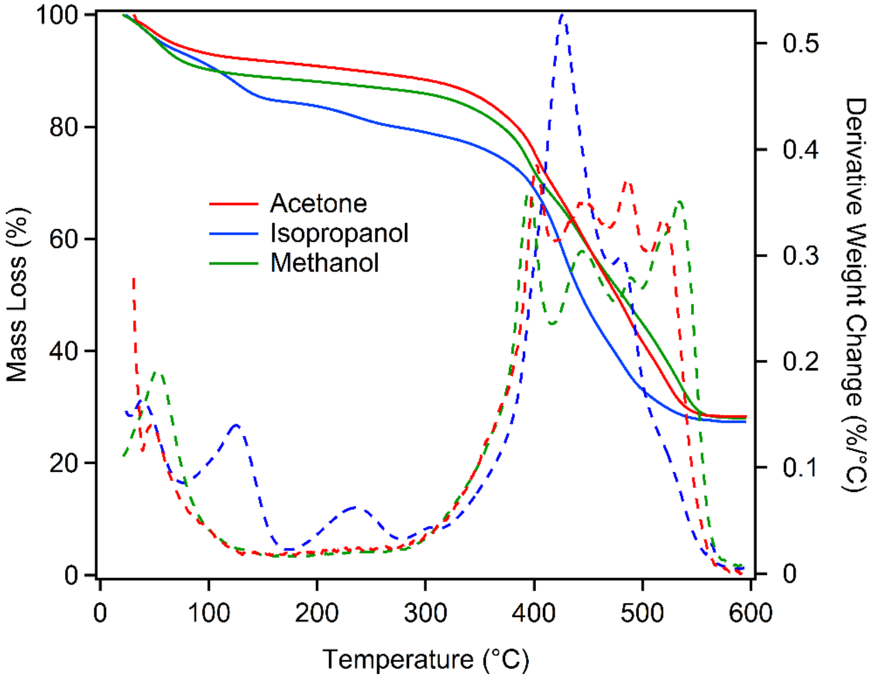

Figure 3.13. TGA of $Zn_3(NH_2BDC)_3DABCO$ when soaked in three different solvents: acetone (red), isopropanol (blue), and methanol (green).

Although TGA showed promising results, the crystals became duller in terms of their appearance. When soaked viewing the crystals under a microscope, the samples that were in acetone showed many striations while the samples soaked in isopropanol and methanol appeared to be less affected by switching out the solvents. Striations are a series of ridges and lines that decreasing the quality of the crystal from single crystal X-ray diffraction techniques (fracturing single crystals into polycrystalline powders), and sometimes even powder X-ray diffraction techniques (i.e., amorphization of the sample). To ensure the crystals were still $Zn_3(NH_2BDC)_3DABCO$ and not an impurity, single crystal X-ray analysis was conducted on the crystals. In both isopropanol and methanol, the crystals yielded the observed crystal structure of $Zn_3(NH_2BDC)_3DABCO$, albeit with a bit of framework disorder (not discussed in this thesis). Given the X-ray data and the TGA data, methanol was selected as the ideal soaking solvent in combination with the TGA results.

3.2.4 Gas Adsorption Studies

Now that a reproducible synthesis and proper activation of both $Zn_3(NH_2BDC)_3DABCO$ and $Zn_2Cd(NH_2BDC)_3DABCO$ has been achieved, the next step in this thesis is to finally explore what gases are able to adsorb to the material, whether it be by physisorption or chemisorption. The experimental method in determining gas update is via isotherms. Isotherms are a measure of gas uptake as a function of applied pressure.

3.2.4.1 Nitrogen Gas Adsorption

Nitrogen gas is a common probe molecule used to measure the gas uptake in MOFs. Nitrogen gas isotherms of $Zn_3(NH_2BDC)_3DABCO$ and $Zn_2Cd(NH_2BDC)_3DABCO$ were obtained at 77 K. These samples followed the solvent-assisted activation protocol in which they were both soaked in methanol prior to heating. $Zn_3(NH_2BDC)_3DABCO$ showed no uptake of nitrogen gas (Figure 3.14, black squares). On the other hand, $Zn_2Cd(NH_2BDC)_3DABCO$ had a nitrogen gas uptake around 1.2 mmol/g (Figure 3.14, grey circles). The value of gas uptake in the material is quite small when compared to other MOFs in the literature. As a comparison, MOF-808 has a nitrogen gas uptake of 23 mmol/g. Although the nitrogen gas uptake is quite small, we may be able to exploit the characteristic properties for $Zn_2Cd(NH_2BDC)_3DABCO$ in applications involving molecular separations.

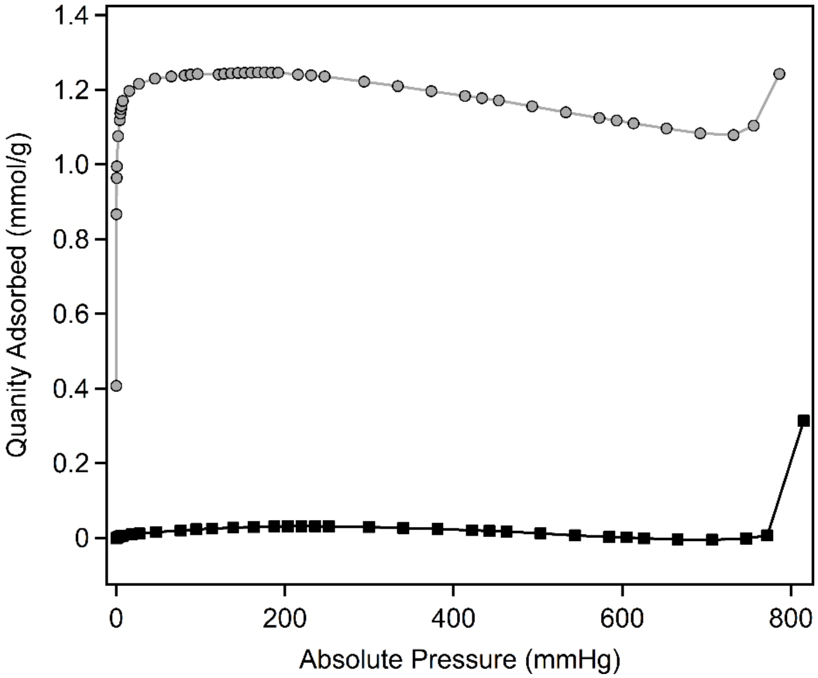

Figure 3.14. Nitrogen gas adsorption isotherms of $Zn_3(NH_2BDC)_3DABCO$ (black squares) and $Zn_2Cd(NH_2BDC)_3DABCO$ (grey circles).

These results indicate that for $Zn_3(NH_2BDC)_3DABCO$, the pore aperture must be smaller than 3.60 Å. Based on this, gas-sorption studies can be conducted with gases that have kinetic diameters smaller than nitrogen until the gas is small enough to enter the pores. Once a threshold between adsorbed gases and excluded gases is determined, the molecular sieving properties of $Zn_3(NH_2BDC)_3DABCO$ can be determined. For $Zn_2Cd(NH_2BDC)_3DABCO$, since nitrogen gas is able to enter the pores, the pore aperture of this MOF must be larger than 3.60 Å. This occurs because the pore becomes slightly wider (see section 3.2.2) upon replacement of a zinc metal centre in the octahedral position for a cadmium. The resultant change seems to open the micropore, just enough, so that nitrogen gas can enter and adsorb to the material. This is an interesting feature because such a small change in the bonding between the central atom and the surrounding oxygen atoms in the structure, results in a vast difference in nitrogen gas uptake between the two materials. This feature may be able to aid in specific molecular sieving between gases that have very similar kinetic diameters. In fact, combining the two MOFs into a separation technology could result in a tandem separation process.

3.2.4.2 Carbon Dioxide and Carbon Monoxide Isotherms

To further explore the pore aperture and the adsorption properties of these two MOFs, we measured the CO and CO_2 isotherms on both MOFs. CO has a kinetic diameter of 3.76 Å (larger than nitrogen gas and thus we don't expect it to enter $Zn_3(NH_2BDC)_3DABCO$) and CO_2 has a kinetic diameter of 3.30 Å (smaller than nitrogen gas, which will enter $Zn_2Cd(NH_2BDC)_3DABCO$ but may or may not enter $Zn_3(NH_2BDC)_3DABCO$).

CO_2 isotherms and CO isotherms of $Zn_3(NH_2BDC)_3DABCO$ and $Zn_2Cd(NH_2BDC)_3DABCO$ were collected at 283 K, 288 K, and 293 K for the solvent-assisted activated samples. In order to compare the gas sorption properties for each material, the CO_2 and CO gas uptake are shown together in one figure for each material (Figure 3.15, $Zn_3(NH_2BDC)_3DABCO$; Figure 3.16, $Zn_2Cd(NH_2BDC)_3DABCO$).

For $Zn_3(NH_2BDC)_3DABCO$, the CO_2 and CO isotherms can be seen in Figure 3.15. In this isotherm, $Zn_3(NH_2BDC)_3DABCO$ showed a maximum gas uptake of 1.48 mmol/g, 1.34 mmol/g, and 1.22 mmol/g for 283 K (Figure 3.15, yellow circles), 288 K (Figure 3.15, green squares), and 293 K (Figure 3.15, red triangles) respectively. In terms of CO gas, as expected, nearly no gas uptake was observed. The small degree of uptake may be more reflective of coverage on the external surface area rather than the internal surface area.

From the combined nitrogen, CO, and CO_2 data, we conclude that we are able to estimate the size of the pore aperture. The collective results of the gas isotherms outlined above indicate the pore aperture of the material is between 3.30 Å and 3.64 Å. Thus, $Zn_3(NH_2BDC)_3DABCO$ has potential applications in separating CO_2 from CO, CO_2 from N_2.

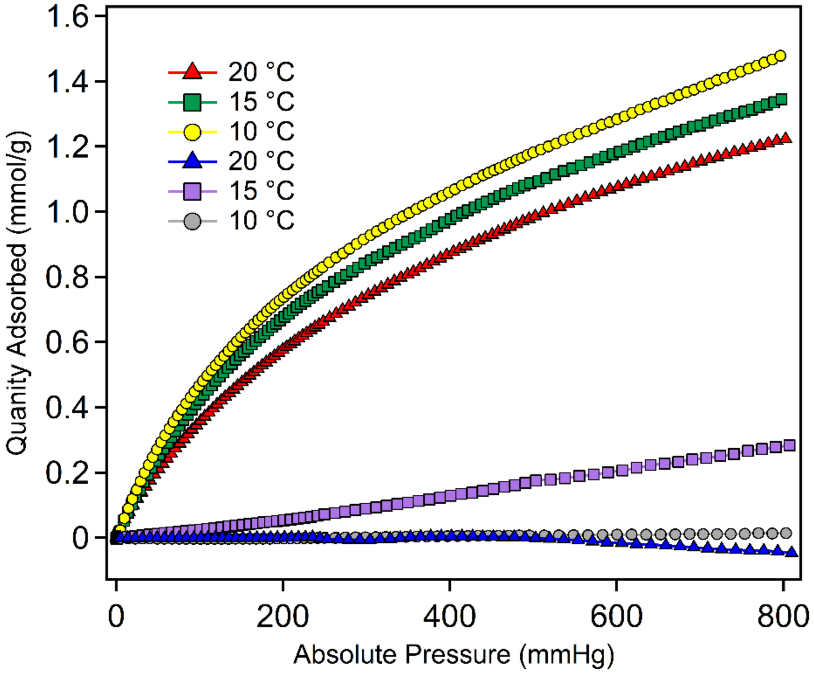

Figure 3.15. $Zn_3(NH_2BDC)_3DABCO$ CO_2 isotherms for (CO_2, 283 K, yellow circles; CO_2, 288 K, green squares; CO_2, 293 K, red triangles) and CO isotherms (CO, 283 K, grey circles; CO, 288 K, purple squares; CO, 293 K, blue triangles).

In $Zn_2Cd(NH_2BDC)_3DABCO$, the CO_2 and CO isotherms can be seen in Figure 3.16. $Zn_2Cd(NH_2BDC)_3DABCO$ showed a maximum gas uptake of 0.42 mmol/g, 0.52 mmol/g, and 0.55 mmol/g for 283 K (Figure 3.16, yellow circles), 288 K (Figure 3.16, green squares), and 293 K (Figure 3.16, red triangles) respectively. CO isotherms showed zero gas uptake for each temperature run (Figure 3.16, 288 K, purple squares; Figure 3.16, 293 K, blue triangles). The run at 283 K was omitted in Figure 3.16 because the data showed negative adsorption quantities. This is merely the error associated with the instrument and for the purposes of this project, the quantities collected at 283 K were assumed to be zero. In conclusion, for $Zn_2Cd(NH_2BDC)_3DABCO$, CO_2 is able to enter the pore, but CO may not. The challenge with CO is similar to that of the helium argument in the introduction. CO doesn't adsorb well even on large pore MOFs, so actual separation studies are necessary to determine the real separation potential.

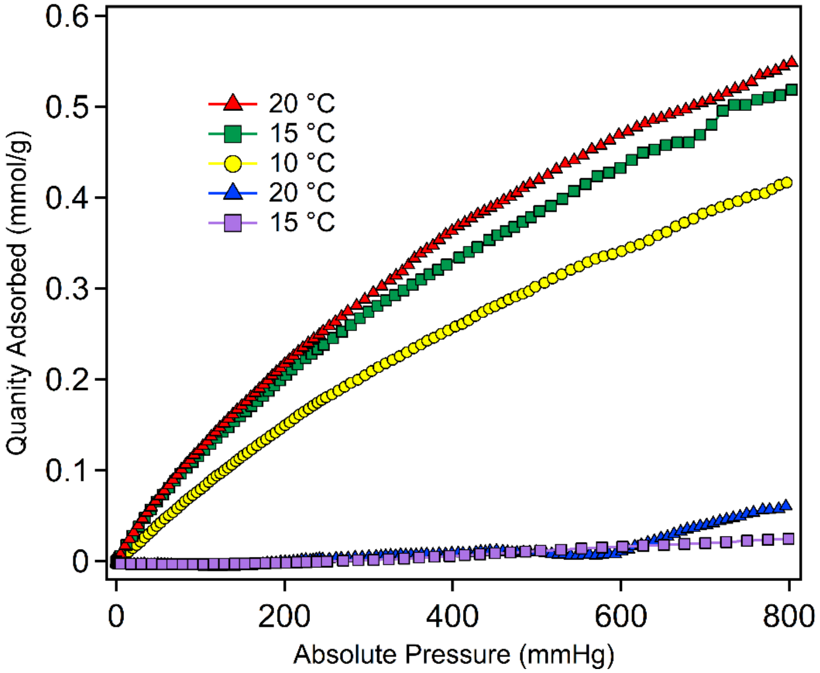

Figure 3.16. $Zn_2Cd(NH_2BDC)_3DABCO$ CO_2 isotherms for (CO_2, 283 K, yellow circles; CO_2, 288 K, green squares; CO_2, 293 K, red triangles) and CO isotherms (CO, 283 K, grey circles; CO, 288 K, purple squares; CO, 293 K, blue triangles).

From the combined data for $Zn_2Cd(NH_2BDC)_3DABCO$, we can conclude that a lower limit for the pore aperture is 3.60 Å with the potential for the pore aperture to be smaller than 3.76 Å (i.e., the kinetic diameter of CO). Further studies will be necessary with other gases to determine where the cut-off is for $Zn_2Cd(NH_2BDC)_3DABCO$.

3.2.5 $Zn_3(NH_2BDC)_3DABCO$: Attempted Derivatives

Often in the synthesis of MOFs, it is much easier to synthesize the parent MOF than the functionalized versions. The parent MOFs, in this case, are versions in which the framework contains no presence of functional groups (e.g., amine and hydroxy groups on the linker). As an example, $Zn_2(BDC)_2DABCO$ has a reproducible synthesis but the amine-functionalized version, $Zn_2(NH_2BDC)_2DABCO$, is difficult to synthesize.[146] With that in mind, we attempted to synthesize derivatives of $Zn_3(NH_2BDC)_3DABCO$ by altering the choice of linker.

Synthesis of the parent MOF, $Zn_3(BDC)_3DABCO$, was attempted. The same synthetic procedure as the functionalized version was followed and any attempts at making the parent material yielded no observation of any crystals. A ^1H NMR spectrum showed incorporation of only BDC in the solution, and no presence of DABCO was observed. The amine-functionality was switched out for bromine and hydroxy functional groups. Bromine is a much larger atom, so it may be difficult to substitute for the amine group because of the microporous nature of the MOF. The hydroxy group represents a functional group similar in size to the amine group, with similar hydrogen bonding capabilities. However, both attempts yielded no presence of crystals and again the ^1H NMR results showed no DABCO incorporation into the product. Given these results, it is necessary to have the amine group present on the linker or else any attempts at synthesizing derivatives of this material fail.

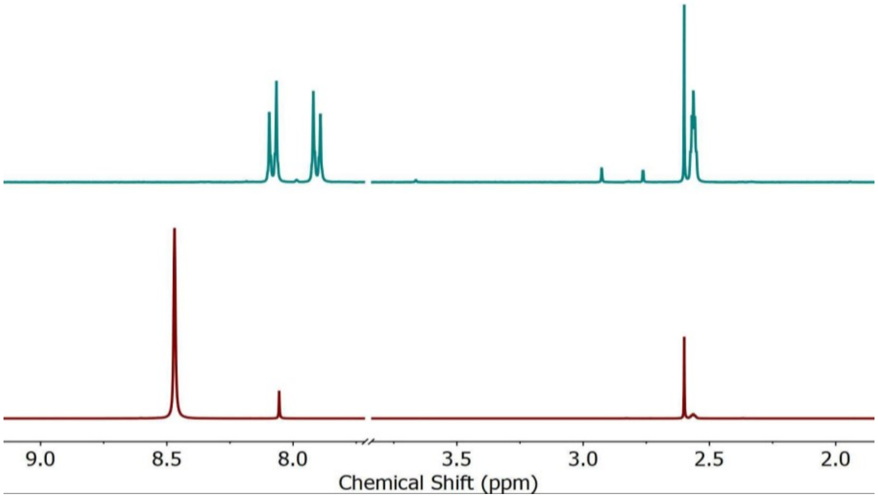

Figure 3.17. ^{1}H NMR spectrum of $Zn_3(BPDC)_3DABCO$ (blue trace) and $Zn_3(BDC)_3DABCO$ (red trace) digested in D_2SO_4/DMSO-d_6.

Instead of altering the functionality on linkers, it is possible to extend the size of the linkers too. By changing the linkers to be shorter or longer, the pore size of MOFs is altered (Figure 3.18). For instance, a terephthalic acid linker can be replaced with 1,4-benzenedicarboxylic acid (BPDC) linker. The same synthesis to make $Zn_3(NH_2BDC)_3DABCO$ was used as an attempt to make $Zn_3(BPDC)_3DABCO$ but substituting 2-aminoterephthalic acid with BPDC. A ^{1}H NMR of the solution was taken after three days and yielded no observed DABCO signal (3.50 ppm) in the spectrum (Figure 3.17). The peaks present at 2.77 ppm, 2.93 ppm, and 8.05 ppm are from residual DMF in the solution.

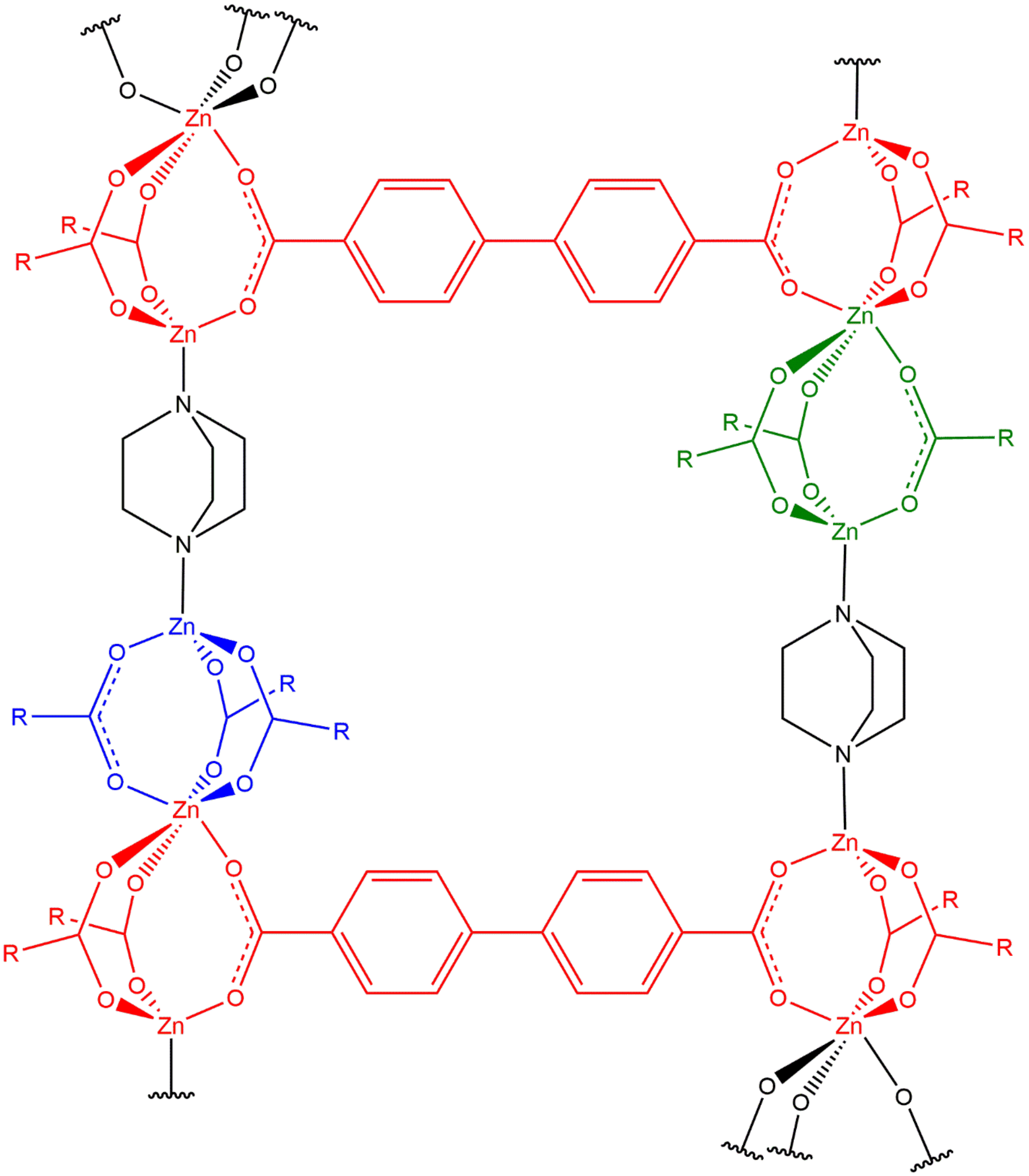

Figure 3.18. Structure of $Zn_3(BPDC)_3DABCO$ showing how extended the size of the linker increases the pore size of the MOF.

All solutions were kept in the oven at 110 °C for longer than three days to determine whether crystals required longer heating times. The solutions were kept in the oven for a further week and no appearance of crystal growth was observed. Based on these results, we were not able to expand the linker size from the parent MOF of $Zn_3(BDC)_3DABCO$. If we were able to synthesize H_2-NH_2BPDC (with the additional amine functionality on the ligand ortho to the carboxylate) and try to incorporate it into the material, it may be possible to create an even larger pore for gas adsorption to occur. This may reduce the molecular sieving abilities of the MOF but may open avenues for different adsorption experiments.

3.3 Conclusions

In summary, we were able to synthesize two different materials known as $Zn_3(NH_2BDC)_3DABCO$ and $Zn_2Cd(NH_2BDC)_3DABCO$. Detailed crystal structures of both materials were obtained, and we observed a slight difference in the pore aperture size. For $Zn_3(NH_2BDC)_3DABCO$, the central zinc forms a Zn–O bond length of 2.086(2) Å and the Cd–O bond in the other MOF, $Zn_2Cd(NH_2BDC)_3DABCO$, is 2.244(15) Å. The results in this slight difference of bond length have a direct impact on the pore size, and subsequently, the gases that are able to adsorb to the material.

Prior to gas sorption studies, we concluded that the proper activation of these two materials were to utilize a method known as solvent-assisted activation. Since DMSO is so difficult to remove from the MOFs before they begin to decompose, we opted to switch to a solvent that had a much lower boiling point. In conclusion, we soaked both of the MOFs in methanol and followed up by heating the samples gently under vacuum to remove the methanol from the pores.

In terms of gas sorption studies, $Zn_3(NH_2BDC)_3DABCO$ was only able to adsorb CO_2 gas (both nitrogen gas and CO gas were not able to enter the pores). Therefore, it can be concluded that the pore aperture of this material is between 3.30 and 3.64 Å. A slightly different result was seen for $Zn_2Cd(NH_2BDC)_3DABCO$. This MOF was able to uptake both CO_2 and nitrogen gas. It was not able to uptake any amounts of CO gas. Therefore, it can be concluded that the pore aperture of this material is larger than 3.60 Å. Since we were able to switch the metal centre in the pore for a larger atom (cadmium), we increased the pore size, and in turn, we were able to control the gas uptake properties.

In conclusion, we were able to selectivity allow for different gases to absorb to the material, depending on which central metal atom was used. Based on these results, it may be possible to tailor these results further in applications involving molecular sieving.

3.4 Experimental

3.4.1 General Materials and Instrumentation

All compounds and solvents were used as received unless noted otherwise: 2-aminoterephthalic acid (Aldrich, 99%), 1,4-diazabicyclo[2.2.2.]octane (Aldrich, 99%), acetone (ACP, 99.5%), cadmium(II) nitrate tetrahydrate (J.T. Baker, 99%), carbon dioxide (Praxair, 99.995%), carbon monoxide gas (Praxair, 99.5%), deuterated dimethyl sulfoxide (DMSO-*d6*) (Cambridge, 99.5%), deuterated sulfuric acid (D_2SO_4/D_2O) (Aldrich, 99.5 atom % D), dimethyl sulfoxide (Fischer, 99.7%), isopropyl alcohol (VWR, 99.5%), (methanol (ACP, 99.8%), nitrogen gas (Praxair, 99.9999%), *N,N*-dimethylformamide (Fisher, 99.9%), trimesic acid (Aldrich, 95%), zinc(II) nitrate hexahydrate (Aldrich, 98%), zirconium(IV) oxychloride octahydrate (Aldrich, 99.5%).

^{1}H NMR data was collected on a 300 MHz Bruker Avance III instrument, and a 500 MHz Bruker Avance instrument equipped with an inverse probe. Prior to ^{1}H NMR data analysis, the MOF samples were prepared by adding 2 drops of D_2SO_4 to 5 mg of sample and sonicated. Following sonication, an additional 1 mL of DMSO-d_6 was added and used as the locking solvent for all the data collection.

PXRD patterns were collected using a Rigaku Ultima IV X-ray diffractometer equipped with a copper X-ray source operating at 40 kV × 44 mA (1.76 kW) and a scintillation counter detector. Single crystal X-ray diffraction data were collected on a Rigaku XtaLAB Synergy-S X-ray diffractometer equipped with a 4-circle Kappa goniometer, dual PhotonJet sources (Cu and Mo), and a HyPix-6000HE Hybrid Photon Counting (HPC) detector.

Thermogravimetric analysis (TGA) experiments were collected on a TA Instruments Q500 equipped with Thermal Advantages Software (version 5.2.6). The samples were placed in a platinum pan and heated to 600 °C under a nitrogen atmosphere and further heated to 800 °C in an atmosphere of air. Approximately 10 mg of the sample was placed on a platinum weighing pan and heated to 500 °C under a nitrogen atmosphere and switched to an air atmosphere until 600 °C.

Prior to surface area analysis, samples were activated on a Micromeritics Smart VacPrep gas adsorption sample preparation device. The samples were gently heated to 60 °C for 180 minutes, followed by a ramp up to 80 °C for 180 minutes, and finally held at 100 °C for 720 minutes under vacuum. The ramp rates for each temperature were all completed using a heating rate of 5 °C/min. The samples were cooled to room temperature and backfilled with nitrogen (N_2) gas. N_2 gas adsorption isotherm data was collected at 77K on a Micromeritics 3Flex Surface Characterization instrument. The data was analysed, utilizing the MicroActive software, to obtain the Brunner-Emmett Teller (BET) surface area. CO_2 gas adsorption data was collected at 10, 15, and 20 °C on a Micromeritics 3Flex Surface Characterization instrument. The temperatures were held at a constant temperature by using a circulating water bath. CO gas adsorption data was collected at 10, 15, and 20 °C on a Micromeritics 3Flex Surface Characterization instrument with the circulating bath attachment.

3.4.2 Synthesis of MOFs

a) $Zn_3(NH_2BDC)_3DABCO$: 0.0947 g (0.844 mmoles) of DABCO was added to a 25 mL Duran® glass bottle followed by 6 mL of DMSO and sonicated until dissolution. 0.5010 g (1.684 mmoles) of $Zn(NO_3)_2 \cdot 6H_2O$ and another 6 mL aliquot of DMSO was added to the solution and sonicated. Next, 0.2765 g (1.526 mmoles) of 2-aminoterephthalic acid and 6 mL of DMSO was added and sonicated to yield a clear yellow solution. 1.2 mL of DMF and 3 mL of distilled water were added to the solution and sonicated after each addition, respectively. The solution was placed in an oven at 110 °C for three days. The solution was removed from the oven and the mother liquor was decanted. The crystals were washed with three separate 10 mL aliquots of DMSO. The resulting yellow crystals were stored in 10 mL of DMSO.

b) $Zn_2Cd(NH_2BDC)_3DABCO$: 0.0947 g (0.844 mmoles) of DABCO was added to a 25 mL Duran® glass bottle followed by 6 mL of DMSO and sonicated until dissolution.

0.1734 g (0.5621 mmoles) of $Cd(NO_3)_2 \cdot 4H_2O$, 0.3340 g (0.1123 mmoles) of $Zn(NO_3)_2 \cdot 6H_2O$, and another 6 mL aliquot of DMSO was added to the solution and sonicated. Next, 0.2765 g (1.526 mmoles) of 2-aminoterephthalic acid and 6 mL of DMSO was added and sonicated to yield a clear yellow solution. 1.2 mL of DMF and 3 mL of distilled water were added to the solution and sonicated after each addition respectively. The solution was placed in an oven at 110 °C for two days. The solution was removed from the oven and the mother liquor was decanted. The crystals were washed with three separate 10 mL aliquots of DMSO. The resulting yellow crystals were stored in 10 mL of DMSO.

Chapter 4

Conclusions and Future Work

4.1 Conclusions

In this thesis, we aimed to explore SO_2 and CO_2 adsorption. In Chapter 2, we focused on the design of an SO_2 system. We were able to successfully build a SO_2 gas generator that produced a range of different SO_2 concentrations (depending on the HCl concentration used in the permeation tube). We were also able to apply a variety of external modifications (e.g., insulation, compression fittings, and quartz fibre filters) to achieve a more stable SO_2 concentration output on the gas analyzer. While we didn't get a chance to focus on MOF adsorption (see section 4.3.1), this work lays the groundwork for all the future studies. In Chapter 3, we made two new MOFs with a relatively new topology (only three other examples of this topology are known, one of which the authors admit cannot be reproduced). The $Zn_3(NH_2BDC)_3DABCO$ system showed the central zinc forms a Zn–O bond length of 2.086(2) Å. In a slightly modified system, we were able to swap out the zinc metal centre for a cadmium atom to form $Zn_2Cd(NH_2BDC)_3DABCO$, which has a Cd–O bond of 2.244(15) Å. The cadmium version of the MOF has a slightly larger bond length which in turn, has a direct impact on the pore size and aperture of the material. We were able to properly activate both materials, and we opted to utilize solvent-assisted activation in comparison to thermal activation. We soaked both of the materials in methanol and gently heated them under vacuum to ensure there was no presence of solvent molecules in the pores, therefore optimizing the adsorption potential for both materials. In terms of gas sorption studies completed using CO, CO_2, and nitrogen gas, the pore aperture of $Zn_3(NH_2BDC)_3DABCO$ was concluded to be between 3.30 and 3.64 Å. For $Zn_2Cd(NH_2BDC)_3DABCO$, it can be concluded that the pore aperture of this material is larger than 3.60 Å. These results mean that both $Zn_3(NH_2BDC)_3DABCO$ and $Zn_2Cd(NH_2BDC)_3DABCO$ have the gas adsorption potential to molecularly sieve toxic gas chemicals (CO) from benign chemicals (CO_2), specifically in flue streams present as a result of industries burning fossil fuels. As with any good project, there is always more to be explored. If there was more time permitting, then the section below will tell you more about what I would have done.

4.2 Future Work for Sulfur Dioxide Gas Permeation System

As demonstrated in this thesis, we have developed a tunable SO_2 source that produces SO_2 gas in a range of concentrations. Although the initial results of the stability experiments showed reproducibility with each HCl concentration, the next step in this project would be to repeat each of the datasets at 30, 40, 50, and 60 °C with each HCl concentration (1 M – 6 M). Ideally, triplicate data is necessary to demonstrate the reproducibility of this work. Triplicate results are vital for this custom SO_2 source, as data accuracy is extremely important for this project, prior to any exposure of porous material to the gas.

As seen in the thesis, a number of external modifications were made to the SO_2 gas permeation device. For instance, compression fittings were used, insulation to the aluminum block was added, and filters were placed inside of the compression fittings. All of these modifications seemed to improve the stability of the gas permeation device. That being said, there were still times during the course of this work where the stability of the gas output mixing ratio seemed to waiver. For example, it would take approximately two to three days before the SO_2 concentration reached a relatively constant gas output. In my opinion, this issue was related to the gas flow in the instrument. All throughout the project, numerous permeation tubes and salt beds were tested. In regard to the permeation tubes, each of the different HCl concentrations were tested and calibrated prior to placing the solution inside of the permeation tubes. Once the HCl solutions were made up, I took the extra step to titrate the HCl solution with a sodium hydroxide solution and phenolphthalein indication to accurately quantify the concentration of the acid solutions. These results made me extremely confident that the permeation tubes were not the issue with concentration stability in the experiments. The other main part of the gas permeation device was the salt bed. In regard to this, the makeup of the salt bed is relativity simple. The only modifications, other than changing the salt out for a different salt, would be to add dispersants. Dispersants are small pieces of PFA tubing that are approximately 1 mm in size. The dispersants provide additional surface area in which gases may react. In other words, dispersants increase the possible reaction sites for the HCl gas and salt, providing optimal SO_2 gas production.

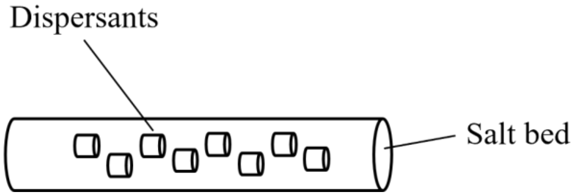

Figure 4.1. Dispersants housed inside of a salt bed.

In addition to trying dispersants in the salt bed, another factor I would like to explore is the gas flow. Since the gas flow is controlled by a regulator on the nitrogen gas cylinder, a range of gas flow was selected for the experiments between 100 – 150 sccm. It was difficult to set the regulator for the exact same gas flow for each experiment, since we were working with small gas flows. To correct for this issue, I would like to install critical orifices before the gas permeation device to ensure a constant gas glow is being provided. Critical orifices are used to act as flow restrictors. Essentially, they are added to the tubing via appropriate gas-related fittings, and inside of the critical orifices are very small diameter openings. These openings only allow a specific amount of gas to pass through. In other words, they restrict the gas flow to the desired amount needed for the experiment. This addition of critical orifices would allow for a precise amount of gas in each experiment; thus, hopefully controlling the SO_2 gas output to be optimally stable. With all of these new changes and a stable SO_2 concentration produced, the next step in this thesis would be to explore porous materials on the source.

4.3 Future Work Using MOFs in Sulfur Dioxide Adsorption

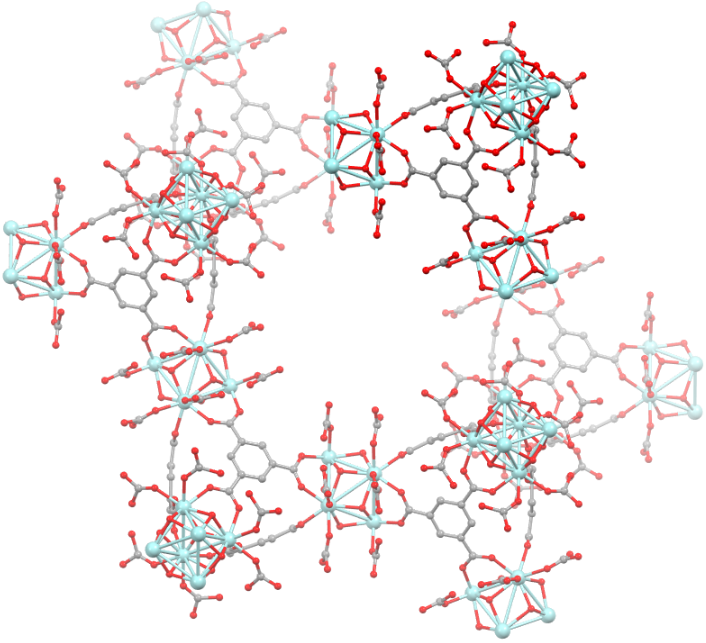

Figure 4.2. 3-D crystal structure of MOF-808 illustrating an adamantane cage with a large internal pore diameter: Zr, blue; C, grey; O, red.

Previously in the group, the adsorption properties of MOF-808 have been studied. MOF-808 is a porous material that is formed from $[Zr_6O_4(OH)_4]^{12+}$ clusters bound to trimesic acid (BTC) linkers. Each cluster contains one terminal water group and one terminal hydroxide group for each zirconium metal centre, leaving the metal centre unsaturated and free to interact with gas molecules. The crystal structure of MOF-808 is shown below in Figure 4.2. As can be observed in the figure, MOF-808 has a large internal pore and the terminal water and hydroxide groups present on each zirconium metal centre can be observed. As observed in Figure 4.2, MOF-808 contains a large amount of these terminal water and hydroxide groups; therefore, MOF-808 has the potential to adsorb significant amounts of gas.

Due to the presence of these terminal water and hydroxide groups, we predicted this MOF would be ideal at adsorbing gases. Preliminary work hypothesized the terminal water and hydroxide groups present on the metal centres may react with SO_2 to form coordinated sulfuric acid or sulfite groups as illustrated below in Figure 4.3. Zhang et al. showed, through a series of breakthrough experiments, that MOF-808 uptakes SO_2 at a dynamic loading of 0.53 mmol/g when exposed to concentrations of 1000 ppb of SO_2. This is a promising result observed for MOF-808 but requires further breakthrough experiments. In addition to these breakthrough experiments, the structural stability and mechanistic studies must be completed.

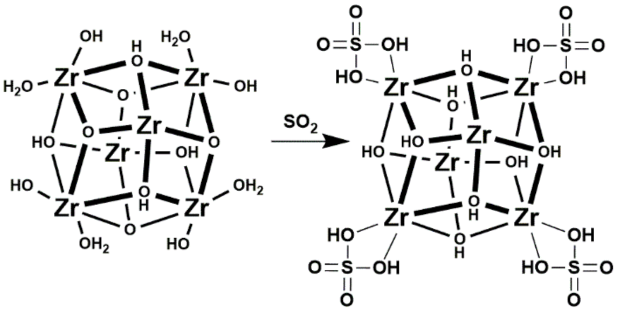

Figure 4.3. Proposed reactivity of the node in MOF-808 with SO_2.

Although we were unable to complete a full study on the adsorption properties of SO_2 utilizing MOF-808, we were able to successfully complete one trial exposure. When exposing any MOF to a stream of SO_2 gas, a positive control must first be obtained (Figure 4.4, a). A positive control is defined as a point at which a constant amount of gas is being produced. Once a positive control is obtained, the MOF is exposed to the gas. Ideally, if gas adsorption occurs, we should observe the gas mixing ratio reduce to zero. As the pores of the MOF begin to fill up, the gas mixing ratio increases until it reaches the output generated from the positive control (Figure 4.4, a). In our initial results for MOF-808, we were able to observe similar behavior in terms of the adsorption cycle. This is a promising result but requires many more trial exposures to determine whether we are adsorbing significant amounts of SO_2 gas. It would also be interesting to determine if the method of adsorption is occurring via chemisorption or physisorption to observe whether the terminal hydroxyl groups are playing a role in the reaction with SO_2.

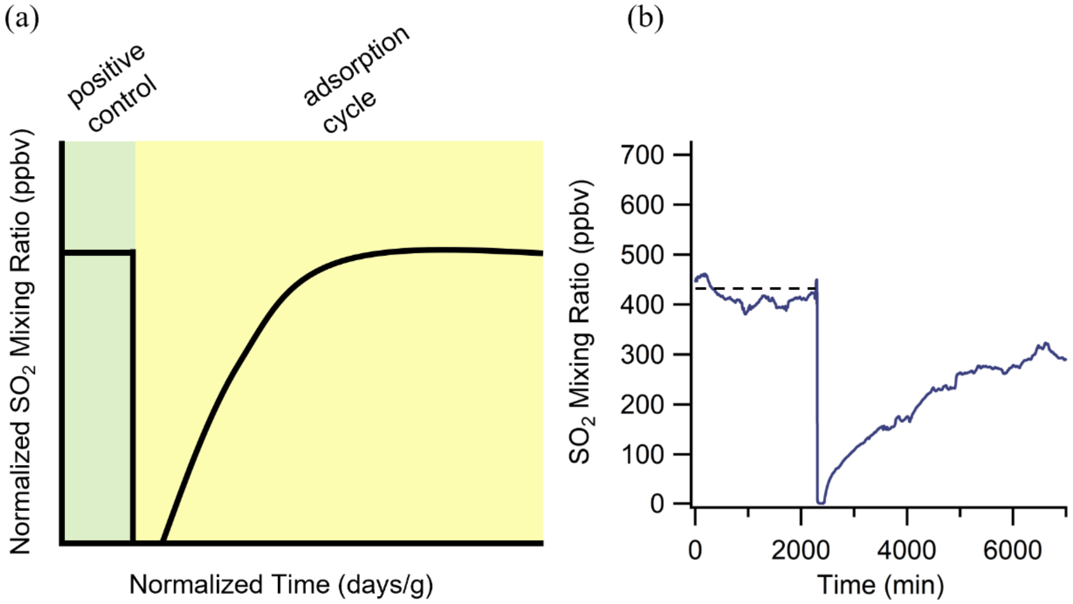

Figure 4.4. Outline of a generic MOF exposure to a gas (a) and results of exposing MOF-808 to SO_2 gas (b).

In addition to SO_2 reacting with terminal hydroxide groups, it has been shown that it reacts well with DABCO (Figure 4.5). The SO_2 group is able to chemically react with DABCO to form a stable product known as DABSO.[155] With this in mind, it may be possible to incorporate DABCO as a reaction site in MOFs. To accomplish this, carboxylic acid functional groups must be installed on the DABCO ligand. If DABCO is present with no carboxylate groups, DABCO acts as the Lewis-base, which leaves no possible reactivity with SO_2 gas as the nitrogen atom is already coordinated in a MOF. Instead, we can functionalize DABCO with carboxylic acids, and therefore, the carboxylate groups may act as the Lewis-base to form a MOF. If this is possible, the nitrogen atoms present on the DABCO itself may further react with SO_2.

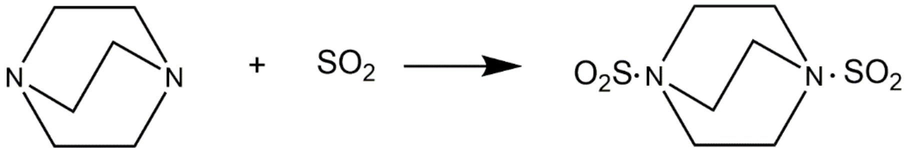

Figure 4.5. Chemical reactivity of DABCO with SO_2 to form DABSO.

In conclusion, this project should focus on achieving a completely stable SO_2 source, and then begin testing different MOFs on the gas permeation device. With SO_2 as the target gas for adsorption, the project should focus on testing materials that have functional groups that have been shown to react well with SO_2 gas. Ideally, in the industry field, it would be financially beneficial to develop a MOF that reacts with SO_2 gas by physisorption. Since both of my examples above are chemisorption-based, it may be important to focus our efforts on designing a MOF that adsorbs SO_2 via physisorption. If physisorption occurs, it may be possible to remove the SO_2 gas in a safely manner and reuse the porous MOF for additional uses. If such a material is developed, the long-term goal for this project is to implement MOFs in industries that produce SO_2 as a by-product.

4.4 Additional Experiments on the $M_3(NH_2BDC)_3DABCO$ Family

4.4.1 Gas Adsorption Experiments for Pore Aperture Studies

As demonstrated in this thesis, we were able to conclude that $Zn_3(NH_2BDC)_3DABCO$ was only able to adsorb CO_2 gas (neither nitrogen gas and CO gas were able to enter the pores). Therefore, it can be concluded that the pore aperture of this material is between 3.30 and 3.64 Å. When we replaced one of the metal centres with a larger atom, such as cadmium, to form $Zn_2Cd(NH_2BDC)_3DABCO$, the MOF was able to uptake both CO_2 and nitrogen gas. It was not able to uptake any amounts of CO gas. Therefore, it can be concluded that the pore aperture of this material is larger than 3.64 Å. In order to determine a more accurate pore aperture for both materials, further gas adsorption experiments must be obtained with gases that are able to readily adsorb onto a surface and have kinetic diameters larger than 3.64 Å. To ensure that the interpretation of the data is clear, adsorption of the same gas on a prototypical MOF with considerably large pore apertures should be examined. If the two MOFs show similar gas adsorption, then it is likely that the gas is not "sticky" enough. However, if the prototypical MOF adsorbs a gas while $Zn_2Cd(NH_2BDC)_3DABCO$ does not, then it is clear that a limit to the pore aperture has been found.

For $Zn_3(NH_2BDC)_3DABCO$, we were able to conclude the pore aperture was between 3.30 and 3.64 Å. If we take a look at the kinetic diameter of other gases, we can see that oxygen gas has a kinetic diameter if 3.46 Å which is in between that of CO_2 and nitrogen gas. We can collect oxygen isotherms to determine whether oxygen gas can enter the pores of $Zn_3(NH_2BDC)_3DABCO$. Based on the results of those experiments, we can continue to perform gas adsorption studies with other gases until we are able to accurately determine the pore aperture of the material.

As for $Zn_2Cd(NH_2BDC)_3DABCO$, the material was determined to have a pore aperture larger than 3.64 Å. We can continue to test the material with gases that have a kinetic diameter larger than 3.64 Å, such as methane gas which has a kinetic diameter of 3.80 Å, to accurately measure the pore aperture of the material.

4.4.2 Further Synthetic Experiments

As seen in this thesis, we were able to synthesize two new materials: $Zn_3(NH_2BDC)_3DABCO$ and $Zn_2Cd(NH_2BDC)_3DABCO$. A variety of transition metals were studied to try and swap out the metal centres, but ultimately only zinc and cadmium formed a product. A number of transition metals were attempted which included copper, aluminum, and cobalt; therefore, I would like to try more transition metals using the same synthesis used to make $Zn_3(NH_2BDC)_3DABCO$. If we are able to switch the metal centres out for the MOF, we would be able to further tune the properties of the material. Since cadmium was able to slightly increase the pore aperture of material compared to a zinc metal centre in the central octahedral position, we may be able to achieve similar results by switching to a smaller or bigger atom in this position. If we are able to do so, we can control the gas-uptake properties even further. This may be helpful in terms of gas mixtures, in which we are interested in selectivity adsorbing one gas over another.

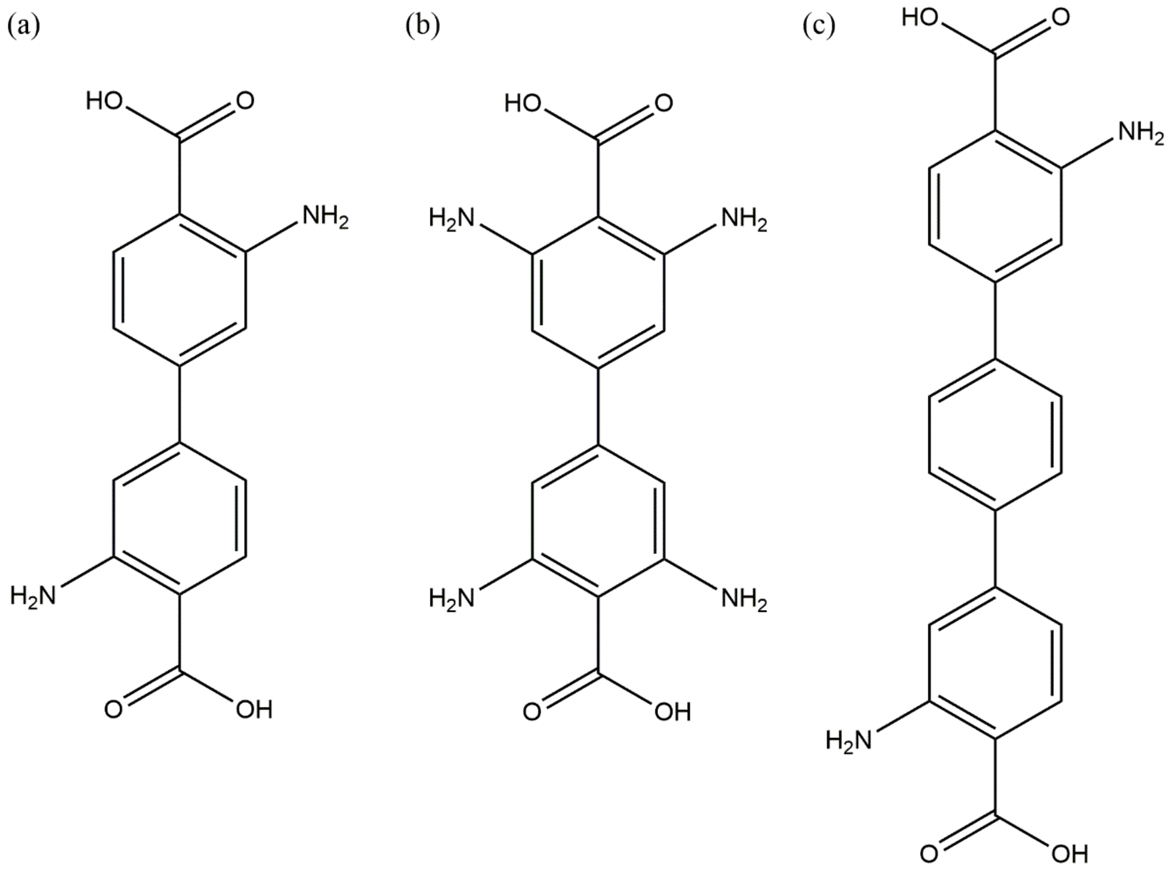

Figure 4.6. Possible ligands that may aid in designing larger pores for the $M_3(NH_2BDC)_3DABCO$ family: H_2-$(NH_2)_2BPDC$ (a), H_2-$(NH_2)_4BPDC$ (b), and H_2-$(NH_2)_2TPDC$.

In addition to changing the metal centres of the MOF, I would also like to explore different ligands in more depth. We attempted to install BPDC as the ligand in $Zn_3(NH_2BDC)_3DABCO$, but no desired result was achieved. If we are able to synthesize H_2-NH_2BPDC (with the additional amine functionality on the ligand ortho to the carboxylate) and try to incorporate it into the material, it may be possible to create an even larger pore for gas adsorption to occur (Figure 4.6). In addition, we can continue to try and grow the pore by trying to incorporate H_2-NH_2TPDC (2'-amino-1,1':4,1''-terphenyl-4,4''-dicarboxylic acid) into the material (Figure 4.6). If these derivatives would allow us to access a large pore version of this new topology, then it would likely not act as a molecular sieve. However, it would allow us to examine the gas adsorption and stability of these systems with respect to other applications.

References

1. Hall, M. R.; Allinson, D., 1 - heat and mass transport processes in building materials. In *Materials for energy efficiency and thermal comfort in buildings*, Hall, M. R., Ed. Woodhead Publishing: 2010; pp 3-53.
2. Aquino, C.; Maschmeyer, T., Chapter 1 - a new family of mesoporous oxides—synthesis, characterisation and applications of tud-1. In *Ordered porous solids*, Valtchev, V.; Mintova, S.; Tsapatsis, M., Eds. Elsevier: Amsterdam, 2009; pp 3-30.
3. Li, H.; Wang, K.; Sun, Y.; Lollar, C. T.; Li, J.; Zhou, H.-C., Recent advances in gas storage and separation using metal–organic frameworks. *Mater. Today.* **2018,** *21* (2), 108-121.
4. Li, B.; Wen, H.-M.; Zhou, W.; Chen, B., Porous metal–organic frameworks for gas storage and separation: What, how, and why? *J. Phys. Chem. Lett.* **2014,** *5* (20), 3468-3479.
5. Connolly, B. M.; Madden, D. G.; Wheatley, A. E. H.; Fairen-Jimenez, D., Shaping the future of fuel: Monolithic metal–organic frameworks for high-density gas storage. *J. Am. Chem. Soc.* **2020,** *142* (19), 8541-8549.
6. Konstas, K.; Osl, T.; Yang, Y.; Batten, M.; Burke, N.; Hill, A. J.; Hill, M. R., Methane storage in metal organic frameworks. *J. Mater. Chem.* **2012,** *22* (33), 16698-16708.
7. Ahmed, A.; Seth, S.; Purewal, J.; Wong-Foy, A. G.; Veenstra, M.; Matzger, A. J.; Siegel, D. J., Exceptional hydrogen storage achieved by screening nearly half a million metal-organic frameworks. *Nat. Commun.* **2019,** *10* (1), 1568.

8. Gándara, F.; Furukawa, H.; Lee, S.; Yaghi, O. M., High methane storage capacity in aluminum metal–organic frameworks. *J. Am. Chem. Soc.* **2014,** *136* (14), 5271-5274.

9. Britt, D.; Tranchemontagne, D.; Yaghi, O. M., Metal-organic frameworks with high capacity and selectivity for harmful gases. *Proc. Natl. Acad. Sci.* **2008,** *105* (33), 11623.

10. Wang, C.; An, B.; Lin, W., Metal–organic frameworks in solid–gas phase catalysis. *ACS Catal.* **2019,** *9* (1), 130-146.

11. Hwang, Y. K.; Hong, D. Y.; Chang, J. S.; Jhung, S. H.; Seo, Y. K.; Kim, J.; Vimont, A.; Daturi, M.; Serre, C.; Férey, G. J. A. C., Amine grafting on coordinatively unsaturated metal centers of mofs: Consequences for catalysis and metal encapsulation. *Angew. Chem. Int. Ed.* **2008,** *120* (22), 4212-4216.

12. Yang, D.; Gates, B. C., Catalysis by metal organic frameworks: Perspective and suggestions for future research. *ACS Catal.* **2019,** *9* (3), 1779-1798.

13. Mondloch, J. E.; Katz, M. J.; Isley Iii, W. C.; Ghosh, P.; Liao, P.; Bury, W.; Wagner, G. W.; Hall, M. G.; DeCoste, J. B.; Peterson, G. W.; Snurr, R. Q.; Cramer, C. J.; Hupp, J. T.; Farha, O. K., Destruction of chemical warfare agents using metal–organic frameworks. *Nat. Mater.* **2015,** *14* (5), 512-516.

14. Rasheed, T.; Rizwan, K.; Bilal, M.; Iqbal, H. M. N., Metal-organic framework-based engineered materials-fundamentals and applications. *Molecules.* **2020,** *25* (7), 1598.

15. Zhang, M.; Huang, B.; Jiang, H.; Chen, Y., Metal-organic framework loaded manganese oxides as efficient catalysts for low-temperature selective catalytic reduction of no with nh3. *Front. Chem. Sci. Eng.* **2017,** *11* (4), 594-602.

16. Li, H.-Y.; Zhao, S.-N.; Zang, S.-Q.; Li, J., Functional metal–organic frameworks as effective sensors of gases and volatile compounds. *Chem. Soc. Rev.* **2020,** *49* (17), 6364-6401.

17. Koo, W.-T.; Jang, J.-S.; Kim, I.-D., Metal-organic frameworks for chemiresistive sensors. *Chem.* **2019,** *5* (8), 1938-1963.

18. Achmann, S.; Hagen, G.; Kita, J.; Malkowsky, I. M.; Kiener, C.; Moos, R., Metal-organic frameworks for sensing applications in the gas phase. *Sensors (Basel).* **2009,** *9* (3), 1574-89.

19. Fang, X.; Zong, B.; Mao, S., Metal–organic framework-based sensors for environmental contaminant sensing. *Nano Lett.* **2018,** *10* (4), 64.

20. Tchalala, M. R.; Bhatt, P. M.; Chappanda, K. N.; Tavares, S. R.; Adil, K.; Belmabkhout, Y.; Shkurenko, A.; Cadiau, A.; Heymans, N.; De Weireld, G.; Maurin, G.; Salama, K. N.; Eddaoudi, M., Fluorinated mof platform for selective removal and sensing of so2 from flue gas and air. *Nat. Commun.* **2019,** *10* (1), 1328.

21. Furlong, B. J.; Katz, M. J., Bistable dithienylethene-based metal–organic framework illustrating optically induced changes in chemical separations. *J. Am. Chem. Soc.* **2017,** *139* (38), 13280-13283.

22. McGrath, D. T.; Ryan, M. D.; MacInnis, J. J.; VandenBoer, T. C.; Young, C. J.; Katz, M. J., Selective decontamination of the reactive air pollutant nitrous acid via node-linker cooperativity in a metal–organic framework. *Chem. Sci.* **2019,** *10* (21), 5576-5581.

23. Lawrence, M. C.; Schneider, C.; Katz, M. J., Determining the structural stability of uio-67 with respect to time: A solid-state nmr investigation. *Chem. Commun.* **2016,** *52* (28), 4971-4974.

24. Zhang, J.; White, G. B.; Ryan, M. D.; Hunt, A. J.; Katz, M. J., Dihydrolevoglucosenone (cyrene) as a green alternative to n,n-dimethylformamide (dmf) in mof synthesis. *ACS Sustain. Chem. Eng.* **2016,** *4* (12), 7186-7192.

25. Furukawa, H.; Cordova, K. E.; O'Keeffe, M.; Yaghi, O. M., The chemistry and applications of metal-organic frameworks. *Science.* **2013,** *341* (6149), 1230444.

26. Zhou, H.-C. J.; Kitagawa, S., Metal–organic frameworks (mofs). *Chem. Soc. Rev.* **2014,** *43* (16), 5415-5418.

27. Hall, J. N.; Bollini, P., Structure, characterization, and catalytic properties of open-metal sites in metal organic frameworks. *React Chem. Eng.* **2019,** *4* (2), 207-222.

28. Cook, T. R.; Zheng, Y.-R.; Stang, P. J., Metal-organic frameworks and self-assembled supramolecular coordination complexes: Comparing and contrasting the design, synthesis, and functionality of metal-organic materials. *Chem. Rev.* **2013,** *113* (1), 734-777.

29. Lu, W.; Wei, Z.; Gu, Z.-Y.; Liu, T.-F.; Park, J.; Park, J.; Tian, J.; Zhang, M.; Zhang, Q.; Gentle Iii, T.; Bosch, M.; Zhou, H.-C., Tuning the structure and function of metal–organic frameworks via linker design. *Chem. Soc. Rev.* **2014,** *43* (16), 5561-5593.

30. Moosavi, S. M.; Nandy, A.; Jablonka, K. M.; Ongari, D.; Janet, J. P.; Boyd, P. G.; Lee, Y.; Smit, B.; Kulik, H. J., Understanding the diversity of the metal-organic framework ecosystem. *Nat. Commun.* **2020,** *11* (1), 4068.

31. Yakovenko, A. A.; Reibenspies, J. H.; Bhuvanesh, N.; Zhou, H.-C., Generation and applications of structure envelopes for porous metal–organic frameworks. *J. Appl. Crystallogr.* **2013,** *46* (2), 346-353.

32. Øien, S.; Wragg, D.; Reinsch, H.; Svelle, S.; Bordiga, S.; Lamberti, C.; Lillerud, K. P., Detailed structure analysis of atomic positions and defects in zirconium metal–organic frameworks. *Cryst. Growth Des.* **2014,** *14* (11), 5370-5372.

33. Kim, H.; Chun, H.; Kim, G.-H.; Lee, H.-S.; Kim, K., Vapor phase inclusion of ferrocene and its derivative in a microporous metal–organic porous material and its structural characterization by single crystal x-ray diffraction. *Chem. Commun.* **2006,** (26), 2759-2761.

34. Erkey, C., Chapter 4 - thermodynamics and dynamics of adsorption of metal complexes on surfaces from supercritical solutions. In *Supercritical fluid science and technology*, Erkey, C., Ed. Elsevier: 2011; Vol. 1, pp 41-77.

35. Thommes, M.; Kaneko, K.; Neimark, A. V.; Olivier, J. P.; Rodriguez-Reinoso, F.; Rouquerol, J.; Sing, K. S. W., Physisorption of gases, with special reference to the evaluation of surface area and pore size distribution (iupac technical report). *Pure Appl. Chem.* **2015,** *87* (9-10), 1051-1069.

36. Wang, H.; Mahle, J. J.; Tovar, T. M.; Peterson, G. W.; Hall, M. G.; DeCoste, J. B.; Buchanan, J. H.; Karwacki, C. J., Solid-phase detoxification of chemical warfare agents using zirconium-based metal organic frameworks and the moisture effects: Analyze via digestion. *ACS Appl. Mater. Interfaces.* **2019,** *11* (23), 21109-21116.

37. Katz, M.; Mondloch, J.; Totten, R.; Park, J. K.; Nguyen, S.; Farha, O.; Hupp, J., Simple and compelling biomimetic metal-organic framework catalyst for the degradation of nerve agent simulants. *Angew. Chem. Int. Ed.* **2014,** *53*.

38. Banerjee, S.; Chattopadhyaya, M. C., Adsorption characteristics for the removal of a toxic dye, tartrazine from aqueous solutions by a low cost agricultural by-product. *Arab. J. Chem.* **2017,** *10*, S1629-S1638.

39. Manisalidis, I.; Stavropoulou, E.; Stavropoulos, A.; Bezirtzoglou, E., Environmental and health impacts of air pollution: A review. *Front. Public Health.* **2020,** *8* (14).

40. Chiodo, G.; Polvani, L. M.; Marsh, D. R.; Stenke, A.; Ball, W.; Rozanov, E.; Muthers, S.; Tsigaridis, K., The response of the ozone layer to quadrupled co2 concentrations %. *J. Clim.* **2018,** *31* (10), 3893-3907.

41. Stolarski, R. S.; Douglass, A. R.; Oman, L. D.; Waugh, D. W., Impact of future nitrous oxide and carbon dioxide emissions on the stratospheric ozone layer. *Environ. Res. Lett.* **2015,** *10* (3), 034011.

42. Rosenfield, J. E.; Douglass, A. R.; Considine, D. B., The impact of increasing carbon dioxide on ozone recovery. *J. Geophys. Res.* **2002,** *107*.

43. Andersen, S. O.; Halberstadt, M. L.; Borgford-Parnell, N., Stratospheric ozone, global warming, and the principle of unintended consequences—an ongoing science and policy success story. *J. Air Waste Manage. Assoc.* **2013,** *63* (6), 607-647.

44. Tan, W.; Liu, C.; Wang, S.; Xing, C.; Su, W.; Zhang, C.; Xia, C.; Liu, H.; Cai, Z.; Liu, J., Tropospheric no2, so2, and hcho over the east china sea, using ship-based max-doas observations and comparison with omi and omps satellite data. *Atmos. Chem. Phys.* **2018,** *18* (20), 15387-15402.

45. Rollins, A. W.; Thornberry, T. D.; Atlas, E.; Navarro, M.; Schauffler, S.; Moore, F.; Elkins, J. W.; Ray, E.; Rosenlof, K.; Aquila, V.; Gao, R.-S., So2 observations and

sources in the western pacific tropical tropopause region. *J. Geophys. Res.* **2018,** *123* (23), 13,549-13,559.

46. Richter, A.; Burrows, J. P.; Nüß, H.; Granier, C.; Niemeier, U., Increase in tropospheric nitrogen dioxide over china observed from space. *Nature.* **2005,** *437* (7055), 129-132.
47. Khalil, M. A. K.; Rasmussen, R. A., Carbon monoxide in the earth's atmosphere: Indications of a global increase. *Nature.* **1988,** *332* (6161), 242-245.
48. Kanniche, M.; Gros-Bonnivard, R.; Jaud, P.; Valle-Marcos, J.; Amann, J.-M.; Bouallou, C., Pre-combustion, post-combustion and oxy-combustion in thermal power plant for co capture. *Appl. Therm. Eng.* **2010,** *30*, 53-62.
49. Moioli, S.; Giuffrida, A.; Gamba, S.; Romano, M. C.; Pellegrini, L.; Lozza, G., Pre-combustion co2 capture by mdea process in igcc based on air-blown gasification. *Energy Procedia.* **2014,** *63*, 2045-2053.
50. Rosenberg, H. S.; Curran, L. M.; Slack, A. V.; Ando, J.; Oxley, J. H., Post combustion methods for control of nox emissions. *Prog. Energy Combust. Sci.* **1980,** *6* (3), 287-302.
51. Wang, Y.; Zhao, L.; Otto, A.; Robinius, M.; Stolten, D., A review of post-combustion co2 capture technologies from coal-fired power plants. *Energy Procedia.* **2017,** *114*, 650-665.
52. Duke, M. C.; Ladewig, B.; Smart, S.; Rudolph, V.; Diniz da Costa, J. C., Assessment of postcombustion carbon capture technologies for power generation. *Front. Chem. Eng. China.* **2010,** *4* (2), 184-195.
53. Savage, M.; Cheng, Y.; Easun, T. L.; Eyley, J. E.; Argent, S. P.; Warren, M. R.; Lewis, W.; Murray, C.; Tang, C. C.; Frogley, M. D.; Cinque, G.; Sun, J.; Rudić, S.; Murden, R. T.; Benham, M. J.; Fitch, A. N.; Blake, A. J.; Ramirez-Cuesta, A. J.; Yang,

S.; Schröder, M., Selective adsorption of sulfur dioxide in a robust metal–organic framework material. *Adv. Mater.* **2016,** *28* (39), 8705-8711.

54. Karplus, V. J.; Zhang, S.; Almond, D., Quantifying coal power plant responses to tighter emissions standards in china. *Proc. Natl. Acad. Sci.* **2018,** *115* (27), 7004.
55. Chen, T. M.; Gokhale, J.; Shofer, S.; Kuschner, W. G., Outdoor air pollution: Nitrogen dioxide, sulfur dioxide, and carbon monoxide health effects. *Am. J. Med. Sci.* **2007,** *333* (4), 249-56.
56. Lin, C.-K.; Lin, R.-T.; Chen, P.-C.; Wang, P.; De Marcellis-Warin, N.; Zigler, C.; Christiani, D. C., A global perspective on sulfur oxide controls in coal-fired power plants and cardiovascular disease. *Sci. Rep.* **2018,** *8* (1), 2611.
57. Saygın, M.; Gonca, T.; Öztürk, Ö.; Has, M.; Çalışkan, S.; Has, Z. G.; Akkaya, A., To investigate the effects of air pollution (pm10 and so(2)) on the respiratory diseases asthma and chronic obstructive pulmonary disease. *Turk. Thorac. J.* **2017,** *18* (2), 33-39.
58. Sunyer, J.; Atkinson, R.; Ballester, F.; Le Tertre, A.; Ayres, J. G.; Forastiere, F.; Forsberg, B.; Vonk, J. M.; Bisanti, L.; Anderson, R. H.; Schwartz, J.; Katsouyanni, K., Respiratory effects of sulphur dioxide: A hierarchical multicity analysis in the aphea 2 study. *Occup. Environ. Med.* **2003,** *60* (8).
59. Charan, N. B.; Myers, C. G.; Lakshminarayan, S.; Spencer, T. M., Pulmonary injuries associated with acute sulfur dioxide inhalation. *Am. Rev. Respir. Dis.* **1979,** *119* (4), 555-560.
60. Reno, A. L.; Brooks, E. G.; Ameredes, B. T., Mechanisms of heightened airway sensitivity and responses to inhaled so2 in asthmatics. *Environ. Health Insights.* **2015,** *9* (Suppl 1), 13-25.

61. Ji, Z.; Fan, X.; Gan, M.; Chen, X.; Lv, W.; Li, Q.; Zhou, Y.; Tian, Y.; Jiang, T., Influence of sulfur dioxide-related interactions on pm(2.5) formation in iron ore sintering. *J. Air Waste Manage. Assoc.* **2017,** *67* (4), 488-497.

62. Chen, C.; Allen, C. A.; Cohen, S. M., Tandem postsynthetic modification of metal–organic frameworks using an inverse-electron-demand diels–alder reaction. *Inorg. Chem.* **2011,** *50* (21), 10534-10536.

63. Ray, S.; Kim, K.-H., The pollution status of sulfur dioxide in major urban areas of korea between 1989 and 2010. *Atmos. Res.* **2014,** *147-148*, 101-110.

64. Xing, Y.-F.; Xu, Y.-H.; Shi, M.-H.; Lian, Y.-X., The impact of pm2.5 on the human respiratory system. *J. Thorac. Dis.* **2016,** *8* (1), 69-74.

65. Anderson, J. O.; Thundiyil, J. G.; Stolbach, A., Clearing the air: A review of the effects of particulate matter air pollution on human health. *J. Med. Toxicol.* **2012,** *8* (2), 166-175.

66. Piccione, G.; Lutri, L.; Casella, S.; Ferrantelli, V.; Pennisi, P., Effect of shearing and environmental conditions on physiological mechanisms in ewes. *J. Environ. Biol.* **2008,** *29* (6), 877-80.

67. Grennfelt, P.; Engleryd, A.; Forsius, M.; Hov, Ø.; Rodhe, H.; Cowling, E., Acid rain and air pollution: 50 years of progress in environmental science and policy. *Ambio.* **2020,** *49* (4), 849-864.

68. Burns, D. A.; Aherne, J.; Gay, D. A.; Lehmann, C. M. B., Acid rain and its environmental effects: Recent scientific advances. *Atmos. Environ.* **2016,** *146*, 1-4.

69. Rodhe, H.; Dentener, F.; Schulz, M., The global distribution of acidifying wet deposition. *Environ. Sci. Technol.* **2002,** *36* (20), 4382-4388.

70. Wu, Y.; Liu, J.; Zhai, J.; Cong, L.; Wang, Y.; Ma, W.; Zhang, Z.; Li, C., Comparison of dry and wet deposition of particulate matter in near-surface waters during summer. *PLoS One.* **2018,** *13* (6), 0199241.

71. Singh, A.; Agrawal, M., Acid rain and its ecological consequences. *J. Environ. Biol.* **2008,** *29*, 15-24.

72. Likens, G.; Driscoll, C., Long-term effects of acid rain: Response and recovery of a forest ecosystem. *Science.* **1996,** *272*, 244-246.

73. DeHayes, D. H.; Schaberg, P. G.; Hawley, G. J.; Strimbeck, G. R., Acid rain impacts on calcium nutrition and forest health: Alteration of membrane-associated calcium leads to membrane destabilization and foliar injury in red spruce. *Bioscience.* **1999,** *49* (10), 789-800.

74. Schreiber, R. K.; Newman, J. R., Acid precipitation effects on forest habitats: Implications for wildlife. *Conserv. Biol.* **1988,** *2* (3), 249-259.

75. Chandra Srivastava, V., An evaluation of desulfurization technologies for sulfur removal from liquid fuels. *RSC Adv.* **2012,** *2* (3), 759-783.

76. Clean air act. United States Environmenal Protection Agency: 1970.

77. Viana, M.; Hammingh, P.; Colette, A.; Querol, X.; Degraeuwe, B.; Vlieger, I. d.; van Aardenne, J., Impact of maritime transport emissions on coastal air quality in europe. *Atmos. Environ.* **2014,** *90*, 96-105.

78. Sofiev, M.; Winebrake, J. J.; Johansson, L.; Carr, E. W.; Prank, M.; Soares, J.; Vira, J.; Kouznetsov, R.; Jalkanen, J.-P.; Corbett, J. J., Cleaner fuels for ships provide public health benefits with climate tradeoffs. *Nat. Commun.* **2018,** *9* (1), 406.

79. Olmer, N.; Comer, B.; Roy, B.; Mao, X.; Rutherford, D. *Greenhouse gas emissions from global shipping, 2013–2015*; 2017.

80. Duchatelle, L., Oceanex: 2017.

81. Srivastava, R. K.; Jozewicz, W., Flue gas desulfurization: The state of the art. *J. Air Waste Manage. Assoc.* **2001,** *51* (12), 1676-1688.

82. Good, K. D.; VanBriesen, J. M., Coal-fired power plant wet flue gas desulfurization bromide discharges to u.S. Watersheds and their contributions to drinking water sources. *Environ. Sci. Technol.* **2019,** *53* (1), 213-223.

83. Slack, A. V., Flue gas desulfurization/lime-limestone scrubbing design considerations. *Chem. Eng. Prog.* **1978,** *74* (2).

84. DuPont, A., Improving and monitoring air quality. *Environ. Sci. Pollut. Res. Int.* **2018,** *25* (15), 15253-15263.

85. Jiang, J.; Gándara, F.; Zhang, Y.-B.; Na, K.; Yaghi, O. M.; Klemperer, W. G., Superacidity in sulfated metal–organic framework-808. *J. Am. Chem. Soc.* **2014,** *136* (37), 12844-12847.

86. Nuhnen, A.; Janiak, C., A practical guide to calculate the isosteric heat/enthalpy of adsorption via adsorption isotherms in metal–organic frameworks, mofs. *Dalton Trans.* **2020,** *49* (30), 10295-10307.

87. Zárate, J. A.; Sánchez-González, E.; Williams, D. R.; González-Zamora, E.; Martis, V.; Martínez, A.; Balmaseda, J.; Maurin, G.; Ibarra, I. A., High and energy-efficient reversible so2 uptake by a robust sc(iii)-based mof. *J. Mater. Chem. A.* **2019,** *7* (26), 15580-15584.

88. Brandt, P.; Nuhnen, A.; Lange, M.; Möllmer, J.; Weingart, O., Mofs with potential application for so2 separation and flue gas desulfurization. *ACS Appl. Mater. Interfaces.* **2019,** *11*.

89. Carter, J. H.; Han, X.; Moreau, F. Y.; da Silva, I.; Nevin, A.; Godfrey, H. G. W.; Tang, C. C.; Yang, S.; Schröder, M., Exceptional adsorption and binding of sulfur dioxide in a robust zirconium-based metal–organic framework. *J. Am. Chem. Soc.* **2018,** *140* (46), 15564-15567.

90. Han, X.; Yang, S.; Schröder, M., Porous metal–organic frameworks as emerging sorbents for clean air. *Nat. Rev. Chem.* **2019,** *3* (2), 108-118.

91. Hungerford, J.; Bhattacharyya, S.; Tumuluri, U.; Nair, S.; Wu, Z.; Walton, K. S., Dmof-1 as a representative mof for so2 adsorption in both humid and dry conditions. *J. Phys. Chem. C.* **2018,** *122* (41), 23493-23500.

92. Song, X.-D.; Wang, S.; Hao, C.; Qiu, J.-S., Investigation of so2 gas adsorption in metal–organic frameworks by molecular simulation. *Inorg. Chem. Commun.* **2014,** *46*, 277-281.

93. Anderson, T. R.; Hawkins, E.; Jones, P. D., Co2, the greenhouse effect and global warming: From the pioneering work of arrhenius and callendar to today's earth system models. *Endeavour.* **2016,** *40* (3), 178-187.

94. Cassia, R.; Nocioni, M.; Correa-Aragunde, N.; Lamattina, L., Climate change and the impact of greenhouse gasses: Co(2) and no, friends and foes of plant oxidative stress. *Front. Plant Sci.* **2018,** *9*, 273-273.

95. Haustein, K.; Allen, M. R.; Forster, P. M.; Otto, F. E. L.; Mitchell, D. M.; Matthews, H. D.; Frame, D. J., A real-time global warming index. *Sci. Rep.* **2017,** *7* (1), 15417-15417.

96. Henderson-Sellers, A.; Meadows, A. J., The evolution of the surface temperature of mars. *Plantet. Space Sci.* **1976,** *24* (1), 41-44.

97. Yue, X.-L.; Gao, Q.-X., Contributions of natural systems and human activity to greenhouse gas emissions. *Adv. Clim. Change Res.* **2018,** *9* (4), 243-252.

98. Prentice, I.; Farquhar, G.; Fasham, M.; Goulden, M.; Heimann, M.; Jaramillo, V.; Kheshgi, H.; Le Quéré, C.; Scholes, R.; Wallace, D. W. R.; al, e., The carbon cycle and atmospheric carbon dioxide. 2001.

99. Ekwurzel, B.; Boneham, J.; Dalton, M. W.; Heede, R.; Mera, R. J.; Allen, M. R.; Frumhoff, P. C., The rise in global atmospheric co2, surface temperature, and sea level from emissions traced to major carbon producers. *Clim. Change.* **2017,** *144* (4), 579-590.

100. Lelieveld, J.; Klingmüller, K.; Pozzer, A.; Burnett, R. T.; Haines, A.; Ramanathan, V., Effects of fossil fuel and total anthropogenic emission removal on public health and climate. *Proc. Natl. Acad. Sci.* **2019,** *116* (15), 7192.

101. Abdallah, L.; El-Shennawy, T., Reducing carbon dioxide emissions from electricity sector using smart electric grid applications. *J. Eng.* **2013,** *2013*, 845051.

102. Santos, G., Road transport and co2 emissions: What are the challenges? *Transp. Policy.* **2017,** *59*, 71-74.

103. Solomon, S.; Plattner, G.-K.; Knutti, R.; Friedlingstein, P., Irreversible climate change due to carbon dioxide emissions. *Proc. Natl. Acad. Sci.* **2009,** *106* (6), 1704.

104. Jacobson, T. A.; Kler, J. S.; Hernke, M. T.; Braun, R. K.; Meyer, K. C.; Funk, W. E., Direct human health risks of increased atmospheric carbon dioxide. *Nat. Sustain.* **2019,** *2* (8), 691-701.

105. Azuma, K.; Kagi, N.; Yanagi, U.; Osawa, H., Effects of low-level inhalation exposure to carbon dioxide in indoor environments: A short review on human health and psychomotor performance. *Environ. Int.* **2018,** *121*, 51-56.

106. Satish, U.; Mendell, M. J.; Shekhar, K.; Hotchi, T.; Sullivan, D.; Streufert, S.; Fisk, W. J., Is co2 an indoor pollutant? Direct effects of low-to-moderate co2 concentrations on human decision-making performance. *Environ. Health Perspect.* **2012,** *120* (12), 1671-1677.

107. Permentier, K.; Vercammen, S.; Soetaert, S.; Schellemans, C., Carbon dioxide poisoning: A literature review of an often forgotten cause of intoxication in the emergency department. *Int. J. Emerg. Med.* **2017,** *10* (1), 14.

108. Kulp, S. A.; Strauss, B. H., New elevation data triple estimates of global vulnerability to sea-level rise and coastal flooding. *Nat. Commun.* **2019,** *10* (1), 4844.

109. Du, B.; Tandoc, M. C.; Mack, M. L.; Siegel, J. A., Indoor co2 concentrations and cognitive function: A critical review. *Indoor Air.* **2020,** *30* (6), 1067-1082.

110. Karnauskas, K. B.; Miller, S. L.; Schapiro, A. C., Fossil fuel combustion is driving indoor co(2) toward levels harmful to human cognition. *Geohealth.* **2020,** *4* (5).

111. Vehviläinen, T.; Lindholm, H.; Rintamäki, H.; Pääkkönen, R.; Hirvonen, A.; Niemi, O.; Vinha, J., High indoor co2 concentrations in an office environment increases the transcutaneous co2 level and sleepiness during cognitive work. *J. Occup. Environ. Hyg.* **2016,** *13* (1), 19-29.

112. da Silva, E. F.; Booth, A. M., Emissions from postcombustion co2 capture plants. *Environ. Sci. Technol.* **2013,** *47* (2), 659-660.

113. Niedermaier, I.; Bahlmann, M.; Papp, C.; Kolbeck, C.; Wei, W.; Krick Calderón, S.; Grabau, M.; Schulz, P. S.; Wasserscheid, P.; Steinrück, H.-P.; Maier, F., Carbon dioxide capture by an amine functionalized ionic liquid: Fundamental differences of surface and bulk behavior. *J. Am. Chem. Soc.* **2014,** *136* (1), 436-441.

114. Wu, Y.; Xu, J.; Mumford, K.; Stevens, G. W.; Fei, W.; Wang, Y., Recent advances in carbon dioxide capture and utilization with amines and ionic liquids. *Green Chem. Eng.* **2020,** *1* (1), 16-32.

115. Said, R. B.; Kolle, J. M.; Essalah, K.; Tangour, B.; Sayari, A., A unified approach to co2–amine reaction mechanisms. *ACS Omega.* **2020,** *5* (40), 26125-26133.

116. Krótki, A.; Więcław Solny, L.; Stec, M.; Spietz, T.; Wilk, A.; Chwoła, T.; Jastrząb, K., Experimental results of advanced technological modifications for a co2 capture process using amine scrubbing. *Int. J. Greenh. Gas Control.* **2020,** *96*, 103014.

117. Gao, J.; Wang, S.; Sun, C.; Zhao, B.; Chen, C., Corrosion behavior of carbon steel at typical positions of an amine-based co2 capture pilot plant. *Ind. Eng. Chem. Res.* **2012,** *51* (19), 6714-6721.

118. Zhao, B.; Sun, Y.; Yuan, Y.; Gao, J.; Wang, S.; Zhuo, Y.; Chen, C., Study on corrosion in co2 chemical absorption process using amine solution. *Energy Procedia.* **2011,** *4*, 93-100.

119. Singh, G.; Lee, J.; Karakoti, A.; Bahadur, R.; Yi, J.; Zhao, D.; AlBahily, K.; Vinu, A., Emerging trends in porous materials for co2 capture and conversion. *Chem. Soc. Rev.* **2020,** *49* (13), 4360-4404.

120. Bae, Y.-S.; Snurr, R. Q., Development and evaluation of porous materials for carbon dioxide separation and capture. *Angew. Chem. Int. Ed.* **2011,** *50* (49), 11586-11596.

121. Casco, M. E.; Martínez-Escandell, M.; Silvestre-Albero, J.; Rodríguez-Reinoso, F., Effect of the porous structure in carbon materials for co2 capture at atmospheric and high-pressure. *Carbon.* **2014,** *67*, 230-235.

122. Zhang, Z.; Zhao, Y.; Gong, Q.; Li, Z.; Li, J., Mofs for co2 capture and separation from flue gas mixtures: The effect of multifunctional sites on their adsorption capacity and selectivity. *Chem. Commun.* **2013,** *49* (7), 653-661.

123. Ding, M.; Flaig, R. W.; Jiang, H.-L.; Yaghi, O. M., Carbon capture and conversion using metal–organic frameworks and mof-based materials. *Chem. Soc. Rev.* **2019,** *48* (10), 2783-2828.

124. Siegelman, R. L.; McDonald, T. M.; Gonzalez, M. I.; Martell, J. D.; Milner, P. J.; Mason, J. A.; Berger, A. H.; Bhown, A. S.; Long, J. R., Controlling cooperative co2 adsorption in diamine-appended mg2(dobpdc) metal–organic frameworks. *J. Am. Chem. Soc.* **2017,** *139* (30), 10526-10538.

125. Jayanty, R. K. M.; Fuerst, R. G.; Logan, T. J.; Midgett, M. R., A new audit method for epa reference method 6. *J. Air. Pollut. Control Assoc.* **1984,** *34* (3), 242-246.

126. Sulcius, A.; Griskonis, E.; Žmuidzinavičienė, N., Copper dissolution in concentrated sulfuric acid. *World J. Chem. Educ.* **2019**, 196-202.

127. Langmaier, J.; Opekar, F., A simple laboratory generator for low concentrations of sulphur dioxide. *Anal. Chim. Acta.* **1985,** *166*, 305-310.

128. Voegele, A.; Tautermann, C.; Loerting, T.; Hallbrucker, A.; Mayer, E.; Liedl, K., About the stability of sulfurous acid (h2so3) and its dimer. *Chemistry.* **2002,** *8*, 5644-51.

129. MacInnis, J. J.; VandenBoer, T. C.; Young, C. J., Development of a gas phase source for perfluoroalkyl acids to examine atmospheric sampling methods. *Analyst.* **2016,** *141* (12), 3765-3775.

130. Murugappan, K.; Silvester, D., Electrochemical studies of hydrogen chloride gas in several room temperature ionic liquids: Mechanism and sensing. *Phys. Chem. Chem. Phys.* **2015,** *18*.

131. Tumbiolo, S.; Vincent, L.; Gal, J.-F.; Maria, P.-C., Thermogravimetric calibration of permeation tubes used for the preparation of gas standards for air pollution analysis. *Analyst.* **2005,** *130* (10), 1369-1374.

132. Lao, M.; Crilley, L. R.; Salehpoor, L.; Furlani, T. C.; Bourgeois, I.; Neuman, J. A.; Rollins, A. W.; Veres, P. R.; Washenfelder, R. A.; Womack, C. C.; Young, C. J.; VandenBoer, T. C., A portable, robust, stable, and tunable calibration source for gas-phase nitrous acid (hono). *Atmos. Meas. Tech.* **2020,** *13* (11), 5873-5890.

133. Haerri, H. P.; Mace, T.; Walden, J.; Pascale, C.; Niederhauser, B.; Wirtz, K.; Stovcik, V.; Christophe, S.; Couette, J.; Waldén, T., Dilution and permeation standards for the generation of no, no 2 and so 2 calibration gas mixtures. *Meas. Sci. Technol.* **2017,** *28*, 035801.

134. Sun, M.; Yu, H.; Zhang, K.; Zhang, Y.; Yan, Y.; Huang, D.; Wang, S., Determination of gaseous sulfur dioxide and its derivatives via fluorescence enhancement based on cyanine dye functionalized carbon nanodots. *Anal. Chem.* **2014,** *86* (19), 9381-9385.

135. Bryant, A. P., Potassium permanganate for sulfur dioxide determinations. *J. Ind. Eng. Chem.* **1916,** *8* (7), 663-663.

136. Rosenberg, R. M.; Peticolas, W. L., Henry's law: A retrospective. *J. Chem. Educ.* **2004,** *81* (11), 1647.

137. Mitchell, G. D., A review of permeation tubes and permeators. *Sep. Purif. Methods.* **2000,** *29* (1), 119-128.

138. Washenfelder, R. A.; Roehl, C.; McKinney, K.; Julian, R.; Wennberg, P., A compact, lightweight gas standards generator for permeation tubes. *Rev. Sci. Instrum.* **2003,** *74*, 3151-3154.

139. Ec9850 sulfur dioxide analyzer, operation manual, a & b series. . Ecotech Pty Ltd: 2007.

140. Mehio, N.; Dai, S.; Jiang, D.-e., Quantum mechanical basis for kinetic diameters of small gaseous molecules. *J. Phys. Chem. A.* **2014,** *118* (6), 1150-1154.

141. Rouquerol, J.; Rouquerol, F.; Llewellyn, P.; Maurin, G.; Sing, K. S., *Adsorption by powders and porous solids: Principles, methodology and applications*. Academic press: 2013.

142. Lowell, S.; Shields, J. E.; Thomas, M. A.; Thommes, M., *Characterization of porous solids and powders: Surface area, pore size and density*. Springer Science & Business Media: 2012; Vol. 16.

143. kloutse ayevide, F.; Zacharia, R.; Cossement, D.; Chahine, R.; Balderas Xicohténcatl, R.; Oh, H.; Streppel, B.; Schlichtenmayer, M.; Hirscher, M., Isosteric heat of hydrogen adsorption on mofs: Comparison between adsorption calorimetry, sorption isosteric method, and analytical models. *J. Appl. Phys. A.* **2015,** *121*, 1-8.

144. Fakhraei Ghazvini, M.; Vahedi, M.; Najafi Nobar, S.; Sabouri, F., Investigation of the mof adsorbents and the gas adsorptive separation mechanisms. *Journ. Environ. Chem. Eng.* **2021,** *9* (1), 104790.

145. Ding, L.; Yazaydin, A. O., The effect of so2 on co2 capture in zeolitic imidazolate frameworks. *Phys. Chem. Chem. Phys.* **2013,** *15* (28), 11856-11861.

146. McGrath, D. T.; Downing, V. A.; Katz, M. J., Investigating the crystal engineering of the pillared paddlewheel metal–organic framework zn2(nh2bdc)2dabco. *CrystEngComm.* **2018,** *20* (39), 6082-6087.

147. Burrows, A.; Cassar, K.; Friend, R.; Mahon, M.; Rigby, S.; Warren, J., Solvent hydrolysis and templating effects in the synthesis of metal-organic frameworks. *CrystEngComm.* **2005,** *7*, 548-550.

148. Thaore, V. B.; Gaikar, V. G., Kinetic model development for steam pyrolysis of dimethylformamide in a tubular reactor. *Ind. Eng. Chem. Res.* **2013,** *52* (31), 10601-10608.

149. Redlich, C. A.; Beckett, W. S.; Sparer, J.; Barwick, K. W.; Riely, C. A.; Miller, H.; Sigal, S. L.; Shalat, S. L.; Cullen, M. R., Liver disease associated with occupational exposure to the solvent dimethylformamide. *Ann. Int. Med.* **1988,** *108* (5), 680-6.

150. Lee, J.; Hahm, M.; Huh, D.-A.; Byeon, S.-H., Prioritizing type of industry through health risk assessment of occupational exposure to dimethylformamide in the workplace. *Int. J. Environ. Res. Public. Health.* **2018,** *15* (3), 503.

151. Tao, C.-A.; Wang, J.-F., Synthesis of metal organic frameworks by ball-milling. *Crystals.* **2020,** *11*, 15.

152. Hansen, C. M., *Hansen solubility parameters: A user's handbook*. second ed.; CRC Pres: Boca Raton, FL, 2007.

153. Verheijen, M.; Lienhard, M.; Schrooders, Y.; Clayton, O.; Nudischer, R.; Boerno, S.; Timmermann, B.; Selevsek, N.; Schlapbach, R.; Gmuender, H.; Gotta, S.; Geraedts, J.; Herwig, R.; Kleinjans, J.; Caiment, F., Dmso induces drastic changes in human cellular processes and epigenetic landscape in vitro. *Sci. Rep.* **2019,** *9* (1), 4641.

154. Elisia, I.; Nakamura, H.; Lam, V.; Hofs, E.; Cederberg, R.; Cait, J.; Hughes, M. R.; Lee, L.; Jia, W.; Adomat, H. H.; Guns, E. S.; McNagny, K. M.; Samudio, I.; Krystal, G., Dmso represses inflammatory cytokine production from human blood cells and reduces autoimmune arthritis. *PLoS One.* **2016,** *11* (3), 0152538-0152538.

155. Woolven, H.; González-Rodríguez, C.; Marco, I.; Thompson, A. L.; Willis, M. C., Dabco-bis(sulfur dioxide), dabso, as a convenient source of sulfur dioxide for organic synthesis: Utility in sulfonamide and sulfamide preparation. *Org. Lett.* **2011,** *13* (18), 4876-4878.

Appendix A

Table A.1. Summary of Crystallographic Data and Structure Refinement Parameters for $\mathrm{Zn_2M(NH_2BDC)_3DABCO}$ (M = Zn, Cd); $\mathrm{Zn_3}$ = $\mathrm{Zn_3(NH_2BDC)_3DABCO}$ and $\mathrm{Zn_2Cd}$ = $\mathrm{Zn_2Cd(NH_2BDC)_3DABCO}$.

Compound	**$\mathrm{Zn_3}$ (DMSO)**	**$\mathrm{Zn_3}$ (MeOH)**	**$\mathrm{Zn_2Cd}$ (MeOH)**
Formula	$\mathrm{Zn_3C_{30}H_{27}N_5O_{12}\cdot(C_2H_6OS)_6}$	$\mathrm{Zn_3C_{30}H_{27}N_5O_{12}}$	$\mathrm{Zn_2CdC_{30}H_{27}N_5O_{12}}$
Formula weight (g/mol)	1305.45	845.71	892.73
Temperature (K)	293	100	100
Radiation	MoKα	MoKα	MoKα
Crystal system	Trigonal	Trigonal	Trigonal
Space group	R -3	R -3 m	R -3 m
a (Å) = b(Å)	18.3449(3)	18.12696(2)	18.4624(3)
c (Å)	13.8930(3)	13.64843(2)	13.8878(3)
Volume (Å^3)	4049.08(15)	3883.857(8)	4099.58(14)
Z	3	3	3
ρ_{calc} (g/cm^3)	1.606	1.077	1.085
μ (mm^{-1})	1.628	1.423	1.299
GOF on F^2	1.0236	1.0303	0.9873
θ range for data collection (°)	1.947–29.437	2.2471–39.1940	2.2062–41.2574
Index ranges	$-24 \le h \le 24$ $-25 \le k \le 25$ $-18 \le l \le 19$	$-31 \le h \le 31$ $-26 \le k \le 19$ $-23 \le l \le 19$	$-31 \le h \le 34$ $-34 \le k \le 32$ $-24 \le l \le 24$
Reflections collected	21106	12615	15125
Independent reflections	2394 [R_{int} = 0.047]	2623 [R_{int} = 0.027]	3196 [R_{int} = 0.033]
Data/restraints/parameters	2281/48/138	1944/29/79	2578/20/81
Largest diff. peak and hole (e Å^{-3})	2.64, 1.30	2.08, -3.29	0.72, -0.67
Final R indices [I≥2σ(I)]	R_1 = 0.0706 wR_2 = 0.1622	R_1 = 0.0586 wR_2 = 0.1518	R_1 = 0.0252 wR_2 = 0.0663
Final R indices [all data]	R_1 = 0.0706 wR_2 = 0.1622	R_1 = 0.0586 wR_2 = 0.1518	R_1 = 0.0252 wR_2 = 0.0663

Table A.2. Summary of Bond Lengths and Bond Angles for $Zn_2M(NH_2BDC)_3DABCO$ (M = Zn, Cd) using a Molybdenum Radiation Source; Zn_3 = $Zn_3(NH_2BDC)_3DABCO$ (a) and Zn_2Cd = $Zn_2Cd(NH_2BDC)_3DABCO$ (b).

	Bond Length Label	**Bond Length (Å)**
Zn_3 (MeOH)	Zn2 – O1	2.086(2)
	Zn1 – O22	1.914(3)
	Cd1 – O2	2.442(15)
	Zn1 – O1	1.9210(14)
Zn_2Cd (MeOH)	**Bond Angle Label**	**Bond Angle (°)**
	O22– Zn1 – O22	96.22(10)
	O1 – Zn2 – O1	117.11(6)
	O1– Zn1 – O1	101.87(9)
	O2 – Cd1 – O2	117.35(3)